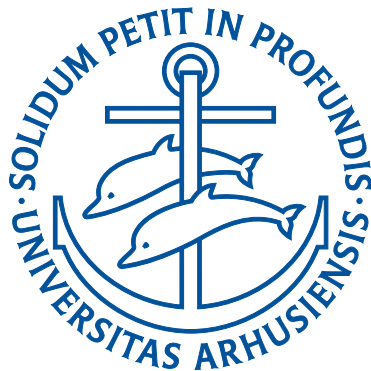

Ultrashort-Pulse Laser Modification of Materials: Understanding and Controlling the Optical Properties



Kristian Juncher Wædegaard

Department of Physics and Astronomy
Aarhus University, Denmark

PhD Thesis
May 2013

This thesis has been submitted to the Graduate School of Science and Technology (GSST) at Aarhus University, in order to fulfill the requirements for obtaining a PhD degree in physics. The work has been carried out under the supervision of associate Professor Peter Balling at the Department of Physics and Astronomy.

1st Edition

—

This document was compiled and typeset in L^AT_EX

May 24, 2013

Contents

Acknowledgements	v
List of publications	vii
Outline	ix
1 Introduction	1
1.1 Gaussian pulses and fluence	2
1.2 Optical properties: Maxwell's equations	3
1.3 Material excitation	6
I Femtosecond-laser excitation of dielectric materials	
2 Modeling of laser excitation of dielectric materials	11
2.1 Introduction	12
2.2 Laser-excitation of dielectric materials	12
2.3 Single-rate-equation models	15
2.4 Multiple-rate-equations model	16
2.5 Excitation mechanisms	21
2.6 Optical properties	26
2.7 Optical field propagation	32
2.8 Material response	35
2.9 Simulation output	36
2.10 Discussion and outlook	42
3 Aarhus experiments: Ablation and self-reflectance	45

3.1	Experimental	46
3.2	Simulations	48
3.3	Results	50
3.4	Discussion and outlook	55
4	CEA experiments:	
	Spectral interferometry, reflectance, and ablation	59
4.1	Introduction	60
4.2	Experimental setup	61
4.3	Simulations	65
4.4	Results	71
4.5	Discussion	79
4.6	Experiments on quartz	82
5	Excitation of water by temporally shaped pulses	87
5.1	introduction	88
5.2	Experiments	88
5.3	Data analysis	93
5.4	Simulations	100
5.5	Discussion and outlook	105
 II Laser-written computer-generated holograms		
6	Laser-written holography	111
6.1	Classical holography	112
6.2	Computer-generated holography	114
6.3	Laser-written CGHs	118
6.4	Optimization of the holographic reconstruction	126
6.5	Discussion	135
7	Summary	139
8	Dansk resumé	141
	Bibliography	145

Acknowledgements

First and foremost, I wish to thank my supervisor Peter Balling for excellent and dedicated supervision. I have enjoyed some very pleasant years in Peter's group: I first joined it when I started my Bachelor's project in December 2006 and I am happy that I also got the opportunity to do a PhD with him. The door to Peter's office has always been open and he has taken the time to discuss my project almost on a daily basis. Peter shows a genuine interest in his students – both personally and professionally, which has given not just a pleasant everyday working atmosphere, but also made our trips to various conferences and international collaborators very enjoyable.

The CATSUP group has been a big part of my PhD and I would like to thank all the people who have been a part of it: Jeppe Byskov, Christian Smith, and Juha-Matti Savolainen for some good conference trips, Bjarke Christensen for valuable insight into the dielectrics model, when I first started working on that, Ditte Sandkamm for a pleasant and productive stay in the Parisian suburbs. Also, thanks to the rest of the group for good times in the lab, group meetings, summer barbecues, christmas dinners, and other social events.

I thank Stéphane Guizard and Alexandros Mouskeftaras for a good collaboration in connection with the experiments at CEA in Saclay, France. I appreciate the invitation from Thomas Baumert for Peter and me to visit his group at the University of Kassel. It was a couple of intense days with very fruitful discussions, and for this I thank Thomas Baumert, Cristian Sarpe, Thomas Winkler, and Matthias Wollenhaupt. I hope that this was just the beginning of a long collaboration between the two groups.

Also, I would like to thank Peter Skyt and Benedikte Klærke for proofreading this thesis.

Thanks to my friends for fun and memorable times during my studies and to my family for their support and interest in my work. Finally, I owe a special thanks to my wonderful girlfriend Benedikte for making every day better.

Kristian Juncher Wædegaard
May 2013

List of publications

- K. J. Wædegaard and P. Balling
High-resolution computer-generated reflection holograms with three-dimensional effects written directly on a silicon surface by a femtosecond laser
Optics Express **19**, 3434 (2011)
- K. Wædegaard, M. Frislev, L. A. Kjær, and P. Balling
Femtosecond laser excitation of dielectric materials: Optical properties and ablation
AIP Conference Proceedings **1464**, 32 (2012)
- K. Wædegaard, M. Frislev, and P. Balling
Femtosecond laser excitation of dielectric materials: experiments and modeling of optical properties and ablation depths
Applied Physics A **110**, 601 (2013)
- K. J. Wædegaard, H. D. Hansen, and P. Balling
Optimizing the efficiency of femtosecond-laser-written holograms
Applied Physics B, online first (DOI: 10.1007/s00340-013-5496-0)
(2013)
- K. J. Wædegaard, D. B. Sandkamm, A. Mouskeftaras, S. Guizard, and P. Balling
Modeling of short-pulse laser excitation of dielectrics
Physical Review Letters, submitted (2013)

- K. J. Wædegaard, C. Sarpe, T. Winkler, J. Köhler, M. Wollenhaupt, T. Baumert, and P. Balling
Excitation of water by temporally shaped femtosecond laser pulses: Measuring and modeling the transient optical properties including propagation
in preparation (2013)

Outline

Chapter 1 gives a general introduction to laser-material interaction. It presents the temporal and spatial Gaussian-pulse profile and introduces the material optical properties, including the complex refractive index. Various degrees of material excitation are described, including laser ablation.

Chapter 2 provides a detailed explanation of the model used to describe the interaction between ultrashort-laser pulses and dielectric materials. The different ingredients of the model (excitation, optical properties, light-field propagation) are discussed, and it is explained how they are incorporated in the numerical simulations. The simulation output is presented in the form of a thorough analysis of the excitation profiles for two different fluences.

Chapter 3 presents results from experiments carried out at Aarhus University, where the self-reflectance and ablation depth is measured on a sapphire sample. The experimental results are compared to numerical simulations.

Chapter 4 describes the experiments performed in collaboration with the group of Professor Stéphane Guizard at the “Centre Energie Atomique” (CEA) in Sacclay, France: Pump-probe experiments that combine spectral interferometry with reflectance and ablation-depth measurements. The combination of the different techniques enables measurements over a large range of fluences and provides further comparison to the numerical simulations.

Chapter 5 presents results from spectral-interferometry experi-

ments on water carried out in the group of Professor Thomas Baumert at the University of Kassel. In an ongoing study, numerical simulations based on the model described in chapter 2 are applied in order to reproduce the experimental results, and preliminary results of this study are presented.

Chapter 6 demonstrates an application of the capabilities of laser-surface modifications: Computer-generated holograms (CGHs) written directly on the surface of reflecting materials. One study investigates CGHs with high resolution and integrated 3-D effects, and another study focusses on optimizing the holograms.

Chapter 7 gives an English summary.

Chapter 8 is a summary in Danish.

Introduction

Today, lasers are used extensively for modification and processing of a wide range of materials [1]. Over the years, ultrashort-pulse lasers such as femtosecond lasers have become a well-known tool for material processing; for reviews on the subject see, e.g., Refs. [1–6]. Many femtosecond lasers used for material processing (including those used in this project) have pulse durations on the order of 100×10^{-15} seconds = 100 femtoseconds (fs). In this very short time, the material motion is practically frozen, which minimizes the heat transfer during processing. Hence, small heat-affected zones can be achieved with femtosecond laser excitation of material surfaces (as well as inside the bulk) [7]. This is in contrast to using continuous wave (cw) or long-pulse duration (e.g. nanosecond) lasers, where heating of the surrounding material (around the laser-interaction region) occurs during the laser excitation. The localized interaction means that ultrashort-pulse lasers can generate very small structures, making it ideal for high-precision micro- and nanostructuring [1].

Femtosecond lasers typically operate in the infrared or visible regimes, which is usually unsuitable for excitation of high band gap materials, such as dielectrics. This is simply because the energy of the photons is less than the material band gap energy, thus not allowing for

linear absorption of the photons. However, the femtosecond lasers can provide very high peak intensities, which enables non-linear excitation processes [8].

In this PhD thesis, results from both a fundamental investigation of the interaction between ultrashort-laser pulses and materials as well as an example of an application are presented. Part I combines numerical modeling with experimental investigations of ultrashort-pulse laser excitation of dielectric materials. In part II, the modification of the optical properties is applied to the production of directly-written computer-generated holograms (CGHs). This illustrates an example of the capabilities of surface modifications by ultrashort-pulse lasers.

1.1 Gaussian pulses and fluence

Throughout this thesis, laser pulses with Gaussian intensity¹ profiles in time and space will be used frequently. For such a pulse, the intensity I as a function of the time t is given by

$$I(t) = I_0 \exp \left[-4 \ln 2 \left(\frac{t - t_0}{\tau} \right)^2 \right], \quad (1.1)$$

where I_0 is the intensity at the temporal center ($t = t_0$) and τ is the full width at half maximum (FWHM) pulse duration. The spatial beam profile at the temporal center is given by

$$I(r) = I_{\text{peak}} \exp \left[-\frac{2r^2}{\omega_0^2} \right], \quad (1.2)$$

where $I_{\text{peak}} = I(r = 0)$ is the intensity at the (spatial) center of the pulse, r is the radial distance from the center, and ω_0 is the spot size of the beam, i.e., the radius where the intensity has dropped to $1/e^2$ relative to the center.

The fluence is defined as the temporally integrated intensity at any point in space

¹The term “intensity” is used for the time averaged power per area of the electromagnetic field, even though the correct term is in fact irradiance.

$$F(r) = \int_{-\infty}^{\infty} I(t) dt. \quad (1.3)$$

For the spatially and temporally Gaussian pulse, the peak intensity, peak fluence F_{peak} , and pulse energy ϵ_{pulse} are related via the pulse duration and spot size by

$$F_{\text{peak}} = I_{\text{peak}} \tau \frac{1}{2} \sqrt{\frac{\pi}{\ln 2}} = \frac{2\epsilon_{\text{pulse}}}{\pi\omega_0^2}. \quad (1.4)$$

The fluence is a measure of the amount of energy per area in the laser pulse, which is often used in connection with femtosecond-laser-material interaction. As mentioned above, the material is essentially frozen during the interaction with the ultrashort-laser pulse. Hence, in many applications, the fluence is a better measure of the pulse strength or ability to cause material excitation – compared to, e.g., the intensity. This is because, the specific pulse duration is not so important as long as it is shorter than the “reaction time” of the material. However, for non-linear processes, such as excitation of dielectric materials, the intensity and pulse duration in fact play crucial roles, as will be discussed in part II of this thesis.

1.2 Optical properties: Maxwell's equations

The propagation of electromagnetic fields inside materials and at interfaces is described by Maxwell's equations including boundary conditions. In differential form, Maxwell's equations are given by [9]

$$\nabla \cdot \mathbf{D} = \rho_f \quad (1.5)$$

$$\nabla \times \mathbf{H} - \frac{\partial \mathbf{D}}{\partial t} = \mathbf{J}_f \quad (1.6)$$

$$\nabla \times \mathbf{E} + \frac{\partial \mathbf{B}}{\partial t} = 0 \quad (1.7)$$

$$\nabla \cdot \mathbf{B} = 0. \quad (1.8)$$

where \mathbf{E} is the electric field, \mathbf{D} the electric displacement field, \mathbf{B} the

magnetic field, \mathbf{H} the magnetizing field, ρ_f the free charge density, and \mathbf{J}_f the free current density. For linear media, $\mathbf{D} = \hat{\varepsilon}\mathbf{E}$ and $\mathbf{B} = \hat{\mu}\mathbf{H}$, where $\hat{\varepsilon}$ is the electric permittivity and $\hat{\mu}$ the magnetic permeability. For most materials, $\hat{\mu}$ can be considered equal to the vacuum permeability ($\hat{\mu} = \mu_0$). Assuming that (i) the free currents can be related to the electric field via Ohm's law $\mathbf{J}_f = \sigma\mathbf{E}$ [9], where σ is the material conductivity, and that there are no free charges, (ii) normal incidence, and (iii) slowly varying $\hat{\varepsilon}$ and σ compared to the optical frequency, plane wave solutions for the electric and magnetic fields to Maxwell's equations can be found. For a dispersive medium ($\sigma \neq 0$), the electric field for a plane monochromatic wave of frequency ω propagating in the z -direction can be expressed as

$$\mathbf{E}(z, t) = E_0 \exp \left[i \left(\tilde{k} \frac{\omega}{c} z - \omega t \right) \right] \hat{\mathbf{e}}_y, \quad (1.9)$$

where E_0 is the electric-field amplitude at $z = 0$, c the speed of light in vacuum, $i = \sqrt{-1}$ the imaginary unit, and $\hat{\mathbf{e}}_y$ the polarization direction of the electric field. \tilde{k} is the complex refractive index, which is related to the $\hat{\varepsilon}$ and σ by

$$\tilde{k}^2 = \varepsilon = \hat{\varepsilon}_r + i \frac{\sigma}{\omega \varepsilon_0}, \quad (1.10)$$

where ε_0 is the vacuum permittivity and $\hat{\varepsilon}_r = \hat{\varepsilon}/\varepsilon_0$ is the relative permittivity. ε is the so-called dielectric function, which for perfect insulators ($\sigma = 0$) is equal to the relative permittivity. Since \tilde{k} is complex, it can be split into its real and imaginary parts

$$\tilde{k} = k + i\kappa. \quad (1.11)$$

Inserting this in Eq. (1.9) gives

$$\mathbf{E}(z, t) = E_0 \exp \left(-\frac{\kappa\omega}{c} z \right) \times \exp \left[i \left(\frac{k\omega}{c} z - \omega t \right) \right] \hat{\mathbf{e}}_y. \quad (1.12)$$

This is a plane wave propagating at a speed of c/k with an exponential attenuation of the amplitude characterized by $\kappa\omega/c$. The wavelength of the field is $\lambda' = \lambda/k = 2\pi c/(k\omega)$, where λ is the vacuum wavelength.

The optical period is $2\pi/\omega$, which is about 3 fs for a wavelength of 800 nanometers (nm). Hence, the temporal changes in $\hat{\epsilon}$ and σ have to be slower than this for the above equations to be valid.

The intensity of the electromagnetic wave is related to the electric field by

$$I(z) = \frac{1}{2}\varepsilon_0ck|\mathbf{E}|^2 = I_0 \exp\left(-\frac{2\kappa\omega}{c}z\right), \quad (1.13)$$

where I_0 is the intensity at $z = 0$, which is related to the electric field by [10]

$$I_0 = \frac{1}{2}\varepsilon_0ckE_0^2. \quad (1.14)$$

The absorption coefficient $\alpha_{\text{abs}} = 2\kappa\omega/c$ is an inverse absorption length, which determines how quickly the light field is absorbed as it propagates through the medium. For good conductors, e.g., metals, α_{abs} is large, and the light field is absorbed over a short distance – usually on the order of tens of nanometers. In dielectric materials (insulators), on the other hand, $\kappa \simeq 0$ and the light field propagates (almost) unperturbed through the material – e.g. as sunlight through a window.

1.2.1 Interfaces: Reflectance and transmittance

When a propagating electromagnetic field encounters an interface with an abrupt change in the refractive index, part of the light is reflected and the rest is transmitted (and refracted) in the “new” medium. How much is reflected and transmitted is determined by the boundary conditions applied to the solutions of Maxwell's equations. The ratios depend on the refractive index of the two media, the angle of incidence and the polarization of the light. For an interface between vacuum and a material with complex refractive index \tilde{k} , the reflectance R and transmittance T at normal incidence are given by the Fresnel equations [9]

$$R = \left| \frac{1 - \tilde{k}}{1 + \tilde{k}} \right|^2 \quad \text{and} \quad T = k \left| \frac{2}{1 + \tilde{k}} \right|^2. \quad (1.15)$$

Here, R and T are defined as the ratios of the reflected and transmitted *intensities* relative to the incoming intensity, which means $R + T = 1$. The magnetic permeability is assumed equal to the vacuum permeability. It should be emphasized that these equations only apply when there is an immediate change in the refractive index. Continuous changes in the refractive index do *not* cause any reflections.

1.3 Material excitation

When a material is excited by a (femtosecond) laser pulse, the optical properties change due to changes in the dielectric function. A model describing how the optical properties of a dielectric material change with excitation is presented in chapter 2. Depending on the degree of excitation, the changes may be temporary or permanent. At low excitation, typically, the change in the optical properties will disappear due to, e.g., electron-hole recombination and/or heat diffusion to the surrounding material. This usually occurs on a time scale longer than the pulse duration (> 1 picosecond (ps)). At moderate excitation, permanent modifications may be induced, e.g., local changes in the material density of a dielectric, which causes changes in the refractive index. At even higher excitation, the material may locally become unstable due to the electronic excitation or the temperature may simply become so high that the material evaporates. The result is removal of material due to laser excitation – a phenomenon known as laser ablation.

1.3.1 Laser ablation

In laser ablation, the size of the ablated region depends on material parameters as well as the spot size of the laser beam at the surface and the fluence of the laser pulse. For linearly absorbing materials, such as metals and low-band-gap semiconductors, the onset of ablation will often be related to a material-specific threshold fluence F_{th} . If a Gaussian beam profile is assumed, the diameter d of an ablated hole is given by

$$d^2 = 2\omega_0^2 \ln \left(\frac{F_{\text{peak}}}{F_{\text{th}}} \right). \quad (1.16)$$

This expression assumes that heat diffusion is negligible, making it valid only at moderate fluences (up to a few times the threshold fluence). Liu [11] shows that by measuring the diameter of holes made at different pulse energies, this equation (with the pulse energy substituted for the fluence) gives an easy way to determine the beam spot size. The spot size is controlled by the focussing optics, but the lowest achievable spot size is determined by the diffraction limit – it can be down to the order of the wavelength. Hence, ablation structures with sizes down to the wavelength can readily be produced. Strictly speaking, Eq. (1.16) puts no lower bounds on the structure size. In fact, structures well below the spot size has been produced, e.g., by Pronko *et al.* [12], who demonstrate 300 nm wide holes in a metal film generated by an 800-nm laser focused to a spot size of 3 μm . Vestentoft *et al.* [13] use micro-spheres as a lens array to produce 500-nm size holes with an 800-nm laser in solid copper samples. A recent study by Englert *et al.* [14] demonstrates how temporally tailored femtosecond pulses can be used to generate ablation structures in fused silica with a size an order of magnitude below the diffraction limit.

Besides removing material, laser ablation also changes the morphology and, thus, the optical response of the surface left behind. The ablated surface region is usually quite uneven and rough compared to, e.g., an initially flat polished surface. The rough surface will scatter and absorb light more easily, while specular reflection will be reduced. This is exploited in Part II of this thesis, where the reduced reflectance is utilized to produce CGHs on otherwise reflecting surfaces. Here, the ability to create small structures with short pulse durations facilitates a high resolution of the CGHs, which enhances their quality.

Part I

Femtosecond-laser excitation of dielectric materials

Modeling of laser excitation of dielectric materials

This first part of the thesis focusses on the interaction between ultrashort-laser pulses and dielectric materials, and the resulting electronic excitation of the dielectric. This chapter explains the various details of a model used for numerical simulations of the laser-material interaction. The model is based on the so-called multiple-rate equations model developed by Rethfeld [15], which is introduced. The transient optical properties are described, including modeling of the electron-scattering rate, which has proven to be an important parameter. The different outputs extracted from the simulations and how they depend on the laser fluence is presented. Finally, the model – including limitations and future aspects – is discussed. Chapters 3, 4, and 5 compare the model to experiments.

The model is applied in the 4 articles about laser excitation of dielectrics that I have contributed to [16–19]. The individual articles will be presented in the introduction to the respective experimental chapters.

2.1 Introduction

Many different approaches have been suggested for modeling the excitation of dielectric materials by lasers [15,20–42]. As described in chapter 1, it is a good approximation to assume that only the electrons interact with the light field. Therefore, most models are initiated by an electronic excitation in response to the optical field. Material excitation by energy transfer from the electrons to the lattice may be included to determine the material response. For ultrashort laser-pulse durations, the lattice can be assumed to be frozen during the pulse duration. Hence, the electron-lattice energy transfer is often treated subsequently and independently of the electronic excitation.

The different models apply different schemes for the electronic excitation – often based on rate equations that include different electronic excitation channels. Also, different approaches are used to describe the optical properties of the excited material, the propagation and absorption of the optical field, and the subsequent material response, e.g., ablation. I will not describe the details, advantages, and drawbacks of the different models here. Specific examples of applied models will be given throughout the chapter when describing the individual components of “our” model. For the interested reader, I will refer to the recent review by Balling and Schou [2] and one by Mézel *et al.* [43].

The various models are intended for different applications, and their applicability is often restricted to limited intensity and excitation regimes. However, in this project, the aim is to develop a model that is applicable over a wide range of intensities, while maintaining a simplicity that prevents it from being impractically time-consuming.

2.2 Laser-excitation of dielectric materials

Over the years, a good qualitative picture of short-pulse excitation of dielectric materials has been developed [1,2]. Figure 2.1 illustrates the various mechanisms involved in the excitation and how this affects the propagating light field and the material response. An intense laser pulse interacts with an initially transparent dielectric, and the front part of the pulse is mainly transmitted (top of box (i) in the figure). The large band gap of the material means that the electronic excitation (by visi-

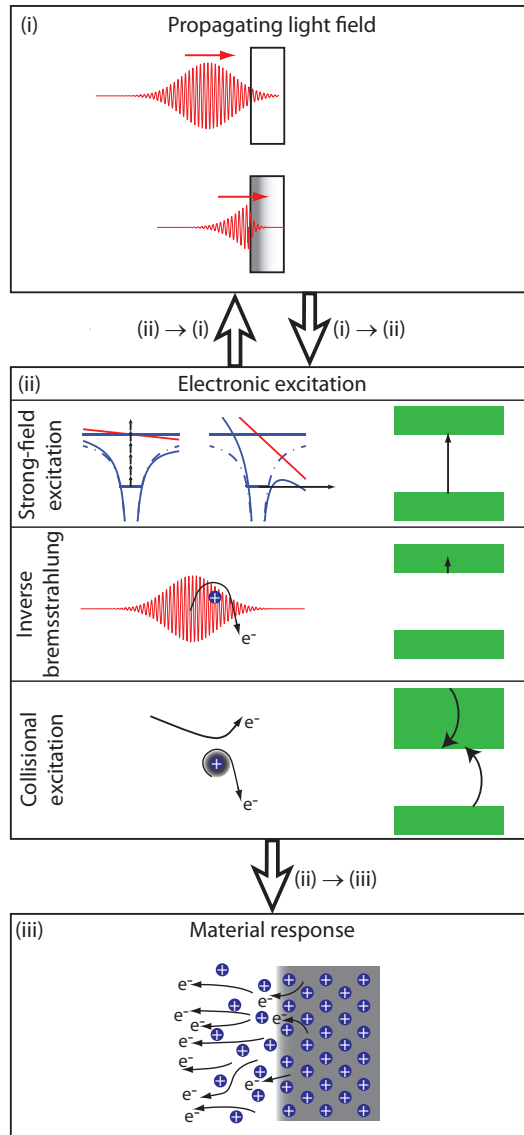


Figure 2.1: Schematic cartoon illustrating the interaction between a dielectric material and an ultra-short laser pulse. In box (ii), the green drawings on the right illustrate how the different excitation mechanisms affect the electrons in the valence band (bottom) and conduction band (top). The figure is taken from Ref. [2]. © IOP Publishing. Reproduced by permission of IOP Publishing. All rights reserved.

ble and near-infrared light) must be initiated by strong-field excitation mechanisms (top of box (ii)). This includes multi-photon excitation (illustrated by the left drawing) or, at even higher intensities, tunnel ionization (right drawing) [8]. At this point, the light field is only attenuated by the corresponding strong-field (non-linear) absorption mechanisms. In the literature, the term strong-field ionization (SFI) is often used for this process, even though strictly speaking, the electrons are only excited to the conduction band and not actually “free”. Nevertheless, the abbreviation, SFI, will be used throughout this thesis.

Once excited, the electrons in the conduction band can be “heated” by the laser field through inverse bremsstrahlung [15,24,32,44,45] (center of box (ii)). If and when the electrons acquire sufficient energy, they may collisionally excite other electrons from the valence to the conduction band (also known as impact ionization). In this process, the highly excited electrons lose kinetic energy corresponding to the energy gain achieved by the newly excited electrons (bottom of box (ii)). Both the previously and newly excited electrons can subsequently be heated and lead to further collisional excitation. The multiplicative nature of this process has led to the term avalanche ionization.

The energy for heating the electrons is naturally absorbed from the light field. Hence, the “free” (conduction band) electrons create a new (linear) absorption channel (represented by the arrow (ii)→(i) in figure 2.1). If the material gets highly excited, the remaining part of the light field will be strongly absorbed. In this case, the absorption properties of the dielectric becomes metal-like, and the light field is absorbed over a thin ‘skin depth’ [21] (bottom of box (i)).

In the end, the overall resulting excitation profile produces a material response (box (iii)). The response can, e.g., be material removal (ablation) or a change in the optical properties. When modeling the excitation of dielectrics, these responses can be compared to experimental measurements. Therefore, models are needed that convert the electronic excitation into a material response. These models may already be part of the excitation model (e.g. for the optical properties), or independent models may be needed (e.g. for ablation).

The understanding of the light-matter interaction described above is the basis of the model that has been developed during this project. A more detailed description of the different mechanisms and the governing equations is given in the following sections.

2.3 Single-rate-equation models

A simple approach to modeling the electronic excitation of dielectric materials is with a single-rate-equation model. The most basic version only includes SFI, however, this is only appropriate at very low light intensities or for extremely short pulses, where the plasma heating can be neglected. Stuart *et al.* [44] propose a straightforward model that also includes collisional (avalanche) excitation. Here, the rate equation that determines the density of excited electrons n as a function of time is given by [44]

$$\frac{\partial n(t)}{\partial t} = \dot{n}_{\text{SFI}}(t) + \beta[I(t)]n(t), \quad (2.1)$$

where \dot{n}_{SFI} is the rate of strong-field excitation, for which Stuart *et al.* [44] use a pure multi-photon rate: $\dot{n}_{\text{SFI}}(t) = \sigma_{\mathcal{N}}I(t)^{\mathcal{N}}$, where \mathcal{N} is the order of the multi-photon process and $\sigma_{\mathcal{N}}$ the \mathcal{N}^{th} -order absorption cross-section. $\beta(I)n$ is the rate of collisional excitation, and $\beta(I)$ can be interpreted as a collisional excitation probability. This probability is dependent on the light-field intensity and vanishes when the pulse is over. The collisional excitation rate can be estimated in different ways. Stuart *et al.* [44] assume a linear dependence on the intensity $\beta(I) = \alpha_{\text{coll}}I$, where α_{coll} is a constant. A more detailed estimate is made by Kennedy [46], who assumes that once an electron reaches the critical level (i.e. the energy level for collisional excitation), it will instantly produce a new conduction-band electron. The rate is then determined by the average time it takes an electron to reach this energy level, which is calculated from a classical absorption rate.

However, these simple descriptions do not adequately implement the “heating time”, i.e., the time it takes the conduction-band electrons to reach the collisional excitation level. For example, Kennedy [46] only uses this heating time to determine the collisional excitation probability. Excitation probabilities and electron densities at concurrent times are used in the rate equation (e.g. Eq. (2.1)). However, in reality, due to the delay between when the electrons are excited and when they can contribute to the collisional excitation, an electron density at an earlier time would be more suitable.

One way of taking this delay into account is to introduce a retarded

time $t_{\text{ret}} = t - t_{\text{heat}}$, where t_{heat} is the heating or retardation time [47,48]. Sarpe *et al.* [48] use the electron density at this retarded time for the collisional-excitation term in Eq. (2.1). Vogel *et al.* [47] and Sarpe *et al.* [48] calculate this heating time as

$$t_{\text{heat}} = \tau_{\text{coll}} \cdot \mathcal{N}', \quad (2.2)$$

where \mathcal{N}' is the number of photons needed to reach the critical level and τ_{coll} a constant electron-scattering time. Hence, the heating time is determined only by the electron-scattering rate. This is based on the fact that the electron heating is caused by inverse Bremsstrahlung, which requires the electron to scatter off, i.e., a phonon or another electron. However, the absorption of photons, naturally, also requires the presence of photons. It seems that a very high density of photons is assumed, so that the time is only limited by the electron-scattering events. A more appropriate measure would be based on the light-field absorption rate (see section 1.2), e.g., the time used by Kennedy *et al.* [46] to determine the collisional excitation rate (as described above). However, as this would not lead to a fixed retarded time, it would greatly reduce the simplicity of the model used, e.g., by Sarpe *et al.* [48].

The introduction of the retarded time still has drawbacks. The light-field intensity at any time is simply paired with the electron density at an earlier time. This does not describe how the electron density, absorption rate, and degree of excitation gradually evolve – also during the heating process. In addition, high light-field intensities complicates matters further as the material band gap can no longer be considered a fixed quantity. These issues are addressed with the introduction of the more elaborate multiple-rate-equations model.

2.4 Multiple-rate-equations model

Based on the description in section 2.2 of the interaction between dielectrics and intense light pulses, Rethfeld [15] suggest the so-called multiple-rate-equations (MRE) model to describe the density of electrons in the conduction band. The conduction-band electrons have of course a continuous energy distribution, but in the model, the conduction band is divided into a set of discrete energy states with electron densities

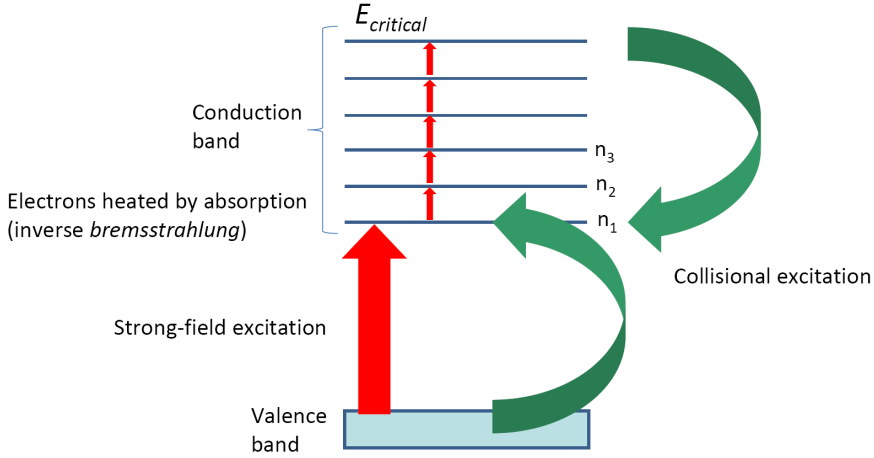


Figure 2.2: A schematic energy diagram of the excitation mechanisms included in the multiple-rate-equations model, as described in detail in the text. The different mechanisms are illustrated in box (ii) in figure 2.1.

given by n_j and corresponding kinetic energies of

$$\epsilon_{\text{kin}}(j) = (j - 1)\hbar\omega_l, \quad (2.3)$$

where ω_l is the laser frequency and \hbar the reduced Planck constant. (Note that ϵ is used for energies and should not be confused with the dielectric function ϵ .) The factor $j - 1$ reflects that the numbering of the states starts at 1, but the kinetic energy of the lowest excited state is 0 eV. The mechanisms included in the model are illustrated in box (ii) in figure 2.1, and a schematic energy diagram of the processes is shown in figure 2.2. Strong-field excitation (big red arrow in figure 2.2) creates the electrons with low energy. These electrons are subsequently excited by the light field (smaller red arrows in figure 2.2) until a critical energy for collisional excitation is reached. By collisional excitation, one electron from the highest conduction-band state collides with an electron from the valence band and produces two electrons in the lowest-lying conduction-band state (green arrows in figure 2.2).

The dynamics of these processes are described by a system of coupled differential equations given by [15]

$$\begin{aligned}
\frac{\partial n_1}{\partial t} &= \dot{n}_{\text{SFI}} - W_{1pt}n_1 + 2\alpha n_N \\
\frac{\partial n_2}{\partial t} &= W_{1pt}n_1 - W_{1pt}n_2 \\
&\vdots \\
\frac{\partial n_{N-1}}{\partial t} &= W_{1pt}n_{N-2} - W_{1pt}n_{N-1} \\
\frac{\partial n_N}{\partial t} &= W_{1pt}n_{N-1} - \alpha n_N.
\end{aligned} \tag{2.4}$$

The photo-excited electrons appear in the lowest conduction band state ($j = 1$), since the SFI rate decreases rapidly with increasing energy barrier. The last term in the first and last equations are due to collisional excitation with α being the collisional-excitation probability. As can be seen, two electrons appear in the first state with each collisional-excitation event; one from the N^{th} conduction band state and one from the valence band. The remaining terms describe the intra-band single-photon absorption, which occurs with a probability given by W_{1pt} . Adding the equations above gives a rate equation for the total density of electrons in the conduction band

$$\frac{\partial n_{\text{con}}}{\partial t} = \dot{n}_{\text{SFI}} + \alpha n_N, \tag{2.5}$$

where $n_{\text{con}} = \sum_{j=1}^N n_j$. As can be seen, this resembles Eq. (2.1), except the collisional excitation term does not depend on the total conduction-band density, but only on the density of electrons that can actually contribute with collisional excitation. Also, as opposed to in Eq. (2.1), α is independent of the intensity. Hence, it is the electron density and not the collisional excitation probability that depends on the intensity, which is a more accurate description of the underlying physical mechanisms. The time delay between SFI and collisional excitation (described in section 2.3) is not an issue as it is automatically incorporated in the MRE model.

2.4.1 Extended MRE

Christensen and Balling [36] extend the MRE model to include propagation of the optical field into the dielectric material. The model takes into account the decreasing intensity of the optical field with increasing distance from the surface, and thus gives a description of the conduction-band electron densities and light-field intensity (or photon density u) throughout the dielectric material. In this model, the conduction-band electrons are assumed to behave as a free-electron gas described by the Drude model [9, 49]. For simplicity, the model is restricted to one-dimensional (1-D) propagation of the optical field. A set of equations similar to the MRE, but with electron densities as functions of both time and depth, is given in Ref. [36].

The equations describing the optical field are given in section 2.7. Several changes to the rate equations have been made compared to the MRE model. To ensure conservation of energy during collisional excitation, the function Υ is introduced, which is given by

$$\Upsilon(x) = \begin{cases} 2 & \text{for } 0 < |x| < 0.25 \\ 1 & \text{for } 0.25 < |x| < 0.75 \\ 0 & \text{else.} \end{cases} \quad (2.6)$$

The argument of Υ includes a (unit-less) function defined as

$$\Delta\hat{\epsilon}(j) = \frac{1}{3}(j - 1 + \epsilon_{\text{corr}}(E_l)/\hbar\omega_l), \quad (2.7)$$

where $\epsilon_{\text{corr}}(E_l)$ is the corrected band gap energy described in section 2.4.2. Furthermore, the single-photon absorption probability in the MRE has been replaced by the Drude plasma absorption W_{pl} to describe the plasma heating due to inverse bremsstrahlung; see section 2.5.2. Lastly, a saturation term ($n_{\text{val}}/n_{\text{tot}}$) has been added to the SFI and collisional excitation terms, where n_{val} and n_{tot} are the valence band and total (valence + conduction band) electron densities, respectively. The saturation term accounts for the fact that there is a finite density of electrons in the valence band, which of course decreases with increasing density in the conduction band.

In the equations, the number of states is chosen to include, as a minimum, the lowest lying state with sufficient energy for collisional ex-

citation to occur. For $\alpha \gg W_{pl}$, which is generally the case, higher-lying states will practically be empty, which is why they are not included. The necessary number of states is strongly dependent on the electric-field amplitude for reasons described in section 2.5.3. Naturally, collisional excitation will only occur as long as there are electrons left in the valence band to excite. At very high laser intensities, the valence band may be depleted, while the heating of the conduction-band electrons continues. In such cases, it is necessary to include more states than the above-mentioned minimum requirement. In practice, the simulations uses a constant number of states N . This implies that collisional excitation may be possible from several of the upper states depending on the light-field intensity. The equations used in the simulations is therefore given by [16]

$$\begin{aligned} \frac{\partial n_1}{\partial t} &= \dot{n}_{SFI}(E_l) \frac{n_{\text{val}}}{n_{\text{tot}}} - W_{pl} n_1 \\ &\quad + \alpha \frac{n_{\text{val}}}{n_{\text{tot}}} \sum_{j'=2}^N n_{j'} \Theta[\epsilon_{\text{kin}}(j') - \epsilon_{\text{coll}}(E_l)] \Upsilon [\Delta \hat{\epsilon}(j')] \end{aligned} \quad (2.8)$$

⋮

$$\begin{aligned} \frac{\partial n_j}{\partial t} &= W_{pl}(n_{j-1} - n_j) - \alpha \frac{n_{\text{val}}}{n_{\text{tot}}} n_j \Theta[\epsilon_{\text{kin}}(j) - \epsilon_{\text{coll}}(E_l)] \\ &\quad + \alpha \frac{n_{\text{val}}}{n_{\text{tot}}} \sum_{j'=j+1}^N n_{j'} \Theta[\epsilon_{\text{kin}}(j') - \epsilon_{\text{coll}}(E_l)] \Upsilon [\Delta \hat{\epsilon}(j') - (j - 1)] \end{aligned} \quad (2.9)$$

⋮

$$\frac{\partial n_N}{\partial t} = W_{pl} n_{N-1} - \alpha \frac{n_{\text{val}}}{n_{\text{tot}}} n_N \Theta[\epsilon_{\text{kin}}(N) - \epsilon_{\text{coll}}(E_l)], \quad (2.10)$$

where all states except 1 and N are given by equation (2.9). Here, Θ is a Heaviside step function assuring that the collisional-excitation term is added and subtracted in the correct states, and $\epsilon_{\text{coll}}(E_l)$ is the kinetic energy needed to achieve collisional excitation, which is described in section 2.5.3.

2.4.2 Corrected band gap

Due to the strong electromagnetic field present in the dielectric material, the free conduction-band electrons oscillate with the electric-field oscillations. This leads to an AC stark shift of the conduction-band states. In the present model, this shift is calculated simply as the mean energy associated with the oscillations of the electrons, which is also known as the ponderomotive energy and is given by [8].

$$U_p = \frac{e^2 E_l^2}{4m^* \omega_l^2}, \quad (2.11)$$

where E_l is the electric-field amplitude of the laser, e the elementary charge, and $m^* = (1/m_{\text{con}} + 1/m_{\text{val}})^{-1}$ is the reduced effective mass calculated from the effective electron mass in the conduction band m_{con} and hole mass in the valence band m_{val} . For valence-band electrons to be excited to the conduction band, they need to absorb enough photons to both overcome the band gap as well as gain the required ponderomotive energy. The corrected band gap is therefore introduced, which is given by

$$\epsilon_{\text{corr}}(E_l) = \epsilon_g + U_p. \quad (2.12)$$

where ϵ_g is the band gap of the unperturbed material.

2.5 Excitation mechanisms

2.5.1 Strong-field excitation

All the processes described in the equations above are initiated by strong-field excitation (SFI). Hence, a good description of the SFI rate is needed. The dominating mechanism responsible for SFI depends on the intensity of the electric field. For relatively weak electric fields, multi-photon absorption is dominating, and a rate that depends on the order of the multi-photon process is widely used: $\dot{n}_{SFI} \propto I^N$ [1]. As the field strength increases, tunnel ionization becomes dominant, and for very strong fields, the Coulomb barrier can be suppressed enough for over-the-barrier ionization to occur.

A quantitative model describing strong-field excitation was proposed by Keldysh [8]. An important parameter in this connection is the so-called Keldysh parameter, given by $\gamma = \omega_l \sqrt{m^* \epsilon_g} / (eE_l)$. The SFI rate is given by [2, 8, 50]

$$\begin{aligned} \dot{n}_{SFI} = & 2 \frac{2\omega_l}{9\pi} \left(\frac{m^* \omega_l}{\hbar \sqrt{\gamma_1}} \right)^{3/2} Q(\gamma, x) \\ & \times \exp \left(-\pi \lfloor x + 1 \rfloor \frac{\mathcal{K}(\gamma_1) - \mathcal{E}(\gamma_1)}{\mathcal{E}(\gamma_2)} \right). \end{aligned} \quad (2.13)$$

Here, I have used the notation of Balling and Schou [2]. However, the expression is identical to the original one by Keldysh [8] except for the correction of small misprints and the inclusion of an extra factor of 2 due to electron spin degeneracy; as according to Gruzdev [50]. Two auxiliary gammas have been introduced [51]: $\gamma_1 = \gamma^2 / (1 + \gamma^2)$ and $\gamma_2 = 1 / (1 + \gamma^2)$. Q is a function given by [2, 8, 50]

$$\begin{aligned} Q(\gamma, x) = & \sqrt{\frac{\pi}{2\mathcal{K}(\gamma_2)}} \times \sum_{n=0}^{\infty} \exp \left(-n\pi \frac{\mathcal{K}(\gamma_1) - \mathcal{E}(\gamma_1)}{\mathcal{E}(\gamma_2)} \right) \\ & \times \Phi \left(\sqrt{\frac{\pi^2 (\lfloor x + 1 \rfloor - x + n)}{2\mathcal{K}(\gamma_2)\mathcal{E}(\gamma_2)}} \right). \end{aligned} \quad (2.14)$$

x is the effective ionization potential in units of photon energy, which is given by [8]

$$x = \frac{2}{\pi} \frac{\epsilon_g}{\hbar \omega_l} \frac{\mathcal{E}(\gamma_2)}{\sqrt{\gamma_1}}, \quad (2.15)$$

and $\lfloor x \rfloor$ denotes the integer below x . \mathcal{K} and \mathcal{E} are the complete elliptic integrals of the first and second kind, and Φ is the Dawson integral.

In the low intensity limit ($\gamma \gg 1$), multi-photon absorption is dominating, and Eq. (2.13) can be estimated by the multi-photon ionization (MPI) rate [2, 8, 50]

$$\begin{aligned} \dot{n}_{MPI} = & 2 \frac{2\omega_l}{9\pi} \left(\frac{m^* \omega_l}{\hbar \sqrt{\gamma_1}} \right)^{3/2} \Phi \left(\sqrt{2\mathcal{N} - 2x} \right) \\ & \times \exp \left(2\mathcal{N} \left(1 - \frac{1}{4\gamma^2} \right) \right) \left(\frac{1}{16\gamma^2} \right)^{\mathcal{N}}, \end{aligned} \quad (2.16)$$

where $\mathcal{N} = \lfloor x + 1 \rfloor$ is the order the multi-photon process (as above). In this high- γ limit, the effective ionization potential can be estimated from the corrected band gap in Eq. (2.12) by

$$x \simeq \epsilon_{\text{corr}} / \hbar \omega_l. \quad (2.17)$$

At the lowest intensities, the MPI rate is proportional to $I^{\mathcal{N}}$, since $\gamma^{-2} \propto E_l^2 \propto I$. This is consistent with that used, e.g., by Stuart *et al.* [44] and Sarpe *et al.* [48], as described in section 2.3. For high intensities ($\gamma \ll 1$), the field is strong enough for tunnel ionization (TI) to dominate. In this regime, the SFI rate can be estimated by [2, 8, 50]

$$\begin{aligned} \dot{n}_{TI} = & 2 \frac{2}{9\pi^2} \frac{\epsilon_g}{\hbar} \left(\frac{m^* \epsilon_g}{\hbar^2} \right)^{3/2} \left(\frac{\hbar \omega_l}{\epsilon_g \gamma} \right)^{5/2} \\ & \times \exp \left(-\frac{\pi}{2} \frac{\epsilon_g \gamma}{\hbar \omega_l} \left(1 - \frac{\gamma^2}{8} \right) \right). \end{aligned} \quad (2.18)$$

The SFI rate for a specific band gap and laser wavelength calculated with the full Keldysh expression (Eq. (2.13)) is shown in figure 2.3. The approximate expressions for the limiting cases (Eqs. (2.16) and (2.18)) are also shown. As can be seen, they estimate the full expression well, in their respective limits.

Calculating absolute values with the full Keldysh expression (Eq. (2.13)) is quite extensive; especially due to the electric-field-dependent elliptic integrals (\mathcal{K} and \mathcal{E}). Historically, the approximate expressions (Eqs. (2.16) and (2.18)) that are much simpler to calculate have, thus, been used more extensively. However, based on the two approximate expressions, there has still been a demand for an SFI rate at all electric-field strengths. Therefore, an interpolation procedure

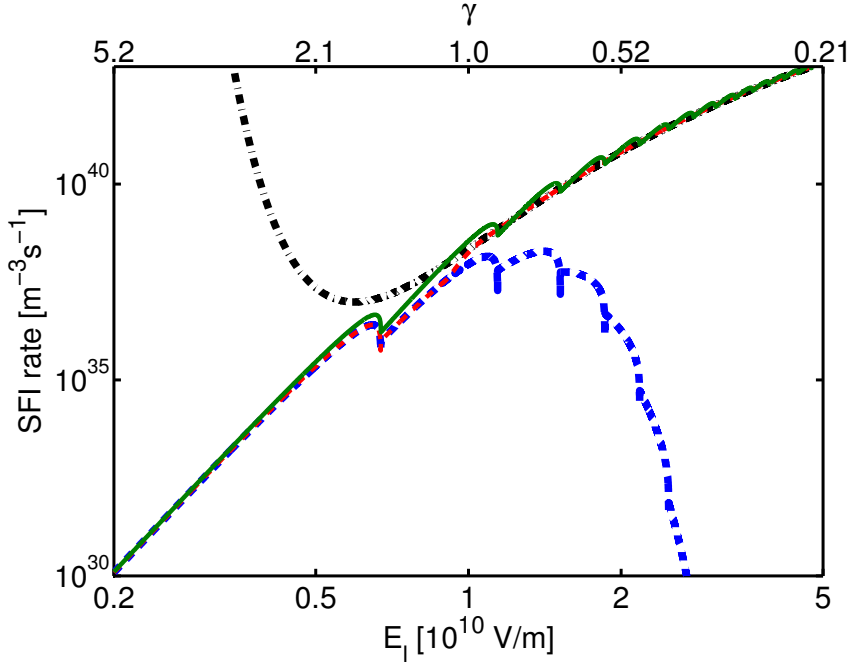


Figure 2.3: The SFI rate as a function of the electric-field strength. The corresponding Keldysh parameters γ are shown on the top x -axis. The thin green solid line is for the full Keldysh expression (Eq. (2.13)). The blue dashed line is the multi-photon ionization rate (Eq. (2.16)) dominating at low intensities (high γ). The black dash-dotted line is the tunnel ionization rate (Eq. (2.18)) dominating at high intensities (low γ). The thin red dashed line is an example of an interpolated curve used to merge the two regimes, as proposed by Kaiser *et al.* [24].

that gives a smooth transition between the MPI and the TI regimes is proposed by Kaiser *et al.* [24], where the approximate expression for the effective ionization potential (Eq. (2.17)) is used. An example of such an interpolation is also shown in figure 2.3. Originally, this interpolation procedure was adapted by our group and is used for the simulations presented in chapter 3 (as well as in Refs. [16, 17, 36, 52]). However, with the computer power available today, the full SFI rate (Eq. (2.13)) can be calculated quite quickly (i.e. minutes) for a large

span of electric-field strengths as needed in this project. Naturally, as this came to our attention, the full expression has been used from then on – i.e. in chapter 4 and Ref. [18].

2.5.2 Electron heating

As mentioned in section 2.2, the “free” electrons in the conduction band are heated by inverse Bremsstrahlung. In the MRE model, this is incorporated as the electrons being promoted up one level. The rate of this is determined by the plasma absorption rate W_{pl} . In the current model, this is given by

$$W_{pl} = \frac{I}{\hbar\omega_l} \frac{2\kappa\omega_l}{c} \frac{1}{n_{con}}, \quad (2.19)$$

where (as above), n_{con} is the total conduction-band density. This rate is calculated from the light-field intensity I since this is used to describe the propagating light field. Previously (chapter 3 and Refs. [16, 17, 36, 52]), the photon density u was used instead of the light-field intensity (more on this in section 2.7). In this case, the plasma absorption rate is given by

$$W_{pl,u} = \frac{2\kappa\omega_l}{n} \frac{u}{n_{con}}. \quad (2.20)$$

As can be seen, the rate is directly proportional to the imaginary part of the refractive index, κ . Section 2.6 describes how the optical properties, including κ , are modeled.

2.5.3 Collisional excitation

As described in section 2.4.2, when electrons are excited to the conduction band they need to bridge the band gap as well as gain the required ponderomotive energy. Therefore, the corrected band gap was introduced (Eq. (2.12)). However, in collisional excitation, momentum conservation must also be considered. To fulfill both energy and momentum conservation, the threshold energy for achieving collisional excitation is given by [15, 36, 53]

$$\epsilon_{imp} = \frac{1 + 2\mu}{1 + \mu} \epsilon_{corr}, \quad (2.21)$$

where $\mu = m_{\text{con}}/m_{\text{val}}$ is the ratio of the electron mass in the conduction band to the hole mass in the valence band. For equal electron and hole masses ($\mu=1$), the collisional excitation energy is given by $\frac{3}{2}\epsilon_{\text{corr}}$. In this case, Ridley [53] shows that collisional excitation is statistically most probable if an electron $\frac{3}{2}\epsilon_{\text{corr}}$ above the conduction band minimum collides with an electron $\frac{1}{6}\epsilon_{\text{corr}}$ below the valence band maximum, and both electrons end up $\frac{1}{6}\epsilon_{\text{corr}}$ above the conduction band minimum. This is implemented in the model by including the Heaviside step function Θ and the Υ function mentioned in section 2.4.1. As also mentioned in section 2.4.1, the total number of states is chosen such that, as a minimum, the electrons in the highest state always have sufficient kinetic energy for collisional excitation. Hence, the minimum N in equations (2.8)–(2.10) is given by $N = \lceil \epsilon_{\text{coll,max}}/\hbar\omega_l + 1 \rceil$, where the maximum electric-field amplitude of the incoming laser pulse is used to calculate $U_{p,\text{max}}$ and thereby $\epsilon_{\text{coll,max}}$. It should be emphasized that the energy level of the states changes with the ponderomotive shift, so that the kinetic energy of the states is always given by Eq. (2.3).

2.6 Optical properties

Excitation of electrons to the conduction band changes the optical properties of the dielectric material. As mentioned in chapter 1, the complex refractive index (Eq. (1.11)) determines the specific optical properties. In the Drude model, it is given by [9, 49]

$$\tilde{k} = k + i\kappa = \sqrt{\epsilon} = \sqrt{\epsilon_b - \frac{\omega_{\text{pl}}^2}{\omega_l^2 + i\omega_l\Gamma}}, \quad (2.22)$$

where ϵ_b is the contribution to the dielectric function from the bound (valence-band) electrons (see below) and ω_{pl} is the plasma frequency, which is given by

$$\omega_{\text{pl}} = \sqrt{\frac{e^2 n_{\text{con}}}{m_{\text{con}} \epsilon_0}}, \quad (2.23)$$

where ε_0 is the vacuum permittivity. Γ is the electron-scattering rate, which will be discussed in the section 2.6.1.

Clausius-Mossotti correction

The Drude model gives the dielectric function for a free-electron gas, where there are no bound electrons and, thus, $\varepsilon_b = 1$ in Eq. (2.22) [49]. For a dielectric material, the bound electrons contribute to the refractive index. Often, this is incorporated by setting $\varepsilon_b = k_0^2$, where k_0 is the refractive index of the unperturbed material [36, 38, 41, 48, 54]. The dielectric permeability is related to the polarizability of the material, which depends on the density of bound electrons. Hence, as pointed out by Guizard *et al.* [26], ε_b decreases with decreasing valence-band density. The free-electron contribution to the dielectric function is then given by

$$\varepsilon_b = 1 + \frac{3n_{\text{val}}\beta_{CM}}{3 - n_{\text{val}}\beta_{CM}}, \quad (2.24)$$

where β_{CM} is a constant given by

$$\beta_{CM} = \frac{3}{n_{\text{tot}}} \frac{k_0^2 - 1}{k_0^2 + 2}. \quad (2.25)$$

This β_{CM} is derived from the Clausius-Mossotti relation [49], such that $\varepsilon_b = k_0^2$ for $n_{\text{val}} = n_{\text{tot}}$.

Kerr effect

At high light-field intensities, the optical (or AC) Kerr effect may have to be considered as well. As mentioned above, the dielectric function is related to the material polarizability; specifically, it is given as $\varepsilon_b = 1 + \chi_e$, where χ_e is the electric susceptibility. For an inversion symmetric material exposed to an (alternating) optical field of electric-field amplitude E_l , the electric susceptibility can be approximated by [55]

$$\chi_e = \chi_e^{(1)} + \frac{3}{4}\chi_e^{(3)}E_l^2, \quad (2.26)$$

where higher-order terms are neglected, and $\chi_e^{(3)}$ is the third-order

susceptibility. Hence, ε_b is given by

$$\varepsilon_b = k_0^2 + \frac{3}{4}\chi_e^{(3)}E_l^2, \quad (2.27)$$

where, as above, $k_0^2 = 1 + \chi_e^{(1)}$. When the non-linear (last) term is much smaller than the linear, k_b (i.e. the refractive index of an unexcited material due to the bound electrons) can be approximated with a Taylor expansion to the first order

$$k_b = \sqrt{\varepsilon_b} \simeq k_0 + \frac{3\chi_e^{(3)}}{8k_0}E_l^2 = k_0 + k_2I. \quad (2.28)$$

In the last rewriting, k_b is expressed by the light-field intensity and the non-linear refractive index k_2 , which is often stated in the literature. With this notation, $\chi_e^{(3)}$ and k_2 are proportional and related by

$$k_2 = \frac{3}{4\varepsilon_0ck_0^2}\chi_e^{(3)}. \quad (2.29)$$

For most materials, $\chi_e^{(3)}$ is on the order of $10^{-22} \text{ m}^2/\text{V}^2$. Hence, equation (2.28) is valid up to very high electric-field amplitudes of about 10^{10} – 10^{11} V/m . However, since in the simulations for this project, E_l reaches these levels, $\chi_e^{(3)}$ is used instead of k_2 .

The optical Kerr effect must be combined with the ‘‘Clausius-Mossotti correction’’ from Eq. (2.24). Since, both the linear and non-linear susceptibility are caused by the bound electrons, they should both decrease with the valence-band density. Therefore, ε_b is expressed as

$$\varepsilon_b = 1 + \frac{3n_{\text{val}}\beta_{CM}}{3 - n_{\text{val}}\beta_{CM}} \left(1 + \frac{1}{k_0^2 - 1} \frac{3}{4}\chi_e^{(3)}E_l^2 \right). \quad (2.30)$$

With no excitation, the factor in front of the parentheses is $k_0^2 - 1$ and ε_b is given by Eq. (2.27). At full excitation, $n_{\text{val}} = 0$, which gives $\varepsilon_b = 1$, i.e., the classical Drude expression for the refractive index of a free-electron gas.

For the unexcited dielectric, the conduction band is practically empty, since the size of the band gap much exceeds the thermal energy. The

plasma frequency (Eq (2.23)) is then zero, and the refractive index is simply given by the (real) k_0 . However, when the dielectric material is excited ($n_{\text{con}} \neq 0$), the refractive index changes, and the imaginary part (κ) becomes non-vanishing. Changes in the refractive index has several implications. It changes the absorption properties, which affects both the electron heating (Eq. (2.19)) and, in the same process, the propagating light field (see section 2.7). Also, it alters the conditions at the material surface via changes to the reflectance and transmittance (Eq. (1.15)).

2.6.1 Electron-scattering rate

The momentum of the electrons in the conduction band is scattered at a rate Γ . Sometimes, this is expressed in the form of a mean free time between scattering $\tau_{\text{scat}} = 1/\Gamma$. The scattering rate is important to the optical properties of an excited dielectric as it enters into the expression for the refractive index (Eq. (2.22)). In models describing laser-excitation of dielectrics, often, Γ is taken to be constant (e.g. as a fitting parameter) [27, 48, 54, 56]. However, there are also more elaborate models [29, 34, 36, 41, 57, 58] that, e.g., take the electron and lattice temperatures into account. Balling and Schou [2] give an overview of different scattering models applied in the literature.

Our current model includes two different scattering mechanisms: electron-phonon and electron-electron scattering. The electron-phonon scattering, which dominates at low excitation, is assumed to be constant. The specific value for the electron-phonon scattering rate (Γ_{e-ph}) is used as a fitting parameter to obtain the best agreement with experiments; usually it is on the order of 10^{15} s^{-1} . The electron-electron scattering rate (Γ_{e-e}) is based on a classical-gas collision rate [59]

$$\Gamma_{e-e} = 4\pi\sqrt{2}r^2vn_{\text{con}}, \quad (2.31)$$

where v is the root-mean-square (rms) velocity of the electrons. Since this rate describes electron scattering with other electrons, the factor of $\sqrt{2}$ is included to get the relative velocity. r is the effective electron radius. Usually, we have used the electron Debye screening length for the electron radius, which is given by [24]

$$r_{\text{Debye}}^2 = \frac{\varepsilon_0 k_B T_e}{e^2 n_{\text{con}}}, \quad (2.32)$$

where k_B is the Boltzmann constant. The electron temperature T_e is *not* a well-defined quantity at the non-equilibrium excitation densities obtained during the short-pulse-laser interaction. However, the simulations adopt a thermal description, where the average kinetic energy is set equal to $1/2 k_B T_e$ for each degree of freedom, as according to the equipartition theorem. Hence, in the MRE-model, the electron temperature can be determined from the specific electron distribution by

$$\frac{3}{2} k_B T_e = \frac{\sum_{j=1}^N \epsilon_{\text{kin}}(j) n_j}{n_{\text{con}}}, \quad (2.33)$$

where $\epsilon_{\text{kin}}(j)$ is given by Eq. (2.3). The rms-electron velocity is then determined from the temperature via

$$v_{\text{thermal}} = \sqrt{\frac{3k_B T_e}{m_{\text{con}}}}. \quad (2.34)$$

Note that only the kinetic energy related to the individual (random) motion of the electrons is included here, and *not* the ponderomotive energy due to the collective motion (Eq. (2.11)). Combining Eqs. (2.31)–(2.34) gives an electron-electron scattering rate of

$$\Gamma_{e-e} = \frac{4\pi\varepsilon_0}{e^2} \sqrt{\frac{6}{m_{\text{con}}}} (k_B T_e)^{3/2}. \quad (2.35)$$

Surprisingly, this rate does not depend directly on the free-electron density, which is due to the Debye screening length being inversely proportional to the square root of n_{con} . This model for the electron-electron scattering rate is used for the simulations in chapter 3 and Refs. [16, 17, 36, 52] and proves adequate in these investigations that mainly focus on high-intensity (ablation and self-reflectance) experiments.

More recent investigations (chapter 4 and Ref. [18]) also employ lower intensities. These reveal the need for a refinement of the model at low excitation densities. The Debye screening length (Eq. (2.32)) becomes very large for low excitation densities, which at some point

becomes unphysical. In this case, the thermal de Broglie wavelength is used for the electron radius instead, which is given by [60]

$$r_{deBroglie}^2 = \frac{h^2}{3m_{\text{con}}k_B T_e}. \quad (2.36)$$

In practice, for the newer simulations, the minimum of the two radii is simply used: $r = \min\{r_{Debye}, r_{deBroglie}\}$.

Another modification to the model is introduced in connection with the new experiments (chapter 4 and Ref. [18]). At specific (relatively high) intensities, the simulations reveal that the majority of the valence-band electrons are excited to the conduction band. At this excitation, the band structure may have changed significantly. However, when we maintain a description in terms of a separated valence and conduction band, as the conduction-band electrons acquire sufficient kinetic energy, they will collisionally excite the few remaining valence-band electrons thus keeping the average electron temperature relatively low. In this case, the simulated electron-energy distribution actually predicts a thermal electron temperature (Eq. (2.33)) and velocity (Eq. (2.34)), which are less than that minimally allowed by the Fermi-exclusion principle. Therefore, simulations have also been made, in which the Fermi temperature and velocity have been used to put a lower limit on the average electron temperature and velocity. The Fermi energy is given by [60]

$$\epsilon_{\text{Fermi}} = \frac{\hbar^2}{2m_{\text{con}}} (3\pi^2 n_{\text{con}})^{2/3}. \quad (2.37)$$

The Fermi temperature and velocity are derived from this via equations similar to Eqs. (2.33) and (2.34)

$$\frac{3}{2}k_B T_{e,\text{Fermi}} = \epsilon_{\text{Fermi}} \quad \text{and} \quad v_{\text{Fermi}} = \sqrt{\frac{2\epsilon_{\text{Fermi}}}{m_{\text{con}}}}. \quad (2.38)$$

The effect of including the Fermi temperature and velocity is discussed in connection with the presentation of the experimental results in chapter 4.

2.7 Optical field propagation

The intensity of the optical field decreases through the material as strong-field ionization and inverse bremsstrahlung causes absorption of photons. In the current model, the optical field is described by its intensity as a function of depth. A Gaussian time profile of the incoming pulse is assumed (Eq. (1.1)), which gives an intensity immediately below the surface of

$$I(t, z = 0) = T(t) \cdot I_0 \exp \left[-4 \ln 2 \left(\frac{t - t_0}{\tau} \right)^2 \right], \quad (2.39)$$

where $T(t)$ is the time-dependent transmittance as given in Eq. (1.15). I_0 is the peak intensity, which can be related to the peak fluence via Eq. (1.4).

In the model, the decrease in intensity with increasing depth z is assumed to be given by

$$\frac{\partial I}{\partial z} = - \left(\frac{2\kappa\omega_l}{c} + \frac{1}{I} \left[\frac{\epsilon_{\text{corr}}}{\hbar\omega_l} \right] \hbar\omega_l \dot{n}_{SFI} \frac{n_{\text{val}}}{n_{\text{tot}}} \right) I = -\beta I \quad (2.40)$$

where the first and second terms represent plasma absorption and multi-photon absorption due to strong-field excitation, respectively. β is the light absorption per length.

In the simulations, the material is divided into a number of discrete spatial steps. The step size may be constant or vary with the step number. The conduction-band density within a step is assumed to be constant, thus, the step size needs to be small enough for this to be a good approximation. Immediately below the surface, the material excitation as a function of time due to the optical field given in Eq. (2.39) is calculated. Subsequently, the simulation routine goes as follows: For the given material excitation at depth z_i , the related time-dependent light absorption per length, $\beta(t, z_i)$, is calculated. The light intensity at the next step ($z_{i+1} = z_i + \Delta z_i$) is determined as

$$I(t, z_{i+1}) = I(t, z_i) \times [1 - \beta(t, z_i)\Delta z_i]. \quad (2.41)$$

This intensity profile is then used to determine the excitation at z_{i+1} ,

and so forth. The transmittance is only included at the surface, since the refractive index changes continuously inside the dielectric, which does not cause any reflections.

The step size (Δz_i) is chosen such that it is reasonable to assume a uniform excitation (and thus absorption) within a step. Equivalently, the change in the intensity between one step and the next must only be a small fraction of the absolute intensity. Since the excitation and absorption decrease with increasing z , larger step sizes can also be chosen. Especially, at high initial intensities, where the absorption is very high in the outer layers and then decreases significantly within the first few hundred nanometers. Hence, in some simulations, the step size is chosen to increase exponentially away from the surface. In practice, the step size is chosen such that the simulation output shows no visible change when decreasing it.

2.7.1 Intensity and electric-field amplitude

The Keldysh SFI rate (Eq. (2.13)) is calculated from the electric-field amplitude, so a conversion between intensity and electric-field amplitude is needed. Such a conversion may seem trivial, but at high excitation densities, this is not the case.

Loudon [10] calculates how electromagnetic energy propagates through an absorbing dielectric material. The Poynting vector is given by $\mathbf{S} = \varepsilon_0 c \mathbf{E} \times \mathbf{H}$ and represents the rate at which energy per area propagates across a surface. The light-field intensity is the optical-cycle average of the Poynting vector, which Loudon [10] derives an expression for: $\bar{S} = \frac{1}{2} \varepsilon_0 c k E_l^2$. This is also what is used for conversion between intensity and electric-field amplitude in this thesis, see Eq. (1.14).

In the literature, other conversions have been used. Landau and Lifshitz [61] give the mean Poynting vector as: $\bar{S} = \frac{1}{2} c \sqrt{\varepsilon/\mu'} |\mathbf{E}|^2$, where $\mu' = \hat{\mu}/\mu_0$ is the relative magnetic permeability. However, as seen above, ε may be complex, and no immediate explanation of how the equation should be interpreted in this case is given. Simply taking the real part of the right-hand side gives the same expression as above (for $\mu' = 1$). Rethfeld *et al.* [38] use a similar expression: $I = \sqrt{\varepsilon \varepsilon_0 / \mu_0} = \varepsilon_0 c \sqrt{\varepsilon} E_{\text{rms}}^2$, where E_{rms} must be the root-mean-square (rms) electric field, which is related to the electric-field amplitude via $E_{\text{rms}}^2 = \frac{1}{2} E_l^2$. Again, no description for complex ε is given.

The expression used by Kaiser *et al.* [24] (citing Landau and Lifshitz [61]) is slightly modified: $I = c\sqrt{\Re(\varepsilon)}E_{\text{rms}}^2$. The origin of the real-part is unclear, but it solves the problem of complex ε to some extent. However, $\Re(\varepsilon)$ becomes negative at large excitation, which again leads to an equation without real solutions. Medvedev and Rethfeld [62] (citing Kaiser *et al.* [24]) use $I = c\sqrt{|\Re(\varepsilon)|}E_{\text{rms}}^2$, which does prevent the equation from becoming complex. However, the introduced absolute value has no apparent physical justification, and the equation has a singularity around $\Re(\varepsilon) = 0$. Here, a conversion from intensity will give infinitely large electric-field amplitudes, which seems rather unphysical. At low excitation ($\sqrt{\varepsilon} \simeq k$), all the quoted expressions are applicable and give the same results. Still, for this project, a model that applies at all excitation levels is needed, and the current version uses Eq. (1.14).

2.7.2 Photon density

In previous versions of the model, the photon density u is used instead of the intensity to describe the light field. This method is used for the simulations presented in chapter 3 as well as in Refs. [16, 17, 36, 52]. The optical field and its propagation is described by equations similar to Eqs. (2.39)–(2.41), which are then given by

$$u(t, z = 0) = \frac{F_{\text{peak}}T}{\hbar\omega_l c\tau} \sqrt{\frac{\ln 2}{\pi}} \exp \left[-(4 \ln 2) \left(\frac{t - t_0}{\tau} \right)^2 \right] \quad (2.42)$$

$$\frac{\partial u}{\partial z} = - \left(\frac{2\kappa\omega_l}{c} + \frac{k}{c} \left[\frac{\epsilon_{\text{corr}}}{\hbar\omega_l} \right] \frac{\dot{n}_{SFI}}{u} \frac{n_{\text{val}}}{n_{\text{tot}}} \right) u = -\beta_u u \quad (2.43)$$

$$u(t, z) = u(t, z = 0) \prod_{i=1}^{\lfloor z/\Delta z \rfloor} [1 - \beta_u(z_i)\Delta z] \quad (2.44)$$

For the simulations employing the photon-density description, in Eq. (2.44), the material excitation for all the different depths was calculated in one combined simulation, instead of one by one as in the current model. The output of the simulations with the two methods

is the same. However, the new one is faster for large simulations with many depth steps and/or conduction-band energy levels.

Loudon [10] derives an expression for the electromagnetic energy density \bar{W} in a dispersive dielectric: $\bar{W} = \frac{1}{2}(k^2 + 2\omega_l k \kappa / \Gamma) E_l^2$. Ruppin [63] and Nunes *et al.* [64] derive more general expressions for the energy density in dispersive and absorptive materials, and in the case of no magnetic dispersion and $\mu' = 1$, they get the expression derived by Loudon [10]. Hence, the energy density is not only dependent on the real part of the refractive index, but also on the imaginary part as well as the electron-scattering rate. In fact, this implies that the speed at which the energy is propagating inside the dielectric is given by $v_{\text{energy}} = c / (k + 2\omega_l \kappa / \Gamma)$. At low excitation, where $\kappa \ll k$, the “usual” propagation speed of c/k is obtained.

The photon density is equal to the energy density divided by the photon energy, and is thus related to the electric field by

$$u = \frac{1}{\hbar\omega_l} \frac{1}{2} \varepsilon_0 \left(k^2 + \frac{2\omega_l k \kappa}{\Gamma} \right) E_l^2. \quad (2.45)$$

The photon-density version of the model, employs this expression, when converting photon densities to electric-field amplitudes.

2.8 Material response

As discussed in section 2.2, a given material excitation will yield a certain material response. Simulations of the material response can be used to compare the model to experiments. Changes in the optical properties is one material response, which is already included in the model, as described in section 2.6. In chapters 3 and 4, experimental investigations of the optical properties are compared to simulations.

Material removal (i.e. laser ablation) is another direct material response that can be related to the laser-induced excitation. However, this is not part of the model presented above. Hence, some criterion for when ablation occurs must be included. When a substantial fraction of the valence-band electrons are excited to the conduction band, the material becomes unstable and ablation sets in. Therefore, a certain critical density of excited electrons is chosen as the criterion for

ablation to occur. This fixed density criterion has been used by several authors [21, 27, 29, 36]. Often, the so-called critical plasma density (i.e. the density where the plasma frequency equals the laser optical frequency) is used [21, 27, 29]. However, as pointed out by Christensen and Balling [36], the criterion should be independent of the laser wavelength and only depend on the material. In the simulations for this project, the threshold value is a fitting parameter used to obtain the best agreement with experiments. In the literature, there are also examples of ablation criteria given by the energy density [24, 30, 33] and the lattice temperature [34, 41, 65]. The review article by Balling and Schou [2] gives an overview of different ablation models and experiments.

2.9 Simulation output

Numerical simulations based on the model described above are made to enable comparison to various experiments. A suitable range of peak fluences is chosen depending on the application. For each fluence, the simulations provide a detailed description of the material excitation and the optical field as functions of time and depth.

Figures 2.4 and 2.5 show the the output of simulations for fluences of 1 and 8 J/cm², respectively – from hereon referred to as the low-F and the high-F pulses. All other parameters are the same in the simulations. Gaussian pulse shapes with a (FWHM) pulse duration of 70 fs and a wavelength of 800 nm is employed. The material parameters correspond to those for sapphire as given in section 4.3 ($\epsilon_g = 9.9$ eV). The black curve at the back of each panel illustrates the pulse envelope.

Panel (a) in both figures show the excitation density (i.e. the density of electrons in the conduction band). For the low-F pulse, the surface excitation density reaches $\sim 6 \times 10^{17}$ cm⁻³ towards the end of the pulse. It is fairly constant over a 10 μ m range, and only drops to about half over the total investigated depth of 1 mm. A surface density of $\sim 6 \times 10^{22}$ cm⁻³ is attained for the high-F pulse, i.e., about 5 orders of magnitude higher than for the low-F pulse, even though the fluence (and thus the pulse energy and peak intensity) is only 8 times larger. This clearly demonstrates the strong non-linearity of the excitation processes. The high-F density drops faster with depth – in ~ 1 μ m it has decreased by more than an order of magnitude. Hence, at high fluence the excitation is

mainly focused at the surface, while at lower fluences it is more spread out through the sample.

The light-field intensities are shown in panel (b). Immediately below the surface, the pulse is seen to be almost Gaussian, as specified by Eq. (2.39), except for modifications due to the (time varying) reflectance. The low-F intensity shows almost no signs of absorption, while the high-F pulse is strongly absorbed. After 1 mm of propagation, the pulse is severely distorted; the rear end of the pulse (i.e. at long times) has been strongly absorbed in the generated plasma, while the front end propagates much more unperturbed.

The average kinetic energy of the conduction-band electrons is shown in panel (c). The low-F kinetic energy is almost independent of depth, it increases quickly (compared to the density) to about 8 eV and drops a little towards the end of the pulse. The increase is due to plasma heating, and collisional excitation is the reason why it stabilizes. The maximum ponderomotive energy (Eq. (2.11)) for the low-F pulse is about 1 eV. With the 9.9 eV band gap (and assuming equal electron and hole masses), an electron needs a kinetic energy of about $\epsilon_{\text{imp}} \simeq 16.5$ eV to cause collisional excitation (Eq. (2.21)). If the collisional excitation time is significantly shorter than the energy absorption time, the electrons will be relatively evenly distributed in energy up to this energy, which agrees with the ~ 8 eV average kinetic energy. The high-F kinetic energy reaches levels up to about 16 eV at the surface. Now, the maximum ponderomotive energy is ~ 7 eV, giving $\epsilon_{\text{imp,max}} \simeq 25.5$ eV. The average kinetic energy is above half of this, which is an indication of faster absorption times implying that the collisional excitation cannot be assumed to occur instantaneously. At large depths, the average kinetic energy does not reach as high levels, due to the decreased light-field intensity (panel (b)). Towards the end of the pulse, both the low-F and high-F data settle at around 7 eV – again due to collisional excitation. Hence, the large differences seen in excitation densities (panel (a)) are not observed for the kinetic energies. It should be noted that at even higher fluences, when the valence band is depleted ($n_{\text{con}} = n_{\text{tot}}$), the lack of collisional excitation combined with continuing plasma heating leads to much increased average kinetic energies.

Panel (d) shows the electron-scattering rate (Γ). Note, for the low-F pulse, the z -scale only spans from 1 to 1.003 fs^{-1} , meaning that Γ is practically constant. As described in section 2.6.1, for low excitation,

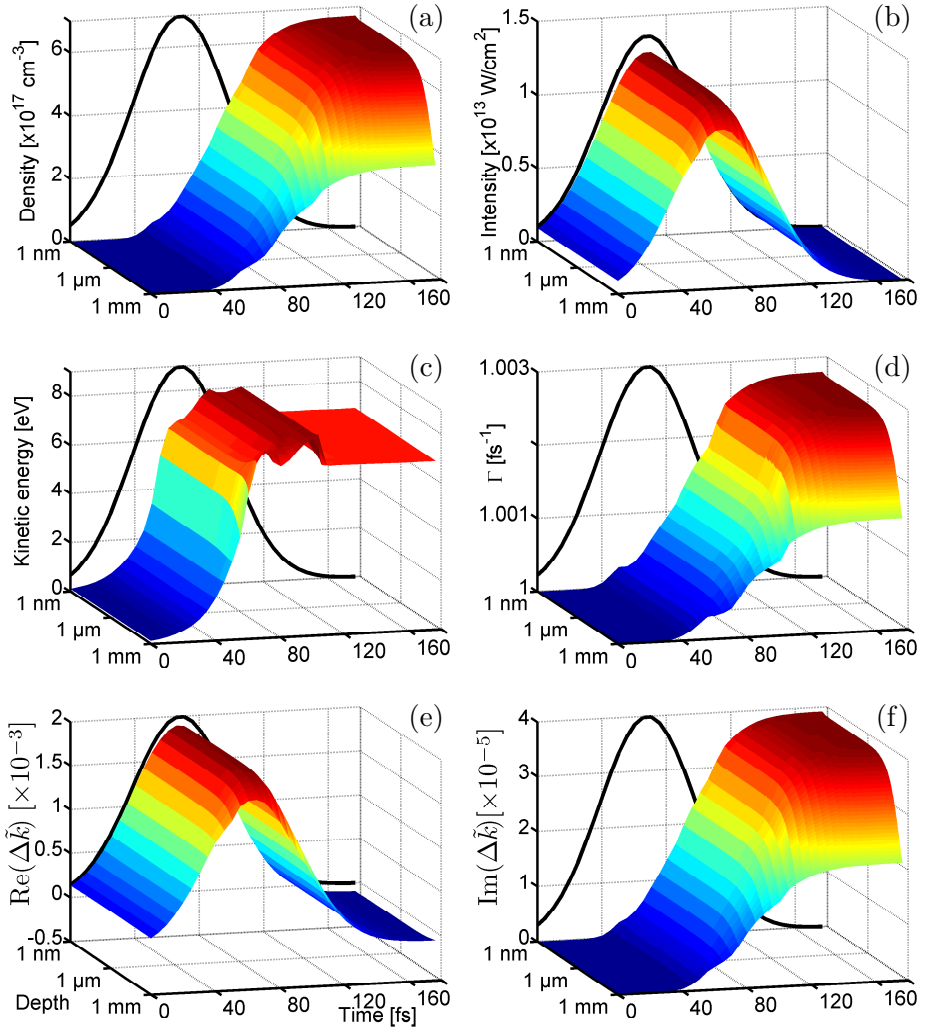


Figure 2.4: Simulation output as a function of depth and time. A peak fluence of 1 J/cm^2 , $\tau = 70 \text{ fs}$, and $\lambda = 800 \text{ nm}$ is used; the material parameters are for sapphire as given in chapter 4. (a) conduction-band density (n_{con}), (b) Light-field intensity, (c) Average kinetic energy of the electrons in the conduction band ($\frac{3}{2}k_B T_e$, Eq. (2.33)), (d) Electron-scattering rate (Γ), (e) Change in real part of refractive index ($\Re(\Delta\tilde{k}) = \Delta k = k - k_0$), (f) Change in imaginary part of refractive index ($\Im(\Delta\tilde{k}) = \Delta\kappa = \kappa$). The lower two axes are the time (in fs) and depth (logarithmic scale); see panel (e). The solid black curve (at 1 nm) illustrates the pulse outside the sample (in arbitrary units for panels (a), (c)-(f)).

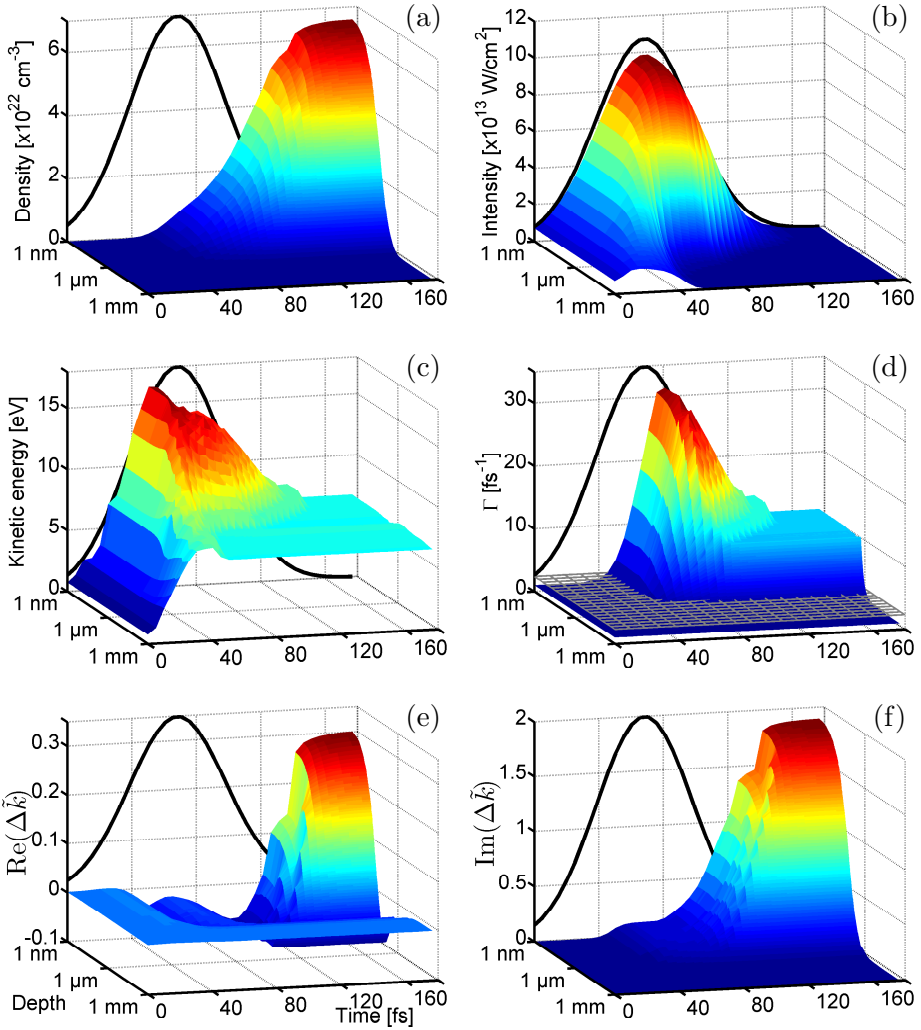


Figure 2.5: Simulation output as a function of depth and time. A peak fluence of 8 J/cm^2 ; otherwise as in figure 2.4. (a) conduction-band density (n_{con}), (b) Light-field intensity, (c) Average kinetic energy of the electrons in the conduction band ($\frac{3}{2}k_B T_e$, Eq. (2.33)), (d) Electron-scattering rate (Γ), grey grid illustrates the laser frequency ($\omega_l = 2.4 \times 10^{15} \text{ Hz}$), (e) Change in real part of refractive index ($\Re(\Delta\tilde{k}) = \Delta k = k - k_0$), (f) Change in imaginary part of refractive index ($\Im(\Delta\tilde{k}) = \Delta\kappa = \kappa$). The lower two axes are the time (in fs) and depth (logarithmic scale); see panel (e). The solid black curve (at 1 nm) illustrates the pulse outside the sample (in arbitrary units for panels (a), (c)-(f)).

the de Broglie wavelength is used as the effective electron radius, when calculating Γ . Had the Debye screening length been used instead (leading to Eq. (2.35)), the scattering rate would have reached levels above 10 fs^{-1} for the kinetic energies shown in panel (c). For the high-F scattering rate the same arguments apply; at low excitation (Time $< 40 \text{ fs}$, Depth $> 1 \text{ }\mu\text{m}$), Γ remains low, and at high excitation, Γ is dominated by electron-electron scattering, where $\Gamma_{e-e} \propto (k_B T_e)^{3/2}$. For comparison, the grey grid indicates the laser frequency ($\omega_l = 2.4 \times 10^{15} \text{ Hz}$). Whether the electron-scattering rate is above or below the laser frequency has a large influence on the optical properties, especially the absorption.

The changes in the real and imaginary parts of the refractive index are shown in panels (e) and (f), respectively. At low-F, the real part is dominated by the optical Kerr effect, which is proportional to the light-field intensity. At the end of the pulse, the small negative changes induced by the material excitation can be observed (from -9×10^{-5} at the surface to -5×10^{-5} at 1 mm). The imaginary part is simply linearly proportional to the density at such low excitation. For the high-F pulse, the picture is very different; note the difference in the z -scales. The change in the real part is negative at low excitation, but becomes positive at higher excitation. The Kerr effect is only slightly recognized as a small top around $t = 60 \text{ fs}$. Changes in the real part reaches about 0.3, which is not just a minor perturbation to the initial refractive index ($k_0 = 1.77$). The imaginary part increases with increasing excitation density. However, when $\Gamma > \omega_l$, κ decreases with increasing Γ , which explains the plateau observed for times between 60 and 80 fs. The final spatial distributions of the changes in the refractive index are very important when comparing simulations to spectral-interferometry experiments, see chapters 4 and 5. The behavior of the reflectance as a function of excitation is described in detail in chapter 3.

The final excitation density (after the pulse is gone) as a function of depth is shown in figure 2.6 (a) for several different peak fluences ($4 - 15 \text{ J/cm}^2$). As described in section 2.8, a fixed excitation density is used as the threshold criterion for ablation to occur. Hence, the largest depth at which the excitation exceeds the criterion, is the ablation depth. The dashed lines in figure 2.6 (a) represent three different threshold densities. The simulated ablation depths corresponding to the three different criteria are shown in figure 2.6 (b) in corresponding colors. The data points indicate the 12 fluences shown in panel (a). As expected, the lower

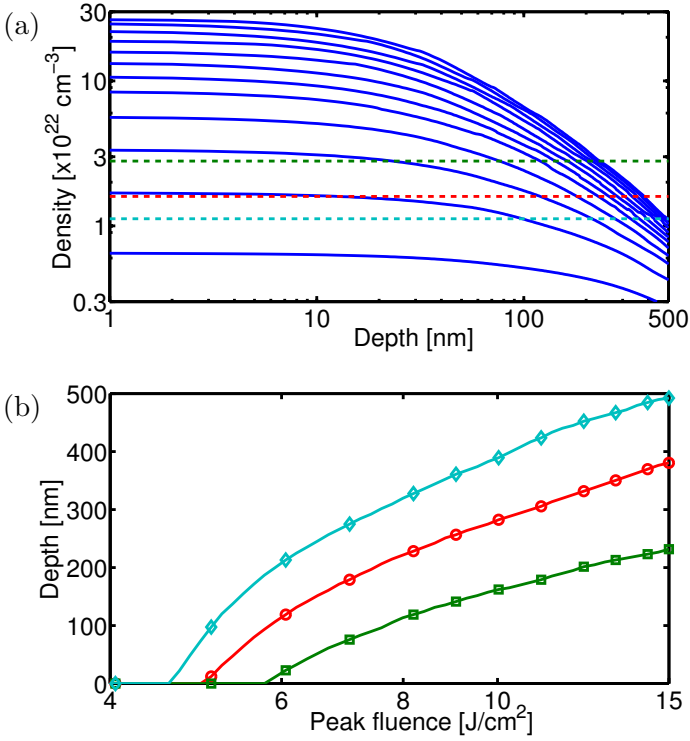


Figure 2.6: Determination of ablation depths. In (a), the blue lines are simulations of the conduction-band density as a function of depth at the end of the simulations. Simulations for fluences at all integer values from 4 to 15 J/cm^2 are shown (the bottom one is for 4 and the top one for 15 J/cm^2). The constant dashed lines represent different ablation-threshold densities of 4 (cyan), 5.7 (red), and 10 % (green) of the total valence band-density. (b) shows the corresponding ablation depths as a function of peak fluence. The data points highlight the fluences shown in the density plot in panel (a).

the threshold the larger the ablation depths. When comparing simulations to experiments, the value for threshold-density is fitted to get the best agreement.

2.10 Discussion and outlook

The model presented in this chapter is quite general as it can be applied to any dielectric material and light field, where the photon energy is significantly smaller than the band gap, so that the excitation process is initiated by non-linear absorption. Also, the pulse duration must be relatively short to justify that electron and heat diffusion as well as electron-hole recombination is omitted during the light-matter interaction. The complexity of the model is ever increasing, e.g., with the introduction of different electron radii for the scattering rate, the Clausius-Mossotti correction, and Fermi energies. Despite this, the model is still relatively simple compared to, e.g., molecular-dynamics models [66, 67], and the numerical simulations can be done on a laptop on an acceptable time scale. Still, it has proven to reproduce experimental data well – even over a large range of light-field intensities.

The model is based on a simplified description of the light-matter interaction, which includes many of the inherent physical mechanisms. However, there are, of course, limitations to the applicability of the model. For example, the band structure is represented by a valence band, with all the electrons initially at the top of the band, and a conduction band with infinitely many states at all energies. One constant effective mass is used for all electrons in the conduction band. Light-field absorption by the holes is not included, and excitation of lower-lying electrons after depletion of the valence band is not considered either. At such extreme excitation, the band structure will have changed significantly, but the fixed band gap description is maintained in the model. In future developments of the model, the actual band structure and density of states could be incorporated, e.g., by ascribing a maximum electron density to each of the discrete conduction band states, and implementing a discretization of the valence band and via this include plasma absorption by the holes. In addition, plasma-absorption rates and collisional-excitation rates that depend on the energy level could be introduced.

The model assumes that electron diffusion to the surrounding material, thermalization of the conduction-band electrons, heat dissipation to the lattice, and electron-hole recombination is minimal and can be neglected on the time scale of the simulations. However, the thermalization, heat dissipation, and electron-hole recombination could be included with appropriate expansions to the rate equations. The diffusion of the

hot electrons is more difficult to incorporate as the model is stationary, and spatial motion is not easily integrated.

The model is restricted to optical propagation in one dimension only, which puts constraints on the focussing conditions for comparative experiments. The focussing must be fairly weak, so that a plane propagating wave can be assumed. It would be very interesting to expand the model to 3-D propagation, as this would allow description of excitation inside the bulk of dielectric materials, which is a field of great interest [3]. Such an expansion requires the inclusion of non-linear propagation effects, and possibly solving Maxwell's equations in 3-D inside the material. In general, it must be admitted that the description of the light-field absorption at large intensities and high excitation is somewhat questionable. As discussed in section 2.7, both intensity and photon-density descriptions have been used in the simulations, and perhaps an electric-field description would be even more appropriate. This subject is definitely worth investigating further for future developments of the model. However, the complexity of the model will increase significantly by including the above-mentioned modifications, thus making the simulations considerably more time consuming.

As mentioned in section 2.6.1, the electron-scattering rate is important to the optical properties of an excited dielectric. The current model only considers electron-electron and electron-phonon scattering, and the latter is simply assumed to be constant. It would be interesting to investigate the implementation of more elaborate models that, e.g., take into account other scattering mechanisms such as electron-ion and electron-neutral scattering [29, 34, 41, 57, 58].

Lastly, a model similar to the one presented here could be developed, which describes the excitation of semiconductor materials by short laser pulses. From the group of Rethfeld who originally suggested the MRE model, Medvedev and Rethfeld [62] have developed a similar model for semiconductors. This model is also based on a set of coupled differential equations, and includes excitation from the valence to the conduction band, which is not necessarily a non-linear (multi-photon) process. As in the dielectrics model, single-photon plasma absorption and collisional excitation is taken into account. Besides this, the semiconductor model also includes Auger recombination, where an electron and a hole recombine and the excess energy is transferred to another free electron. Lastly, energy exchange with phonons is included, which cools the elec-

trons and heats the lattice system. This allows predictions of the lattice temperature and, thus, thresholds for melting and evaporation. A light-propagation structure like the one used in this dielectrics model is currently being applied to develop a similar model to describe the in-depth laser-excitation of semiconductors. Hopefully, this will enable numerical simulations of ablation depths in semiconductors. Laser ablation of semiconductor materials is a topic of great interest [68], and such simulations could provide useful insight into the excitation and ablation mechanisms.

Aarhus experiments: Ablation and self-reflectance

The model presented in chapter 2 describes the interaction between high-intensity ultrashort-laser pulses and dielectric materials. In this chapter, simulations based on the model are compared to experiments of ablation depths and self-reflectance on a single-crystalline sapphire (Al_2O_3) sample. The experiments have been carried out in the laboratory of Peter Balling at Aarhus University. The chapter starts with a descriptions of the experimental setup and the parameters applied in the simulations. The experimental and simulation results for the ablation and reflectance are presented and compared. Finally, the results are discussed and ideas for future developments of the experiment are given.

The work presented in the chapter has led to the publication of two articles: *Femtosecond Laser Excitation of Dielectric Materials: Experiments and Modeling of Optical Properties and Ablation Depths*, Applied Physics A **110**, 601 (2013) [17] and *Femtosecond laser excitation of dielectric materials: Optical properties and ablation*, AIP Conference Proceedings **1464**, 32 (2012) [16].

3.1 Experimental

3.1.1 Setup

The schematic illustration of the experimental setup is shown in figure 3.1. The laser beam is focused onto the sample surface using an achromatic lens with a focal length of 250 mm. The relatively long focal length of the lens ensures a small depth to diameter ratio of the ablated holes – even in the focus where the sample is positioned. This justifies the comparison between the central hole depth and the 1-D simulations. The focal spot size is calculated as $13.4 \pm 0.7 \mu\text{m}$ from the measured spot size before the lens. A flow of helium is applied along the beam focus onto the sample surface to prevent breakdown in the air (and remove laser generated debris). The absence of breakdown and related scattering [69] is confirmed by independent transmission measurements with the sample removed.

The energy of the individual incoming pulses is measured with a calibrated photodiode. An $R/T = 10/90$ beamsplitter is placed in front of the lens. The light reflected from the sample is collected by the lens, and part of this is reflected off the backside of the beamsplitter. This light is focused onto another calibrated photodiode. The reflectance of the individual pulses is determined as the ratio of the reflected to the incoming pulse energies. The measured reflectance thus represents an average over the laser beam profile (both temporally and spatially).

The sapphire sample is a 1" diameter wedge with a maximum thickness of 0.1855" and a wedge angle of 8° . The incoming beam is normally incident on the front surface, and the wedge separates the front- and backside reflections. The backside reflection is blocked so that only the reflection from the front surface is measured with the photodiode. Only single-pulse experiments are made in order to avoid the effects of incubation, and the sample is mounted on a 3-D translational stage to translate it by several beam diameters between shots. The holes ablated in the sapphire sample are analyzed using atomic-force microscopy (AFM).

3.1.2 The laser

In this study, a femtosecond-laser system by Clark-MXR is used. A Ti:Sapphire crystal is pumped by a frequency-doubled Nd:YAG diode

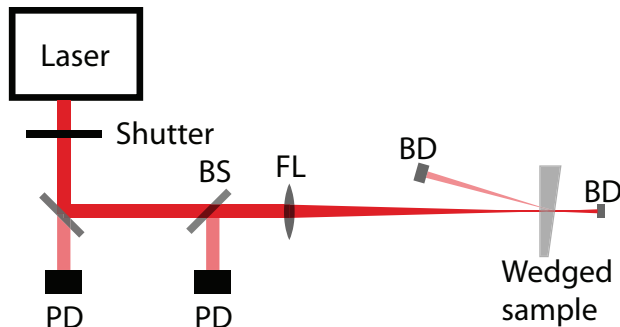


Figure 3.1: Schematic drawing of the experimental setup used for the “Aarhus experiments”. The wedged sample ensures that the backside reflection does not go back into the setup. PD: photodiode, BS: beam splitter, FL: focusing lens, BD: beam dump.

laser, which generates the femtosecond pulses via mode-locking. The pulses are amplified through chirped-pulse amplification (CPA) in a regenerative amplifier, which is pumped by a Q-switched frequency-doubled Nd:YAG laser. The pulses are stretched by giving them a positive chirp, before they are amplified to prevent the pulses from damaging the optical elements inside the amplifier. The coupling of pulses in and out of the regenerative amplifier is regulated by a Pockels cell that thereby controls the number of round-trips per pulse in the amplifier as well as the repetition rate of the laser system. After amplification, the pulses are compressed almost back to their original pulse length. For the experimental results presented in this chapter, the system delivers 795 nm pulses with a duration of about 160 fs at a repetition rate up to 1 kHz, and a maximum power of about 0.7 W corresponding to a pulse energy of 0.7 mJ. The pulse energy is controlled by changing the polarization of the light using a half-wave plate before compressing it. This leads to a decrease in the pulse energy, because the reflection efficiencies of the gratings inside the compressor are strongly polarization dependent. Still, a cube polarizer is positioned immediately before the compressor output to ensure horizontal polarization of the laser beam as it enters the setup. For more detailed descriptions of femtosecond lasers in general, see Ref. [70], and of our specific laser

system, see, e.g., Ref. [71].

3.2 Simulations

Numerical simulations based on the model described in chapter 2 have been made to compare to the two experimentally measured quantities: reflectance and ablation depth. The simulations presented below are based on a pulse duration of 160 fs, a wavelength of 800 nm, and an initial refractive index of 1.77 [72]. The material band gap is set to 6.0 eV for reasons discussed below. The effective conduction-band electron mass and valence-band hole mass have been set to $m_{\text{con}} = 0.38 \times m_e$ and $m_{\text{val}} = 3.99 \times m_e$ [73], respectively, where m_e is the free electron mass. The total electron density was set to $n_{\text{tot}} = 10^{23} \text{ cm}^{-3}$ and the collisional excitation rate to $\alpha = 10^{15} \text{ s}^{-1}$. A constant electron-phonon scattering rate of $\Gamma_{e-ph} = 2 \times 10^{15} \text{ s}^{-1}$ is used, and the electron-electron scattering rate is scaled up by a factor of 1.25 relative to the semi-classical expression in Eq. (2.35). The ablation-threshold criterion is set to 13 % of the valence-band electrons being excited to the conduction band, which corresponds to a density of $1.3 \times 10^{22} \text{ cm}^{-3}$. The experiments measure the self-reflectance of pulse that also causes the excitation. To allow comparison with the experiments, the simulated reflectance is, thus, averaged over the Gaussian temporal *and* spatial profile of the pulse.

3.2.1 Sapphire band gap

Figure 3.2 shows the transmission spectra for two different sapphire samples. The spectra are measured with a spectrophotometer (Thermo Scientific Evolution 300 UV-Vis). The solid red line shows the transmission for the wedged sapphire sample used for the experiments presented in this chapter. In comparison, the dashed blue line is the transmission of a so-called UV-grade sapphire sample, which is used for the experiments presented in chapter 4. The current sample has a significant dip in the transmission starting at around 230 nm and extending down beyond the measurement range of the spectrometer, which only goes to 190 nm. The transmission is minimal around 205 nm, which corresponds to a photon energy of 6.0 eV. The transmission dip is most likely due to color centers in the sample, which are crystallographic defects [49]. The color centers introduce new absorption channels – in this case at wavelengths around

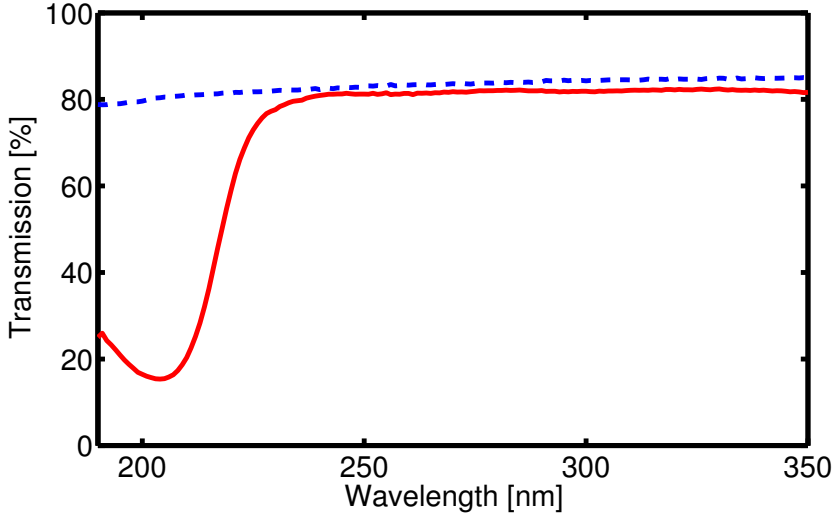


Figure 3.2: Transmission spectra for two sapphire samples measured with a spectrophotometer. The solid red line is for the wedged sapphire sample used in these experiments, and the dashed blue line is for a UV-grade sapphire sample used for the experiments described in chapter 4. The sample used in this part has a distinct dip in the transmission centered around 205 nm (corresponding to 6.0 eV), which is not observed in the UV-grade sample.

205 nm. In the literature, the band gap of defect-free sapphire is stated to be from 8.3 [74] and 8.8 [26, 75] up to 9.9 eV [3, 76, 77].

As mentioned in chapter 2, the excitation rate for non-linear processes decreases significantly with the order of the process, as can be seen from, e.g., Eq. (2.16). Hence, the lowest-order process, which is possible, usually dominates the strong-field excitation. Therefore, it is believed that excitation of sapphire with color centers by 800-nm light is more likely to be dominated by the 6 eV (4 photons) absorption feature, compared with the 8.3–9.9 eV band gap (6–7 photons). This is the reason for using the 6 eV band gap in the simulations for these experiments.

3.3 Results

Reflectance

Figure 3.3 shows experimentally measured and simulated reflectance data as a function of fluence. The data show that, as expected, the reflectance increases for increasing fluence due to the creation of the electron plasma, for this reason sometimes denoted by a plasma mirror. At even higher fluence, the reflectance does, however, decrease again. This – maybe initially somewhat surprising – behavior can be understood by examining the expression for the refractive index, see Eq. (2.22). At high fluences, the majority of the valence-band electrons are excited to the conduction band during the pulse at which point the plasma frequency, Eq. (2.23), saturates. However, the heating of the electrons by plasma absorption continues, which increases the scattering rate, as captured also by the semi-classical expression for Γ_{e-e} , Eq. (2.35). This apparently eventually reduces the reflectance. Note that this only happens when the saturation occurs during the pulse, so that the plasma absorption continues, and not if saturation is only reached subsequently by collisional excitation.

The combination of the increase in the scattering rate and the saturation of the plasma frequency influences the reflectance, as seen in figures 3.4 and 3.5. In figure 3.4, simulations of the temporal evolution of the instantaneous reflectance during illumination for three different fluences are shown. Figure 3.5 is a surface plot of the reflectance as a function of electron-scattering rate and conduction-band electron density, as calculated purely from the Drude model, Eqs. (1.15) and (2.22). In this calculation, the Clausius-Mossotti correction (section 2.6) has not been included, however, including this does not change the plot significantly. The temporal tracks of the same three fluences are also shown (starting from the front right), and here the specific values of Γ and n_{con} that cause the individual reflectances can be seen.

For low fluences (black curves in figures 3.4 and 3.5), where the density of excited electrons does not saturate, the reflectance increases throughout the duration of the pulse. For higher fluences (green curves), the initial increase in reflectance is also observed, but towards the end of the pulse when saturation is reached, the reflectance decreases again. Also, already during the excitation, the electrons are heated more than in the low-fluence case. This means that the maximum instantaneous

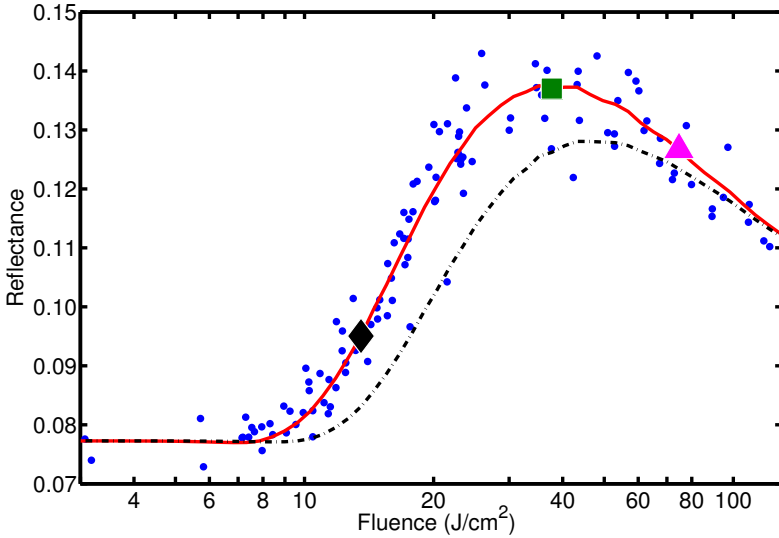


Figure 3.3: Measured (blue data points) and simulated reflectance for sapphire (red solid line). Simulations with the previous value for the electron-scattering rate ($\Gamma_{e-l} = 5 \times 10^{15} s^{-1}$ and Γ_{e-e} given by Eq. (2.35)) is shown for comparison (black dash-dotted line). The black diamond, green square, and magenta triangle at fluences of 15, 40, and 80 J/cm², respectively, correspond to the fluences shown in figures 3.4, 3.5, and 3.6.

reflectance reached for the green curves is not as high as for the black curves. At even higher fluences (magenta curves), saturation sets in earlier and the heating during excitation is even more pronounced. Hence, the reflectance does not reach a very high maximum and starts to decrease quickly.

The overall pulse reflectances for the three different peak fluences shown in figures 3.4 and 3.5 are highlighted with symbols of corresponding colors in figure 3.3. The pulse reflectance for a specific fluence is calculated from the instantaneous reflectance averaged over the pulse envelope. In addition, the simulated reflectances shown in figure 3.3 are averaged over a spatially Gaussian laser-beam profile to allow comparison to the experimentally measured reflectances. It should be noted that even though the temporally and spatially averaged reflectance only goes up to about 14 %, the simulations actually predict instantaneous re-

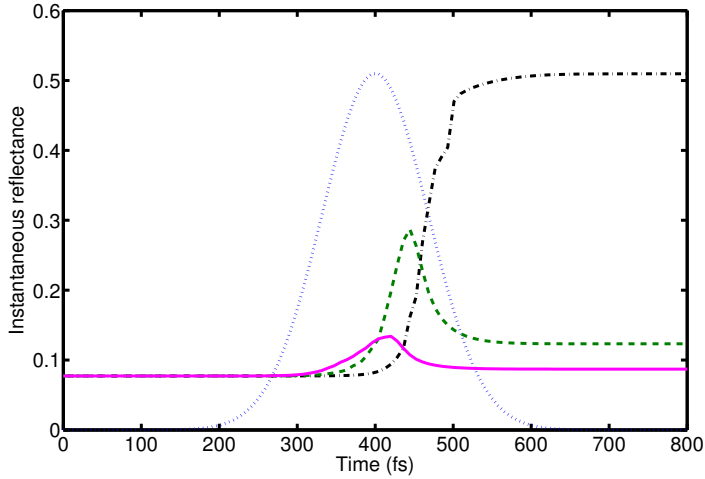


Figure 3.4: Simulations of the temporal evolution of the instantaneous reflectance for fluences of 15 (black dash-dotted), 40 (green dashed), and 80 J/cm² (magenta solid). The overall pulse reflectance for these fluences are highlighted in figure 3.3. The blue dotted curve shows the pulse envelope (in arbitrary units).

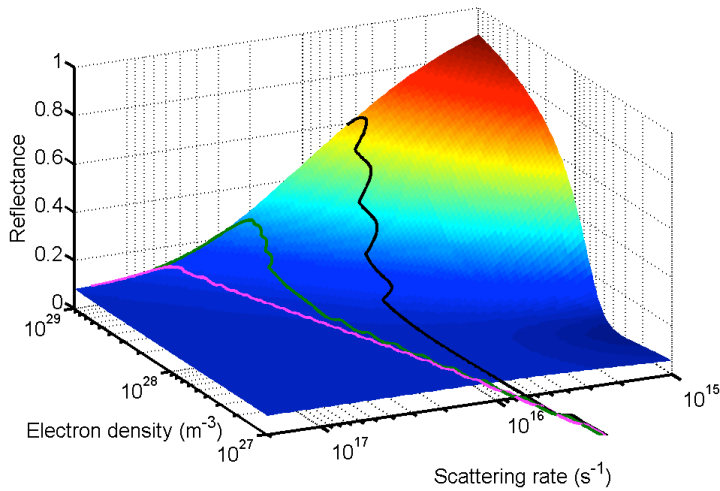


Figure 3.5: Surface plot of the reflectance as a function of electron-scattering rate (Γ) and conduction-band electron density (n_{con}). The calculated reflectance is purely calculated from the Drude model, Eqs. (1.15) and (2.22), without inclusion of the Clausius-Mossotti correction (section 2.6) The curves correspond to those in figure 3.4.

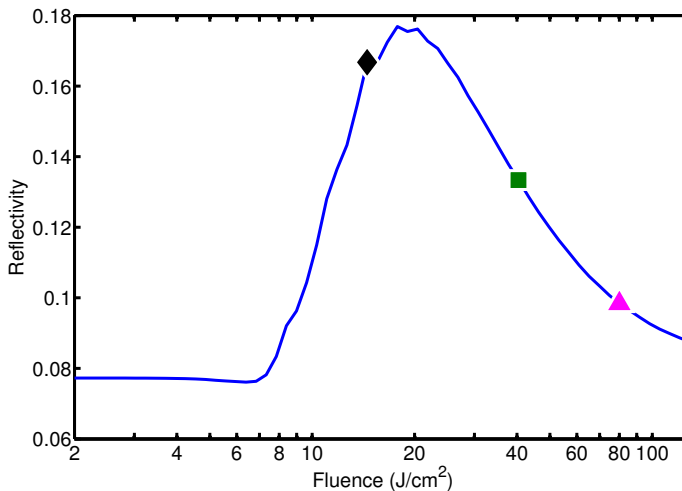


Figure 3.6: Simulated temporally-averaged reflectance as a function of peak fluence. The colored data points at 15, 40, and 80 J/cm² correspond to the fluences that are also shown in figures 3.3, 3.4, and 3.5. Here, the reflectance is seen to rise quicker and decrease at lower fluences compared to in figure 3.3.

reflectances (not spatially averaged) above 50 %. The temporally averaged reflectance *without* spatial averaging is shown in figure 3.6. Without the spatial averaging, the reflectance rises quicker and reaches a higher maximum value ($\sim 18\%$) already at a fluence of ~ 20 J/cm² – compared to $\sim 14\%$ at a fluence of ~ 40 J/cm² in figure 3.3. At the highest investigated fluences, the non-spatially-averaged reflectance almost reaches values down to the initial (Fresnel) reflectance. Also, of the three fluences investigated in detail, the highest level is actually reached for the lowest fluence. From figure 3.4, it can be seen that for this “low” fluence, by far the highest instantaneous reflectance is also reached. However, the 40 J/cm² pulse has outer spatial regions with high reflectance and still a moderate reflectance in the center. Hence, the spatially-averaged reflectance is significantly higher than for the 15 J/cm² pulse.

The decrease in reflectance demonstrates the necessity of a saturation term in the simulations as well as a temperature-dependent scattering rate. This is confirmed by simulations without a temperature-dependent

scattering term, which predict a pulse reflectance that increases monotonically (saturates but never decreases).

Ablation depth

Figure 3.7 shows experimentally measured and simulated ablation-depth data as a function of fluence. Examples of AFM images similar to the ones that were used to determine these hole depths are shown in chapter 4 (figure 4.3). The simulations reproduce the threshold for ablation to set in as well as the initial increase quite well. However, the data and simulations clearly deviate at high fluences; possible explanations for this are discussed in section 3.4. It should be emphasized that agreement with the depth data is not enough to put severe constraints on the model parameters for the optical properties. However, in combination with the reflectance data, it is now possible to improve the values for the optical parameters. In previous work of the group, an electron-lattice scattering rate of $\Gamma_{e-lat} = 5 \times 10^{15} \text{ s}^{-1}$ was applied (and provided agreement with the depth data [52]). However, this value does not quite reproduce the rapid increase in the reflectance observed in the data; it should be significantly lower. For comparison, the black dash-dotted curve in figure 3.3 shows the reflectance obtained with the optical parameters from the group's earlier papers [36, 52].

Other authors have actually reported that their data are in good agreement with a somewhat lower scattering rate; for instance Puerto *et al.* [78] apply $5 \times 10^{14} \text{ s}^{-1}$ for the total scattering rate. Our data are not consistent with such a small scattering rate; it would give much too high reflectances and also, as mentioned above, the constant scattering rate does not reproduce the observed decrease in reflectance at high fluences. While we are thus able to constrain the model parameters in form of the total scattering rate, it is more difficult to fix precisely the ratio between the electron-lattice and the electron-electron rates. We obtain a good agreement with the reflectance data and acceptable agreement with the depth data when using $\Gamma_{e-ph} = 2 \times 10^{15} \text{ s}^{-1}$ and Γ_{e-e} scaled up by a factor of 1.25 relative to the semi-classical expression, Eq. (2.35).

The present comparison indicates that the appropriate critical density for ablation is around 13 % or an absolute density of $1.3 \times 10^{22} \text{ cm}^{-3}$. Note that the optical measurements are independent of the choice for this number; it only influences the calculated ablation depth.

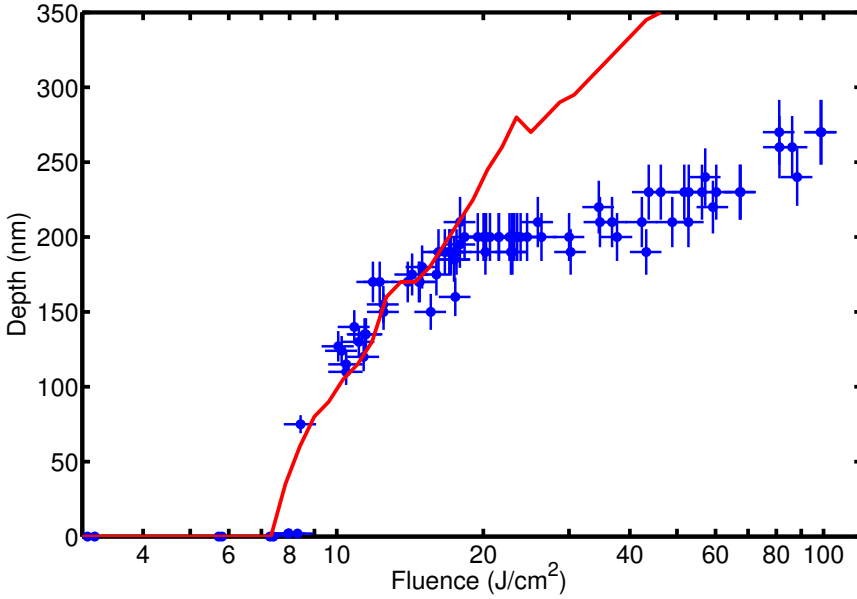


Figure 3.7: Measured (blue data points with error bars) and simulated (red solid line) ablation depths for sapphire. Parameters are as in figure 3.3. The ablation criterion is set to 13 %.

3.4 Discussion and outlook

As can be seen in figure 3.7, at high fluences, the experimentally measured ablation depths are evidently lower than the simulated ones. There are several possible explanations for this disagreement. The simulations do not include the band structure of the conduction and valence bands. In reality, there is a maximum possible electron density in the lowest conduction band states, and all the valence band electrons are not at the top of the valence band as assumed in the simulations. Also, single-photon absorption in the valence band (i.e. by the holes) is not included. The shift in photon energy (i.e. red- and blueshifts) during propagation due to the ponderomotive shift of the electrons is not included in the simulations either. The front end of the pulse is redshifted, because energy is transferred from the photons to the conduction-band electrons corresponding to the ponderomotive potential. The opposite happens on

the rear end of the pulse, which is blueshifted. The effect of this is that the photons in the front end of the pulse (i.e. those that penetrate the deepest into the sample, see figure 2.5 (b)) have a lower photon energy, which strongly decreases the rate of strong-field ionization and hence may cause a lower density of excited electrons. The omission of this effect could possibly explain why the simulations give higher excitation densities and thereby larger ablation depths than what is measured experimentally. It is also possible that the fixed-excitation-density criterion for ablation is simply inadequate at such high fluences. Other models for converting a given electronic excitation to a material response should be considered in future developments of the model.

Large variations in the saturation depths ranging from below 200 nm to above 500 nm have been measured by different groups with similar experimental parameters [18, 26, 52, 78]. For example, in an earlier work of our group [52], the saturation depth is above 500 nm. The same laser system is used as for the data presented here, where the hole depth only reaches about 250 nm. Different focussing conditions were used in the two experiments. However, this should not affect the hole depths when the spot size is much larger than the ablation depths, which is the case in both experiments. The utilized sapphire samples were also different in the two experiments. In general, the large variations in hole depths between the different experiments may suggest a strong dependence on the specific material at hand. Color centers or other defects and the density of these could be an important parameter. As mentioned in section 3.2.1, color centers introduce new absorption channels, which may change the excitation profile significantly and cause the observed changes in ablation depths.

In this chapter, experiments and simulations of the ablation depth and self-reflectance of sapphire are presented. The threshold for ablation to set in and for changes in the self-reflectance to occur are roughly the same ($\sim 8 \text{ J/cm}^2$), which relates to the onset of optical breakdown ($\omega_{\text{pl}} = \omega_l$). The high fluences and, thus, extreme excitation levels that are needed to get information from these experiments means that the model is only tested in this regime. Experiments that can detect smaller excitation levels will provide the possibility to test the model further. Chapter 4 presents such an experiment, which is based on a pump-probe spectral interferometry setup. Since the optical properties are determined with a delayed probe pulse, the reflectance can also be measured

independently, i.e., instead of the self-reflectance. From figure 3.4 it can be seen that the simulations predict instantaneous reflectances up to about 50 %. If the simulations are correct, such high reflectances should be observed in the pump-probe experiments. Note, this is without spatial averaging; lower signals should be expected if not only the central part of the pump pulse is probed.

Ideas for the future development of the model and simulations are described in section 2.10. With regard to experiments like those presented in this chapter, the project is already progressing. New experiments on other dielectric samples such as CaF_2 , MgF_2 , and TeO_2 are under way, and will provide new data to compare to the model. In addition, experiments on different crystallographic facet planes of the same material could reveal if this has an influence on the reflectance and ablation depths and thresholds. An investigation by Qi *et al.* [79] shows that the choice of crystallographic facet plane has little effect on femtosecond-laser ablation of sapphire, but this might be different for other materials.

Future experiments will – hopefully – also involve an extension of the current setup to allow time- and wavelength-resolved measurements. This requires a pump-probe setup and, e.g., a tunable optical parametric amplifier system (TOPAS). The optical properties are highly dependent on the laser frequency, and a wavelength-tunable probe pulse would enable more precise determination of the material excitation as well as other parameters (e.g. the electron-scattering rate).

CEA experiments: Spectral interferometry, reflectance, and ablation

This chapter describes an experiment carried out in collaboration with the group of Professor Stéphane Guizard at the “Centre Energie Atomique” (CEA) in Sacclay, France. The experiment utilizes a pump-probe setup that combines spectral interferometry with reflectance and ablation depth measurements on sapphire. Spectral interferometry is an optical measurement technique, which enables measurements at significantly lower material excitation than was, e.g., possible in the experiment presented in chapter 3. The concept and advantages of spectral interferometry is introduced, and the experimental setup is presented. New probe-pulse simulations are described that allow comparison of the experiment to the model presented in chapter 2. The experimental results and simulations are compared and discussed. Finally, preliminary data for quartz (SiO_2) are presented.

The work presented in this chapter has led to the article entitled: *A comprehensive model for excitation of dielectrics by a short, intense laser pulse*, Physical Review Letters, submitted (2013) [18].

4.1 Introduction

Optical interferometry is a technique based on superposition of electromagnetic waves, which gives information about the waves, such as their phase and/or amplitude. Femtosecond optical interferometry has been used in different pump-probe configurations to quantify the excitation of various samples, especially dielectrics. In spatial interferometry, a probe pulse is reflected from or transmitted through the sample that wants investigated. The probe pulse is interfered with a reference pulse, which propagates in another arm of a Mach-Zehnder interferometer. The spatial interference pattern is recorded, and the phase shift and absorption experienced by the probe pulse can be extracted by Fourier analysis. Based on spatial interferometry, Temnov *et al.* [80] demonstrate a femtosecond time-resolved interferometric microscope capable of determining the surface reflectance and a phase shift, which can be converted to a hole depth. In another paper by the same group, Temnov *et al.* [81] use spectral interferometry in a sample-transmission scheme to compare excitation of a dielectric by circularly and linearly polarized femtosecond pulses.

In spectral interferometry (also known as frequency-domain interferometry), the probe and reference pulses are given a fixed temporal offset in a Michelson interferometer but propagate along the same path. The pulses are interfered in a spectrometer and the spectral interference pattern recorded on a charge-coupled device (CCD). Fourier analysis can be used to determine the phase shift and absorption. Usually, the Michelson interferometer is placed before the sample. This way, the sample-excitation (by the pump pulse) can be set to occur between the probe and reference pulses. Hence, the phase shift and absorption only apply to the last pulse (the probe). However, the setup used in the present experiment is a little different as the Michelson interferometer is situated after the sample; see section 4.2. Already in 1992, Tokunga *et al.* [82] demonstrate the capability of determining pump-induced phase shifts by femtosecond time-resolved spectral interferometry. Geindre *et al.* [83] use the technique to make space- and time-resolved phase measurements of a laser-induced plasma on an aluminum surface. The spatial resolution is obtained by having a narrow slit at the spectrometer entrance which is perpendicular to the direction of the spectral splitting caused by the grating. The two dimensions of the CCD can then be related to

the spatial and frequency components of the pump pulse, respectively. Now, the spectral interferometry technique has been applied in several different schemes and to study various physical mechanisms and materials [20, 22, 48, 54, 84, 85].

The current study combines transmission spectral interferometry with reflectance and ablation depth measurements. As seen in chapter 3, the interesting fluence range for the reflectance and ablation depth is at quite high fluences, when optical break down sets in. Contrary to this, transmission spectral interferometry in fact requires that the excitation is not too high. Otherwise, the probe pulse will be completely absorbed and impossible to measure. Spectral interferometry, thus, provides a strong supplement to the “Aarhus experiment”. Here, the detailed time-resolved measurements of optical properties at comparatively low excitation is combined with high-intensity measurements of time-resolved reflectance and ablation depth – in one comprehensive experiment. Furthermore, since the experiment employs a pump-probe setup, the probe reflectance is measured instead of the self-reflectance. As discussed in section 3.4, this should result in higher peak reflectances and easier comparison of experiments and simulations.

4.2 Experimental setup

The experiment is carried out with a pump-probe setup that combines time-resolved spectral interferometry and reflectance measurements. A schematic drawing of the setup is shown in figure 4.1. A mode-locked Ti:Sapphire laser operating at a central wavelength of 800 nm is used. The output of the oscillator is amplified in a multipass amplifier at a 20 Hz repetition rate yielding a minimal pulse duration of 70 fs. A beam splitter splits the beam into a pump (95%) and a probe (5%) beam. A 4-mm aperture and a 300-mm focusing lens is used to focus the most intense part of the beam onto a single-crystal sapphire sample (0001) at normal incidence, giving a spot size (ω_0) of 49 ± 2 μm . The sample thickness is 1 mm. A computer-controlled shutter ensures single-shot operation. The energy of the pump pulse is controlled by a rotatable half-wave plate and a polarizer.

The probe beam is sent through a computer-controlled delay line determining the time delay between the pump and probe pulses. A

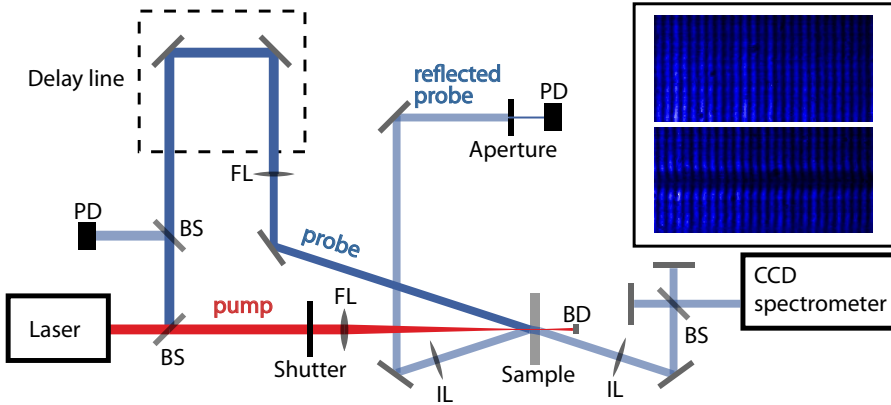


Figure 4.1: A schematic drawing of the experimental setup. The blue beam is the probe and the red the pump. The colors are only for visualization and are not related to the wavelength, which is 800 nm for both beams. BS: beam splitter, FL: focusing lens, IL: imaging lens, PD: photodiode, BD: beam dump. The inset in the top right shows two examples of CCD recordings with (bottom) and without (top) material excitation, see text for details.

1000-mm focusing lens focuses the probe beam onto the sample under an angle of 18° . With a refractive index of 1.77 for sapphire at 800 nm, inside the sample the probe beam is propagating at an angle of $\sim 10^\circ$ relative to the pump. The spot size of the probe beam is approximately $200\ \mu\text{m}$, which is much larger than that of the pump.

A Michelson interferometer splits the transmitted part of the probe into two identical pulses that are separated in time and slightly in space. The two pulses are interfered in the frequency domain by a spectrometer, and the resulting fringe pattern is recorded with a high-resolution CCD. The advantage of splitting the probe pulse after the sample is that it removes the limitations on the pump-probe time delay. This is in contrast to other spectral-interferometry experiments, where the probe splitting is done before the sample and, hence, the pump-probe delay is limited by the separation of the two probe pulses. The splitting after the sample is enabled by the size of the probe beam much exceeding that of the pump. However, this large-time-delay capacity is not fully exploited in

these experiments. Time delays up to only a few picoseconds are used, which can also be achieved with a “conventional” spectral-interferometry setup. In another experiment carried out by the group of Guizard at CEA, Mouskeftaras *et al.* [84] utilize the novel setup in a double-pump study investigating the role of avalanche excitation in sapphire.

The inset in figure 4.1 shows an example of the fringe pattern recorded by the CCD. The horizontal axis is a frequency (or wavelength) axis in which the fringes appear. The specific frequency values are unimportant, which is why no units or labels are given. The vertical axis corresponds to a spatial (vertical) selection of the probe beam. In the spatial center, the fringe pattern is seen to be offset and attenuated compared to at the edges. This is due to the material excitation caused by the pump pulse, which leads to the phase shift (offset) and absorption (attenuation). A line-wise Fourier transform of the image provides the absolute values for the absorption and phase shift experienced by the central part of the probe pulse.

At very low pump-pulse intensities, there is no measurable material excitation. However, during the pump-probe overlap, a phase shift will be induced due to the optical Kerr effect (see section 2.6). Figure 4.2 shows an example of such a low intensity “Kerr-measurement”. The phase shift is shown as a function of the vertical spatial coordinate x (panel (a)) and the pump-probe time delay (panel (b)). The change in the refractive index and, thus, the induced phase shift resulting from the Kerr effect are linearly proportional to the intensity of the pump pulse (see Eq. (2.28)). The temporal width (figure 4.2 (b)) can be used to determine the pulse duration, and the spatial width of the profile (figure 4.2 (a)) gives the spot size of the pump beam. Simulations, as described in chapter 2 and section 4.3, were made which only included the Kerr effect (*no* material excitation and pump pulse absorption). These simulations revealed that the measured spatial width is identical to the actual pump beam spot size. However, the measured temporal width is about a factor of $\sqrt{2}$ larger than the actual pulse duration. The non-co-linear geometry is the reason why this is not exactly $\sqrt{2}$ as for an autocorrelation. The precise value is above $\sqrt{2}$ and increasing with decreasing pulse duration; for a pulse duration of about 70 fs, the scaling factor is ~ 1.44 . Gaussian fits to the two profiles are shown in figure 4.2. From these fits, the pulse duration is found to be 72 ± 4 fs, and the spot size 49 ± 4 μm . A third-order susceptibility of $\chi^{(3)} = 1.7 \times 10^{-22} \text{ m}^2/\text{V}^2$ is used in the simulations

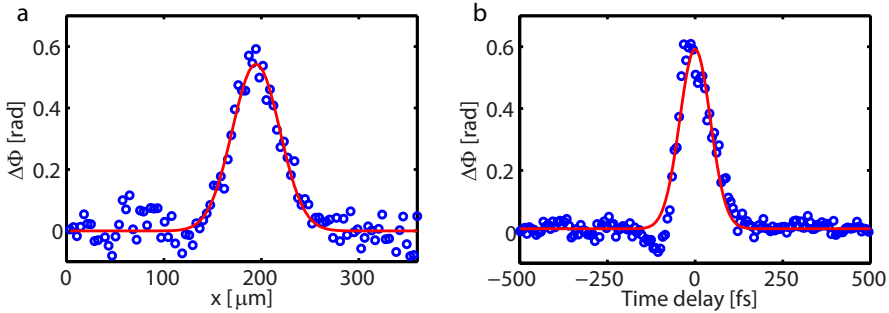


Figure 4.2: Phase shift due to only the Kerr effect as a function of the spatial coordinate x (a) and pump-probe time delay (b). (a) is taken at a time delay around 0 fs and (b) is an average over the spatially central part of the pulse, where the phase shift is maximal. The spatial coordinate x corresponds to the vertical axis on the inset in figure 4.1. The blue circles are experimental data and the red lines are Gaussian fits. The widths determined from the fits are: (a) $49 \pm 4 \mu\text{m}$ (ω_0 , half-width at $1/e^2$), (b) 103 ± 6 fs (FWHM).

as it gave the best agreement with the experimental data. This value is about half of what has been reported in a previous study [86].

In addition to the spectral-interferometry measurements of absorption and phase shift, the setup allows measuring the time-resolved reflectance. The reflected part of the probe beam is imaged onto an aperture picking out the central region of the probe, which is overlapped by the pump (corresponding to a diameter of $\sim 25 \mu\text{m}$ at the surface). A photodiode (PD) measures the energy of the reflected probe light that goes through the aperture. Before the probe-beam-focusing lens, a glass window reflects a small fraction of the probe beam. Another photodiode measures the energy of this beam, which is used as a reference signal giving the fluctuation in the energy between individual pulses. The ratio of the reflectance to the reference PD-signal is directly proportional to the absolute reflectance. Measurements without a pump beam or for negative time delays are set equal to the theoretical Fresnel reflectance; hence, they are used to determine the proportionality constant (conversion factor).

Subsequently, the laser-induced craters are analyzed with AFM to

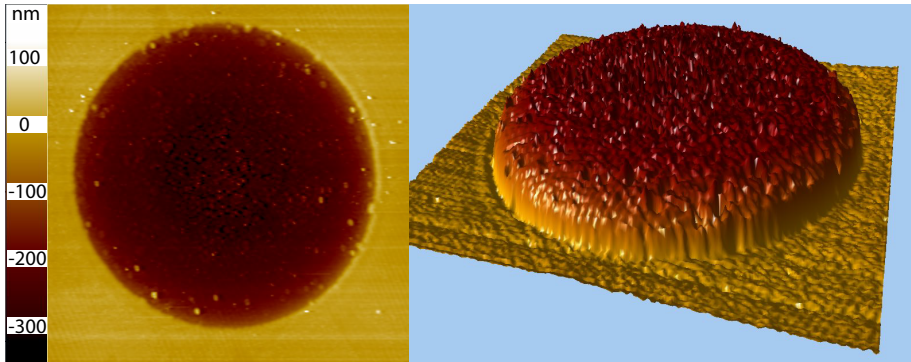


Figure 4.3: AFM image of a hole ablated with a peak fluence of 10.8 J/cm^2 . To the left is a 2-D top view image, where the color illustrates the depth – the absolute z -scale is given in the color bar to the left of the image. The image dimensions are about $65 \times 65 \mu\text{m}^2$. To the right is a 3-D illustration of the hole as seen from below. Note that the individual axes are not to scale. The z -scale is magnified so that the hole appears deeper than in reality, where the depth-to-width aspect ratio is only about 1:200.

determine the hole depths. To allow this and to avoid cumulative effects, the sample is displaced between each laser pulse. Figure 4.3 shows an example of an AFM image of a hole produced with a peak fluence of 10.8 J/cm^2 . In the 3-D image to the right, note that the individual axes are *not* to scale, as the depth-to-width aspect ratio of the hole is only about 1:200. The depths given in section 4.4 are evaluated as an average over the central most part of the hole.

4.3 Simulations

Numerical simulations are made that aim to reproduce the experiments, where four different quantities have been measured: phase shift, absorption, and reflectance of the probe pulse as well as the ablation depth. In chapter 3, only ablation depth and *self*-reflectance was measured. As will be seen in section 4.4, the “new” quantities (phase shift and absorption) generally evolve at lower light-field intensities – significantly below the threshold for optical breakdown – giving a large intensity span (more

than a factor of 25).

The model that is the basis for the simulations is described in detail in chapter 2. Minor refinements of the model have been adopted compared to what was used in chapter 3. Some are due to the general continuing development of the model; such as the utilization of the full Keldysh expression for the strong-field excitation (see section 2.5.1) and the switch from a photon density to an intensity description of the light field (section 2.7). Other refinements was motivated by the fact that the simulations can now be compared to experiments at lower intensities. This includes the upper limit on the electron radius set to the de Broglie wavelength, which is used to calculate the electron-electron scattering rate (section 2.6.1). The modifications mainly have an effect in the low-intensity regime and are still compatible with previous experimental results obtained at only high intensities.

The simulations are based on a band gap of 9.9 eV [3, 76, 77], pump and probe wavelengths of 800 nm, initial refractive index of 1.77 [72], an initial valence-band density¹ of $n_{\text{tot}} = 2.8 \times 10^{23} \text{ cm}^{-3}$, and a collisional excitation rate of $\alpha = 10^{15} \text{ s}^{-1}$. For the ablation-depth simulations, the criterion for ablation is set at 5.7 % of the valence-band electrons being excited to the conduction band, corresponding to a density of $1.6 \times 10^{22} \text{ cm}^{-3}$. An overall scaling of the electron-electron scattering rate by a factor of 1.45 compared to Eq. (2.31) is adapted, and a constant electron-phonon scattering rate of 10^{15} s^{-1} is applied. The effective conduction-band electron and valence-band hole masses are set to $m_{\text{con}} = 0.38 \times m_e$ and $m_{\text{val}} = 3.99 \times m_e$, respectively [73]. However, the effective masses are only used to determine the strong-field excitation rate (according to the Keldysh expression, Eq. (2.13)). The conduction-band electrons that govern the optical properties of the excited dielectric have a range of kinetic energies, and most are not in the bottom of the conduction band, where the effective-mass description is appropriate. Therefore, the free-electron mass is used instead of the effective mass when calculating the optical properties of the excited dielectric in the Drude expression.

¹This valence-band density is based on an Al_2O_3 -density of $2.35 \times 10^{22} \text{ cm}^{-3}$ and the valence band being made up of the $\text{O}(2p^4)$ electrons [87].

4.3.1 Phase shift and absorption

As described in section 4.2, the experiment employs a pump-probe setup that allows for time-resolved measurements of the optical properties of the dielectric. The simulations give the electronic excitation and via the Drude description the optical properties (i.e. the refractive index) as functions of time, fluence (at the surface), and depth. Subsequently, a probe pulse is propagated through the excited dielectric. The change in the refractive index of the dielectric induces a phase shift and an absorption of the transmitted probe pulse along with a change in the probe reflectance. These are determined as functions of the pump-probe time delay and pump-pulse fluence. The relative angle between the propagation directions of the pump and probe pulses as well as the temporal duration of the pulses are taken into account.

Figure 4.4 is a schematic illustration of the interaction region as viewed from above. In practice, the phase shift ($\Delta\Phi$) and absorption (A) are found by integrating the real and imaginary part, respectively, of the change in the refractive index along the probe propagation direction (axis l in figure 4.4). For a given z -coordinate, the corresponding l - and r -coordinates for the probe pulse position are

$$l = \frac{z}{\cos(\theta)} \quad (4.1)$$

$$r = z \tan(\theta), \quad (4.2)$$

where r is the radial coordinate – perpendicular to z , and θ is the angle between the pump and probe beam propagation paths inside the dielectric (10°).

Stable-level simulations

To simulate the phase shift and absorption measurements, the change in the refractive index ($\Delta\tilde{k} = \tilde{k} - k_0$) is needed. At the latest times in the simulations, the excitation has reached a steady state. This level can be compared to experiments, where the measured quantities have also reached stable levels. For $t = t_{\text{final}}$, the simulations give $\Delta\tilde{k}$ as a function of pump-peak fluence and depth. The surface

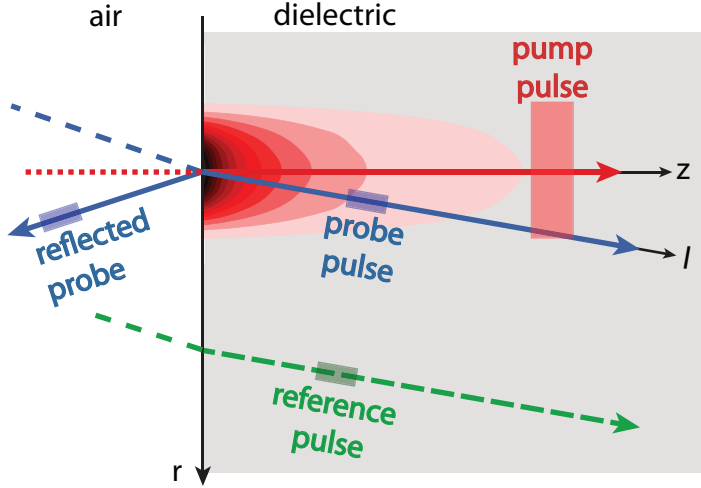


Figure 4.4: A schematic drawing (top view) of the interaction region. The spatial width of the pump pulse is illustrated, while the probe pulse is much wider (about the height of the figure). However, only the thin slices (probe and reference) that enter the slit in the spectrometer are shown; see section 4.2 for details. The red shaded region behind the pump pulse illustrates the electronically-excited dielectric.

fluence is described by a spatial Gaussian distribution as in Eq. (1.2): $F(r) = F_{\text{peak}} \exp(-2r^2/\omega_0^2)$. The total phase shift experienced by the probe pulse is given by

$$\Delta\Phi = \frac{2\pi}{\lambda_{\text{probe}}} \int_0^L \Delta k(F(r), z) dl, \quad (4.3)$$

where $L = Z/\cos(\theta)$ is the length of the sample along the l -axis, Z is the thickness of the sample. λ_{probe} is the probe wavelength, which in this case is the same as the pump wavelength (800 nm). $\Delta k = k - k_0$ is the change in the real part of the refractive index. The absorption is given by

$$A = 1 - \exp \left[-\frac{4\pi}{\lambda_{\text{probe}}} \int_0^L \Delta\kappa(F(r), z) dl \right], \quad (4.4)$$

where $\Delta\kappa = \kappa$ is the change in the imaginary part of the refractive index,

which is simply given by κ , since the refractive index of the unperturbed material is purely real. For these calculations, the propagation of the pump pulse is assumed to be one-dimensional (along z), and no electron diffusion is included. This means that the excitation at any point is stationary and only determined by the depth and surface fluence for that specific r .

Time-evolution simulations

When the pump and probe overlap in time, the simple calculation for the fixed $t = t_{\text{final}}$ cannot be used. In this case, the phase shift and absorption are given by equations similar to Eqs. (4.3)–(4.4)

$$\Delta\Phi(\tau_{\text{delay}}) = \frac{2\pi}{\lambda} \int_0^L \Delta k(F(r), z, t_{\text{probe}}) dl \quad (4.5)$$

$$A(\tau_{\text{delay}}) = 1 - \exp \left[-\frac{4\pi}{\lambda} \int_0^L \Delta\kappa(F(r), z, t_{\text{probe}}) dl \right], \quad (4.6)$$

where τ_{delay} is the pump-probe time delay. In the simulations, the zero time-delay is defined as the time when the central part of the pump and probe overlap at the surface. For the time-evolution simulations a “probe time” t_{probe} is introduced

$$t_{\text{probe}} = \tau_{\text{delay}} + (l - z)k_0/c. \quad (4.7)$$

This is a relative time, which accounts for the probe pulse moving slower in the z -direction than the pump, due to their relative angle.

First, calculations are made for point-like probe pulses, i.e., without any temporal duration. Afterwards, for all time delays, the calculations are averaged over the Gaussian time-profile of the probe. Figure 4.5 shows an example of a time-evolution simulation. The phase shift (red) and absorption (blue) are shown as functions of the pump-probe time delay, both for the point-like (dashed) and the temporally averaged (full) probe pulse. At time-delays around $\tau_{\text{delay}} = 0$, the simulations for the point-like probe are seen to vary rapidly, while the temporally averaged simulations are more smoothed. Note that the pump and probe pulses originate from the same original pulse and, thus, have the same pulse

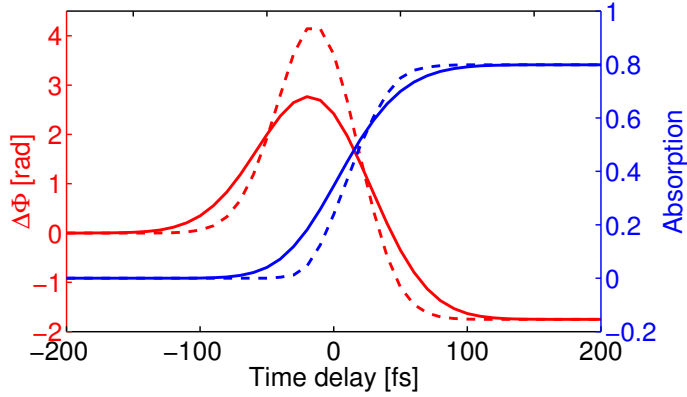


Figure 4.5: Simulated phase shift (red) and absorption (blue) as a function of pump-probe time delay for a pump-peak fluence of 1.83 J/cm^2 and a pulse duration of 70 fs. The dashed lines are for point-like probe pulses, and the solid lines are temporally averaged over the probe-pulse duration.

duration. In this example, the stable-value simulations would yield a phase shift of about -1.75 rad and an absorption of about 0.8.

4.3.2 Reflectance

When simulating the probe reflectance, Eq. (1.15) is not applicable, since the probe pulse is not normally incident on the sample surface. The probe pulse is polarized parallel to the plane of incidence (p -polarized), and the reflectance is given by [9]

$$R_{\text{probe}} = \left| \frac{\sqrt{1 - \frac{\sin^2 \theta}{k^2}} - \tilde{k} \cos \theta}{\sqrt{1 - \frac{\sin^2 \theta}{k^2}} + \tilde{k} \cos \theta} \right|^2. \quad (4.8)$$

The reflectance, like the phase shift and absorption, is temporally averaged over the Gaussian probe profile. Furthermore, the reflectance simulations have been spatially averaged over the central Gaussian fluence distribution of the pump pulse in the (25- μm diameter) region selected by an aperture; see section 4.2.

4.4 Results

When the time delay between the pump and probe pulses exceeds a few hundred femtoseconds, the measured phase shift, absorption, and reflectance stabilize at stable levels. These levels are governed by the final electronic excitation of the dielectric sample at the surface (reflectance) and throughout the bulk of the dielectric (phase shift and absorption). On the time scale of the experiment (~ 1 ps), no significant decay of these final levels are observed. The experimental data for the stable levels of these three quantities as well as the ablation depth are shown in figure 4.6 as functions of the laser peak fluence. As discussed in section 4.1, the evolution of the different quantities occurs in different fluence regimes (note the logarithmic fluence scale). The phase shift and absorption develop at low fluences (below ~ 4 J/cm²). When the absorption gets close to 1, the probe pulse is almost completely absorbed by the excited dielectric and, hence, the phase shift cannot be determined. On the other hand, the reflectance and hole depths develop at higher fluences (above ~ 5 J/cm²).

Due to the application of different compressor settings, a few different pulse durations have been applied in the experiments. In figure 4.6, the (blue) circular data points are taken with a pulse duration of 70 fs, the (green) triangular with 103 fs, and the (red) square with 120 fs. The low-fluence data are seen to be taken mainly at 70 and 103 fs, and the high-fluence data mainly at 120 fs. Hence, simulations are shown for pulse durations of 70 (cyan) and 103 fs (gray) for the phase shift and absorption, and for 120 fs (magenta) for the reflectance and hole depth. The simulations reproduce the experimental data well – even over the large span of fluences applied.

At the highest fluences, the simulations overestimate the reflectance. As described in section 2.6.1, in some cases, the simulations predict electron temperatures and velocities below those allowed by the Fermi-exclusion principle. Hence, simulations with lower limits set by the Fermi temperature and velocity, respectively, have also been made. The results of these simulations are shown as the dashed (black) line in the reflectance plot of figure 4.6. A noticeable difference is seen, where including the Fermi limit leads to a lower reflectance at the highest fluences, which agrees better with the experimental observations. Corresponding simulations have also been made for the three other quantities, which are not

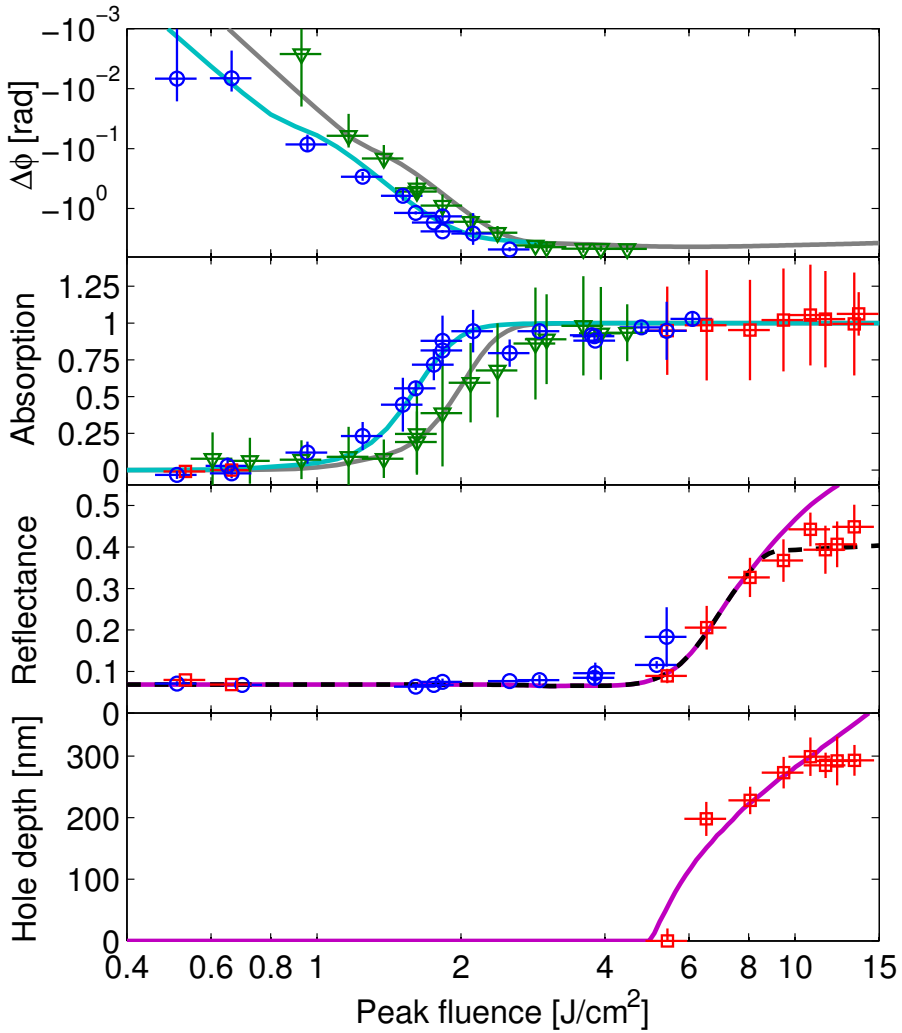


Figure 4.6: Phase shift ($\Delta\Phi$), absorption, reflectance, and ablation depth as functions of the peak fluence. The data points are the experimental data for pulse durations (FWHM) of 70 fs (blue circular), 103 fs (green triangular), and 120 fs (red square). The solid lines are simulations for pulse durations of 70 (cyan) and 103 fs (gray) in the upper two panels, and for 120 fs (magenta) in the lower two panels. The black dashed line is for a simulation that includes a Fermi-energy correction; see text for details.

shown, because they are not visibly different from the displayed curves.

As mentioned in section 4.3, the threshold criterion for ablation is an excitation density of 5.7 % of the initial valence-band density, which corresponds to an absolute conduction-band density of $1.6 \times 10^{22} \text{ cm}^{-3}$. This reproduces the experimental ablation-threshold fluence and the initial increase in ablation depth. However, the model seems to overestimate the ablation depth at the highest fluences. The same was observed in chapter 3 (Ref. [17]), and possible explanations for this disagreement are discussed in section 3.4.

For the phase shift and absorption, simulations for a spatially offset probe beam have been made. In figure 4.7, the phase shift and absorption data and simulations for the 70 fs pulse from figure 4.6 are shown again, and the dash-dotted (cyan) lines correspond to offsets of 5 μm on both sides of the pump-beam center. This represents an estimate of the uncertainty in the alignment of the experimental setup and, hence, the expected scatter of the individual data points. Looking at the schematic drawing of the interaction region in figure 4.4, the offset simulations can be understood as follows: If the selected part of the probe beam is too low (in figure 4.4), the interaction region is reduced and the most excited part of the dielectric is missed. Hence, the signals (i.e. the absorption and $|\Delta\Phi|$) are significantly reduced. On the other hand, if the selected part of the probe is too high, the interaction region is increased, and the signals increase. However, since the probe “goes behind” and misses the most excited part of the dielectric, the increase is not as pronounced as the decrease.

4.4.1 The rate of collisional excitation

The simulations presented above employ a relatively fast collisional excitation rate ($\alpha = 1 \text{ fs}^{-1}$). This means that within the present model, avalanche ionization will contribute quite significantly to the excitation process. This is in variance with another recent study by the group of Guizard, where Mouskeftaras *et al.* [84] investigate the excitation of quartz and sapphire in a double-pump experiment. The results indicate that avalanche excitation is negligible in short-pulse excitation of sapphire. Therefore, simulations have been made, where collisional excitation is reduced or completely removed. Instead, the simulations employ an enhanced strong-field excitation (i.e. by scaling up the Keldysh SFI-

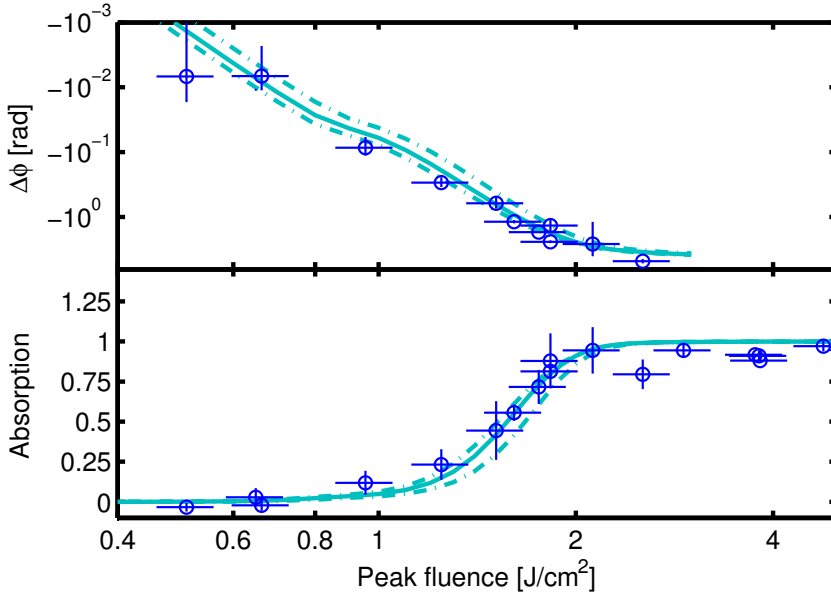


Figure 4.7: Phase shift and absorption measurements for the 70 fs data also shown in figure 4.6. The full line is the “on-axis” simulation where the selected part of the probe beam coincides with the central part of the pump beam at the surface; see figure 4.4. The dash-dotted lines are simulations, where the probe beam is offset by 5 μm to each side of the pump-beam center.

expression, Eq. (2.13)) in order to achieve excitation levels in agreement with the data.

Figure 4.8 shows alternative simulations of the phase shift, absorption, and reflectance; note the different fluence-axes. For the phase shift and absorption (upper two panels), only the 70 fs data are shown, and the solid cyan line is the simulation presented in figure 4.6 ($\alpha = 1 \text{ fs}^{-1}$). The blue lines are without collisional excitation ($\alpha = 0$), both with the SFI-rate not scaled (solid line) and scaled up by a factor of 10 (dash-dotted line). The green lines are for a much reduced collisional excitation rate ($\alpha = 0.01 \text{ fs}^{-1}$), with the SFI-rate unscaled (solid line) and scaled up by a factor of 3 (dash-dotted line). With a characteristic collisional excitation time of $1/\alpha = 100 \text{ fs}$, which is longer than the pulse duration, collisional

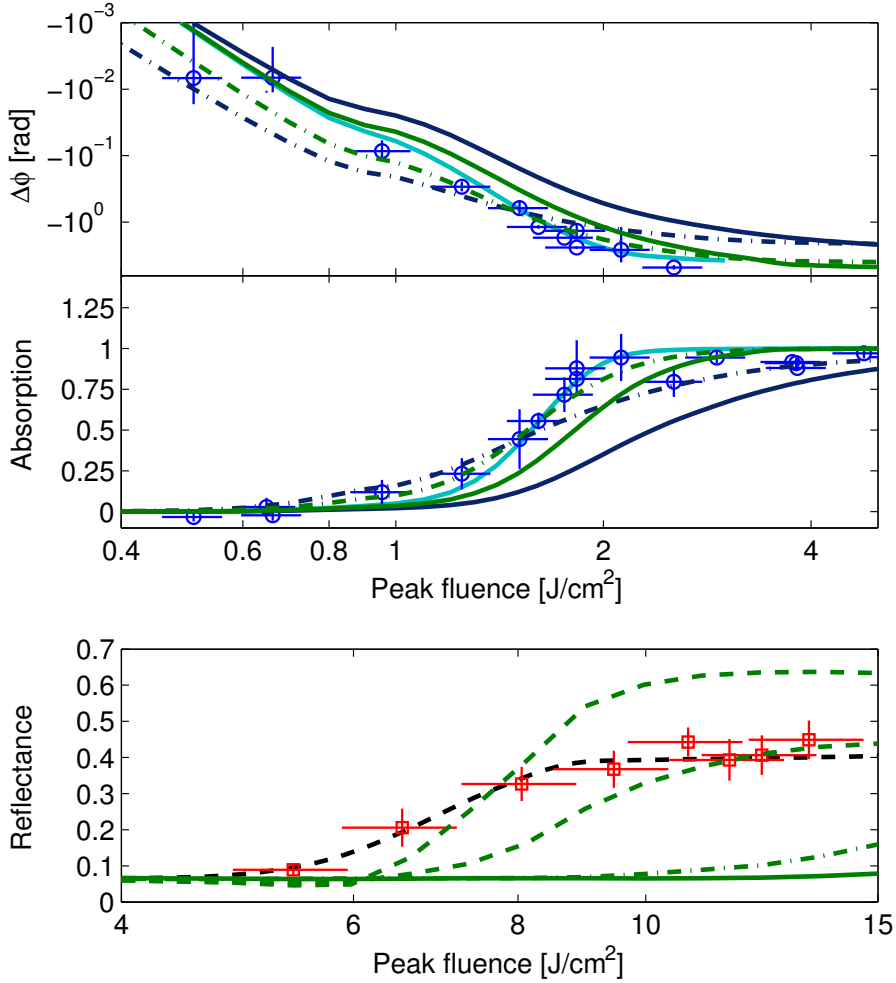


Figure 4.8: Simulations of the phase shift, absorption, and reflectance as functions of the peak fluence for different models with reduced and without collisional excitation. The data points are for the 70 fs (blue) and 120 fs data (red). The solid cyan lines in the upper two panels and the dashed black line in the lower panel are the same as shown in figure 4.6 ($\alpha = 1 \text{ fs}^{-1}$). The dark blue and green lines are without ($\alpha = 0$) and with reduced ($\alpha = 0.01 \text{ fs}^{-1}$) collisional excitation, respectively. The solid lines are without scaling of the SFI-rate and the dash-dotted with the SFI-rate scaled up by a factor of 10 (dark blue) and 3 (green). The dashed green lines in the lower panel is also with the SFI-rate scaled up by a factor of 3, and Γ_{e-e} scaled by 0.1 (top curve) and 0.3 (bottom curve); see text for details. Note the different fluence axes.

excitation will mainly occur after the pulse. Hence, the avalanche effect vanishes, but collisional excitation still contributes somewhat to the overall excitation. The unscaled phase shifts are close to the “original” simulation at low fluences, where the contribution from collisional excitation is small in any case. However, the slope of the phase shifts with reduced or no collisional excitation are too small to fit the data at high fluences. Scaling the SFI-rates increases the signal (increase in absolute value of $\Delta\Phi$), which gives better agreement at intermediate fluences, but the slopes remain too small. For the absorption, the trends are almost the same. The simulations without scaling of the SFI-rate give absorptions that are below the experimental data. In the case of no collisional excitation, a scaling of the SFI-rate is still not enough to reproduce the experimental data. For the reduced collisional excitation, the simulation with SFI-scaling is also different from the “original” simulation, but it actually reproduces the data equally well.

The lower panel in figure 4.8 shows different reflectance simulations for a 120 fs pulse duration. The black dashed line is the simulation presented in figure 4.6 ($\alpha = 1 \text{ fs}^{-1}$) including the Fermi-correction. Simulations without collisional excitation ($\alpha = 0$) produced constant reflectances over the entire fluence range (not shown). As above, the green lines are for the reduced collisional excitation ($\alpha = 0.01 \text{ fs}^{-1}$), with the SFI-rate unscaled (solid line) and scaled up by a factor of 3 (dash-dotted and dashed lines). Different scalings of the electron-electron scattering rate (Eq. (2.31)) has been applied to allow a fair comparison between simulations with the reduced and original collisional excitation rates. The dash-dotted line is with a scaling of 1.45 as used in the original simulations, and the dashed with scalings of 0.1 (top curve with highest reflectance) and 0.3 (bottom curve). Regardless of the adjustment of the Γ_{e-e} scaling, the simulations with the reduced collisional excitation does not reproduce the experimental results as well as the “original” simulations – both at high and low fluences. It should be noted that changing the Γ_{e-e} scaling has no observable effect on the low-fluence simulations.

4.4.2 Time-resolved measurements

The optimization of the simulations and choice of parameters were made to get the best agreement with the final-value data presented in figure 4.6. The simulations of the time-evolution data presented below were made

subsequently without any adjustment of the parameters.

Figure 4.9 shows two examples of the phase shift (red circles) and absorption (blue diamonds) measured as functions of the pump-probe time delay. The lines are the corresponding simulations. Panels (a) and (b) are for 103 and 70 fs pulses, respectively. The large positive phase shift around zero time delay is due to the Kerr effect as seen in figure 4.2 (b). For the 70 fs pulse, a small dip in the phase shift is observed before the Kerr spike and the experimental data are below the simulation in the first part of the spike. This is probably due to artifacts from beam steering caused by the spatial variations in the refractive index combined with the non-co-linear geometry. The effect is not observed in the data for the 103 fs pulse, presumably due to better alignment of the pump-probe overlap.

In both cases, the measured absorption is seen to increase during the pump-probe overlap and well before the simulated absorption increases. Most likely, this is caused by pump-assisted probe absorption: The presence of the strong pump pulse can cause single photons from the weak probe pulse to participate in, e.g., multi-photon absorption, where the rest of the required photons are supplied by the pump pulse. For the 70 fs pulse, there even seems to be a dip in the absorption before it increases again due to material excitation and stabilizes at the final level. This claim is further supported by the measurements at low pump fluence (e.g. for Kerr-only measurements as shown in figure 4.2), where no probe absorption is seen during the pump-probe overlap.

The above-mentioned effects make it difficult to interpret the data unambiguously during the pump-probe overlap and extract the material excitation. However, the experimental data seem to reach the stable level slightly slower than what is predicted by the simulations. This is especially pronounced for the 70 fs pulse, and may partly be explained by the opposite effect of what was observed before the Kerr peak (i.e. at negative delays). Still, the trend is also vaguely observed for the 103 fs pulse. This could be an indication of a relaxation process that is not accounted for in the model. A “smoothing” of the conduction band electron distribution away from the discretized distribution, as described by Kaiser *et al.* [24], may be a possible explanation.

The experimental data for the 70 fs pulse are obviously less scattered than for the 103 fs pulse, which also shows in the size of the error bars in figure 4.6. This is simply due to better statistics, i.e., each data point

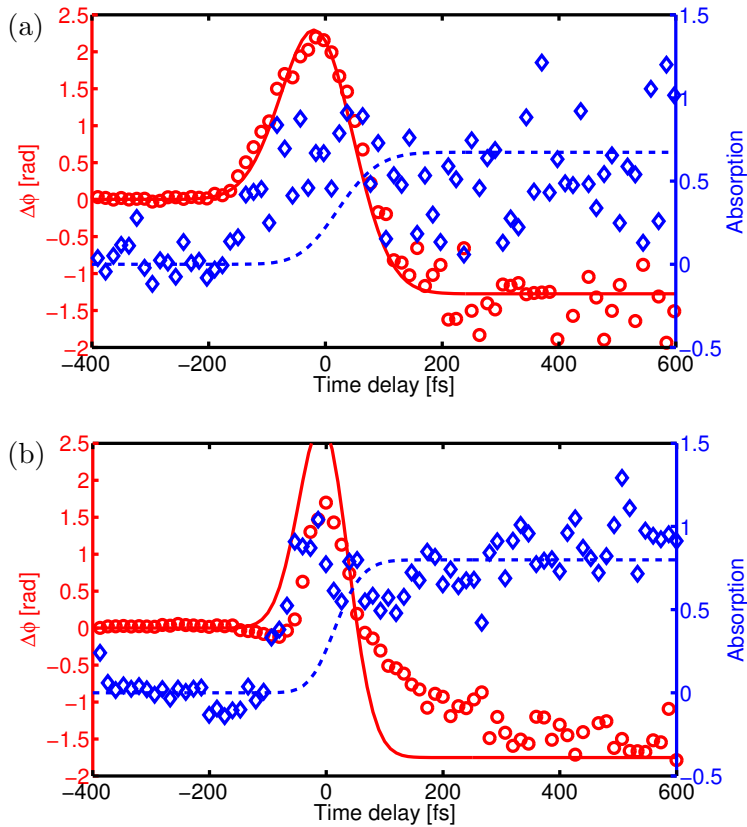


Figure 4.9: The phase shift and absorption as functions of pump-probe time delay. The data points are the experimental data for the phase shift (red circles) and absorption (blue diamonds). The solid (red) and dashed (blue) lines are the corresponding simulations. (a) is for a peak fluence of 2.1 J/cm^2 and a pulse duration of 103 fs, and (b) is for 1.83 J/cm^2 and 70 fs.

is averaged over more individual measurements.

Figure 4.10 shows an example of a reflectance measurement (data points) as a function of the pump-probe time delay. This data series is taken with a pulse duration of 70 fs, and the green line is the corresponding simulation. For comparison, the black line shows a simulation

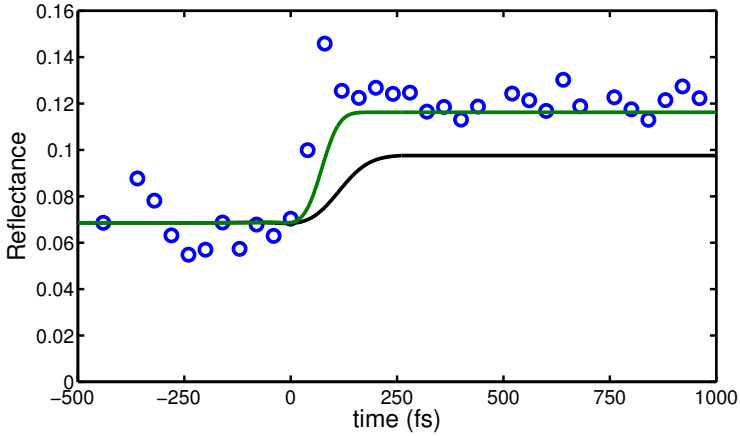


Figure 4.10: The reflectance as a function of time delay between pump and probe pulses. The points are the experimental data, and the green line is the corresponding simulation. The data and simulations are for a peak fluence of 5.14 J/cm^2 and pulse duration of 70 fs. For comparison the black line shows the simulation for a pulse duration of 120 fs.

with a pulse duration of 120 fs, as was used for most of the reflectance measurements and the simulations in figure 4.6. The experimental reflectance data show no sign of the delayed increase in signal that was seen in the phase-shift and absorption data relative to the simulations (figure 4.9). This could indicate that the (omitted) relaxation dynamics discussed above plays a larger role at lower excitation levels. It could be suggested that the slower relaxation observed in figure 4.9 is related to the rate of collisional excitation. However, since the effect is not observed in the reflectance data, this is not likely.

4.5 Discussion

The model described in chapter 2 is successfully applied to this comprehensive experiment that combines measurements of 4 different quantities over a large range of fluences. Minor refinements of the model have been introduced to get agreement with the experimental data at the lowest fluences, i.e., the spectral interferometry measurements. As the modifi-

cations (e.g. the introduction of the de Broglie wavelength) mainly affect the low-fluence simulations, they are not in contradiction with the previous simulations presented in chapter 3. However, the necessity of the modifications had not been discovered, was it not for the low-fluence experiments.

The good agreement between experiments and simulations could prompt one to believe that the simulations are very robust to changes in the different parameters. This is, however, not the case, and changes in one parameter cannot simply be counterbalanced by appropriate changes to another parameter. An example of this can be seen section 4.4.1, where the rate of collisional excitation is reduced, and no adjustment of the other parameters can successfully reproduce the experimental data. A different set of parameters can yield agreement for one of the measured quantities, but it is difficult to get agreement with all of them. The optimization of the parameters is like a complicated multi-dimensional treasure-hunt.

Ablation criterion

The two studies presented in this chapter and the previous provide ablation-depth measurements on sapphire using two different laser systems. In chapter 3, the criterion for ablation is to 13 % of the valence-band electrons being excited to the conduction band, whereas in this chapter 5.7 % is used. However, two different initial valence-band densities have been used in the simulations, which must be considered when comparing the two. The somewhat arbitrary density of 10^{23} cm^{-3} is employed in chapter 3, whereas the current model uses the more well-considered $2.8 \times 10^{23} \text{ cm}^{-3}$. The corresponding absolute threshold-density values are, thus, $1.3 \times 10^{22} \text{ cm}^{-3}$ (chapter 3) and $1.6 \times 10^{22} \text{ cm}^{-3}$ (this chapter). It should be noted that changing the initial valence-band density does not affect the ablation-depth simulations much, when employing the absolute-density criterion. The two absolute-density criteria obtained from the different studies agree quite well. However, the chapter 3 threshold is a bit lower than the other. As discussed in section 3.2.1, the sample used in chapter 3 probably contains color centers (a crystallographic defect). It is plausible that such defects give rise to a weakening of the crystal structure, making it less resistant to electronic excitation. Hence, this provides a possible explanation for the

differences in the attained threshold-densities for the two studies.

An ablation criterion based on the energy density in the material is tested to see how this compares to the electron-density criterion and the experimental data. The energy density ξ at any depth is calculated as the sum of the average kinetic energy and the band gap energy multiplied by the electron density: $\xi = (\frac{3}{2}k_B T_e + \epsilon_g) \times n_{\text{con}}$, where $k_B T_e$ is given by Eq. (2.33). An energy-density threshold of $\xi_{\text{threshold}} = 2.6 \times 10^{23} \text{ eV/cm}^3 = 42 \text{ kJ/cm}^3$ gives the best agreement with the experimental data. Comparing with the electron-density criterion above, this corresponds to the free electrons having gained an average of $\sim 16 \text{ eV}$ (including the band gap energy of 9.9 eV). The ablation-depth simulation with this energy-density criterion practically coincides with the electron-density simulation shown in figure 4.6. The $\sim 6 \text{ eV}$ kinetic energy at the end of the simulations is in accordance with what is observed in panel (c) of figures 2.4 and 2.5.

The energy-density criterion for ablation seems natural, if assuming that the electronic energy is eventually transferred to the lattice, thus, leading to ablation (e.g. simply due to evaporation), and in fact, the criterion is frequently used in the literature [26, 30, 33]. In a study by Brenk and Rethfeld [65], the two ablation criteria are found to yield similar results, which is also what we observe. The obtained energy-density threshold can be compared to theoretical values. An obvious comparison would be with the enthalpy of evaporation, but we have not been able to find any published values for this quantity for sapphire. However, an enthalpy of formation for sapphire has been found to be 1669.8 kJ/mol [88], which corresponds to 65 kJ/cm^3 , and Thompson [89] states the Gibbs free energy for sapphire at 298 K and 1 bar to be 378.08 kcal/mol , which corresponds to 62 kJ/cm^3 . These values are on the same order of magnitude as the determined energy-density threshold (42 kJ/cm^3). They are a bit higher, which seems reasonable as the material probably does not need to be completely disintegrated into the individual atoms for ablation to occur.

Interferometric studies and multi-photon absorption

In interferometric studies of material excitation, the low-intensity data are often used to determine the order of the multi-photon process that initiates the excitation [48, 54, 81, 84]. The reasoning for this is as follows:

At low fluences, the excitation is dominated by multi-photon excitation, because the pulse is not energetic enough to cause sufficient heating of the free electrons for collisional excitation to contribute significantly. Hence, the final excitation density is proportional to the fluence to the power of the multi-photon order ($n_{\text{con}} \propto F^N$). At low excitation densities, the change in the refractive index and, thus, the phase shift are directly proportional to the excitation density (this is derived in section 5.3.1). All in all, in this domain, the phase shift has a power dependence on the fluence. Therefore, a power-fit to the data can be used to determine the order of the process and, thus, give a rough estimate of the material band gap. If the optical response to a given excitation is known, e.g., from the Drude model, the fit can even be used to determine the multi-photon-absorption cross-section [81].

Examining the phase shift data obtained in this study (see, e.g., figure 4.7), it appears to be fairly linear in the log-log plot, i.e., exhibiting a power dependence. A power-fit to the data (not shown) gives a power-coefficient of 4.3 ± 0.4 . With the argument from above, this could easily be interpreted as evidence of a 4-photon absorption process. However, the literature states a band gap between 8.3 [74] and 9.9 eV [3, 76, 77] (the latter is used for the present simulations). With a laser excitation wavelength of 800 nm (corresponding to a photon energy of 1.55 eV), this means that the multi-photon excitation order is 6 or 7. As seen from the simulations presented in this chapter, the higher band gap (9.9 eV) is in fact compatible with the low slope of the data, when taking into account the appropriate excitation mechanisms as well as the light-field absorption. This goes to show that precautions must be taken, when estimating the multi-photon order from interferometric measurements. Even when the data appear linear in a log-log plot, there might be a slight curvature which is not visible over a limited fluence range.

4.6 Experiments on quartz

The results presented so far in this chapter are only for sapphire. However, during the experiments at CEA, similar measurements were conducted on quartz. Figure 4.11 shows a typical time-resolved measurement of the phase shift and absorption on quartz. As in figure 4.9, peaks are observed in both the phase shift and absorption during the pump-probe

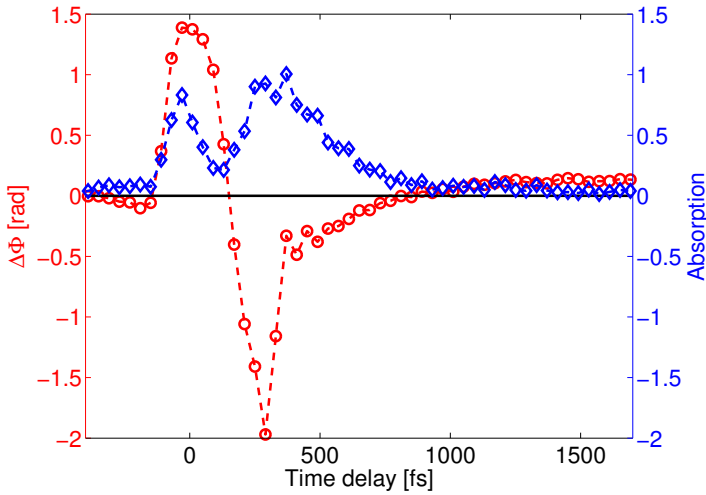


Figure 4.11: The phase shift (red circles) and absorption (blue diamonds) as functions of pump-probe time delay measured on a quartz sample. The dashed lines serve to guide the eye. The solid black line shows the zero-point. The peak fluence is 3.8 J/cm^2 and the pulse duration 120 fs.

overlap owing to the Kerr effect and pump-induced probe absorption. Subsequently, a large negative phase shift due to electronic excitation is seen together with an associated large absorption. However, very quickly (compared to the sapphire-experiments) the absolute values of the phase shift and absorption both decrease. Within about 1 ps, they reach stable levels, which for the phase shift is now *positive*. The fluence applied in this example is 3.8 J/cm^2 (with $\tau = 120 \text{ fs}$). In the case of sapphire, this would have led to a very large absorption and a phase shift that could not be extracted. However, for quartz the stable level values are actually quite low. Hence, spectral interferometry measurements at higher fluences are possible with quartz.

The stable value levels for the phase shift, absorption, and reflectance together with ablation depths are shown in figure 4.12 as functions of the peak fluence. Note that the fluence-axis starts at 2 J/cm^2 compared to 0.4 in figure 4.6. It is interesting to see that for quartz, the four measured quantities all evolve at the same fluence range. There are pros and cons to this: It does not enable comparison with simulations over

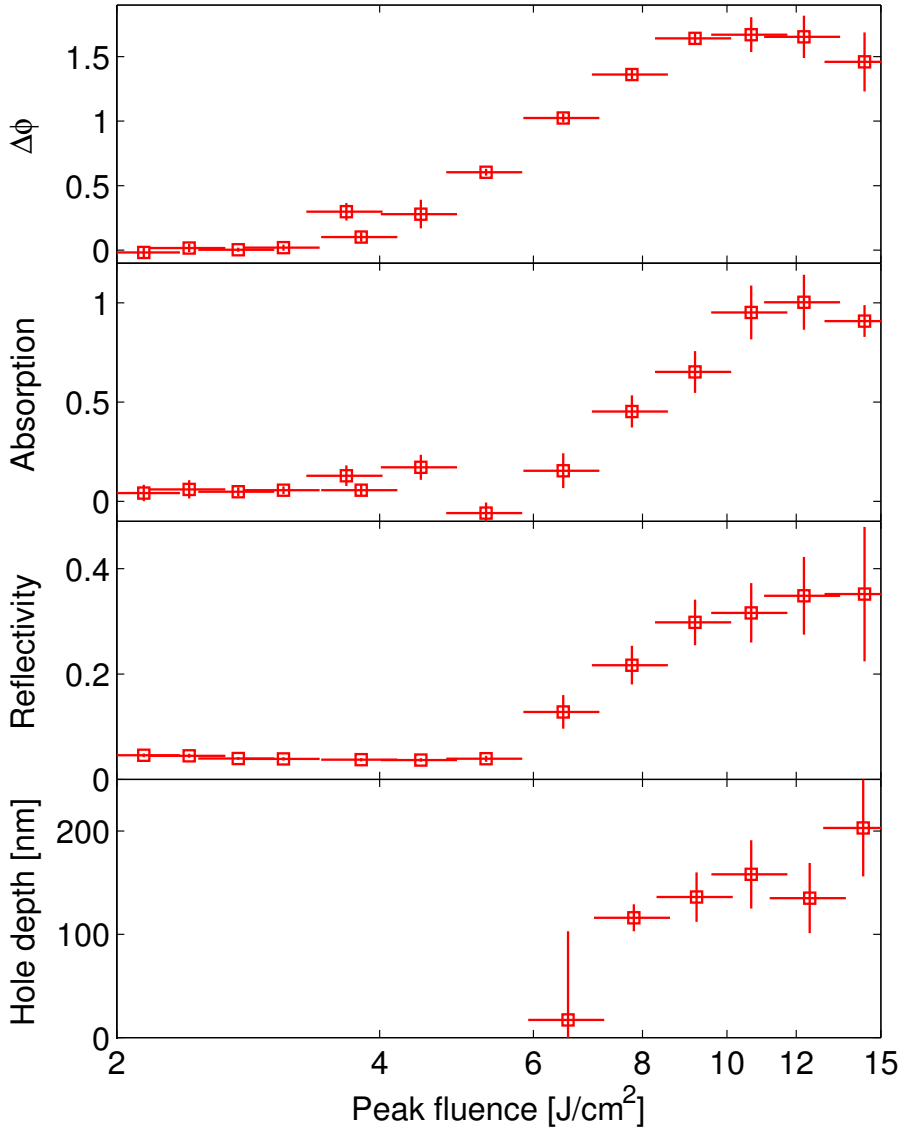


Figure 4.12: Phase shift ($\Delta\Phi$), absorption, reflectance, and ablation depth as functions of the peak fluence. The data are measured on quartz with a pulse duration of 120 fs. Note, the fluence axis starts at 2 J/cm² compared to 0.4 in figure 4.6.

the large range of fluences that was possible with sapphire. On the other hand, it enables the comparison of simulations with all the four measured quantities simultaneously (i.e. at one fluence).

The group of Guizard has studied short-pulse excitation of quartz extensively [20, 22, 54, 84]. The characteristic increase in phase shift and positive stable-level values are ascribed to the formation of self-trapped excitons (STEs) [22]. Simulations based on “our” model of the excitation of quartz is still a work in progress, which is why no simulations are presented in the plots. These simulations require a further modification of the model to account for the fast exciton-trapping, which is currently being implemented. This will introduce several new parameters, including a frequency and width related to the transition to the STE state, which must be included in the expression for the dielectric function. In addition, a characteristic trapping time for the STEs is needed; fortunately a good estimate for this can be deduced from the time-evolution measurements. Hopefully, the combination of the four different measured quantities will provide a solid basis for determining the various parameters.

A study by Hernandez-Rueda *et al.* [90] employs time-resolved reflectance measurements to investigate the plasma dynamics of highly excited quartz (and fused silica). An increase in reflectance is also observed in this study for a 120 fs pulse with a fluence of 7.5 J/cm^2 , and the maximum reflectance obtained is about 0.24, which is relatively consistent with our measurements (see figure 4.12 3rd panel from the top). However, in Ref. [90] there is a delay between the pump pulse and the increase in reflectance. For the first few hundred femtoseconds, there is no noticeable change in the reflectance and the maximum value is not reached until a delay of about 1.5 ps. In another study by the same group, Puerto *et al.* [91] present time-resolved measurements of both the reflectance and transmittance of fused silica, and a delay between the pump pulse and the drop in transmittance (increase in absorption) is also observed. The minimal transmittance occurs sooner than the maximal reflectance, but well after the pump pulse has ended. Note that this is for fused silica, however, from Ref. [90] the time-evolutions for quartz and fused silica appear similar. Such long delays between the pump-material interaction and optical response are not observed in our experiments, which apply both higher and lower fluences. The time-evolutions observed in figure 4.11 are typical for all the applied fluences, and the reflectance measurements (not shown) also start increasing dur-

ing the pump-probe overlap and show no sign of such large delays. For now, we have no good explanation for the observed discrepancies between the different experiments, but hopefully the simulations will help to clarify this.

Excitation of water by temporally shaped pulses

The model described in chapter 2 is originally developed for solid dielectric crystals, and the experiments described in the previous two chapters are performed on solid single-crystalline dielectric samples (mainly sapphire). However, the model can be applied to other materials with similar physical properties. Liquid water can in many ways be viewed as an amorphous dielectric. Spectral interferometry experiments of laser-excited water has been carried out in the group of Professor Thomas Baumert at the University of Kassel [48].

This chapter describes how our model has been applied to simulate these experimental results. The chapter starts with an introduction of how this work was motivated. The experimental details and results from the article of Sarpe *et al.* [48] are presented, since this is important to the simulations and how the resulting data are extracted. Various approaches to modeling the data are presented and discussed.

The work presented in this chapter is currently being written into an article entitled: *Excitation of water by temporally shaped femtosecond laser pulses: Measuring and modeling the transient optical properties including propagation*, in preparation (2013) [19].

5.1 introduction

Sarpe *et al.* [48] have studied the excitation of water by laser pulses with different temporal shapes using spectral interferometry. A single-rate-equation model was used to describe the relatively low-excitation data, and good agreement between numerical modeling and experiments was achieved. The original motivation of the work presented in this study was, therefore, mainly to explain and – hopefully – reproduce the high-excitation data from the experiments, as the low-excitation data were believed to be well-understood. However, when investigating the experiment with a more elaborate model, especially taking light-field absorption into account, the interpretation of the entire experiment turned out to be more complicated than initially anticipated.

In this chapter, simulations based on the model described in chapter 2 are applied to try to reproduce the experimental data from Ref. [48]. This work is still in progress, and the results presented here are preliminary. So far, focus has mainly been on describing the low-excitation data. However, possibly explanations for some surprising behavior observed at high excitation is presented in section 5.5, and ways to incorporate these in the model have already been tested.

5.2 Experiments

The experiments presented here are published in the article by Sarpe *et al.*: *Real-time observation of transient electron density in water irradiated with tailored femtosecond laser pulses*, New Journal of Physics **14**, 075021 (2012) [48]. The experimental results are reproduced with the accept of the authors.

5.2.1 Setup

The experiment utilizes a spectral-interferometry setup, and a schematic illustration of the setup is shown in Ref. [48]. The basic principles are the same as described in chapter 4. However, there are some differences between the two setups. The setup in Kassel has a co-linear geometry, where both the pump and probe beams are normally incident on the sample. This eliminates some of the special considerations due to the

Table 5.1: Experimental parameters for the pump and probe pulses. Pump-pulse duration is for the bandwidth-limited pulse.

	Pump	Probe
Pulse duration (fs, FWHM)	35	55
Spot size (μm , $1/e^2$)	30.5	120
Wavelength (nm)	785	392.5
n_0	1.329	1.34

off-axis geometry that had to be taken into account in chapter 4, which greatly eases the simulations.

The pump beam uses the fundamental frequency of the laser output (i.e. 785 nm). It is sent through a pulse shaper, which is based on a liquid-crystal modulator (Jenoptik SLM-S640d). A description of the pulse shaper is given in the article by Wollenhaupt *et al.* [92]. This enables very diverse shaping of the pump pulses in phase, frequency, intensity, and polarization. For these experiments, bandwidth-limited and third-order dispersion (TOD) shaped pulses are used; see section 5.2.2. The probe beam uses the second harmonic of the laser output (i.e. 392.5 nm). A birefringent α -BBO crystal splits the probe beam into a reference and a probe pulse with a separation of 6.5 ps. They are equally intense and their polarization is rotated by 45° to each side relative to the original probe pulse. After the sample, the temporal separation is decreased to 0.2 ps in another (thinner) BBO crystal, which is rotated by 90° relative to the first. With this clever setup, pump-probe delays of up to 6.5 ps can be achieved, while having a short probe-reference separation in the spectrometer giving a high fringe resolution at the CCD. A short-pass color filter is used to sort off the pump beam after the sample, so that only the probe and reference pulses enter the spectrometer. The sample is a $96 \mu\text{m}$ thick water jet with a speed of 3 m/s, which ensures a clean sample for every measurement. The rest of the experimental parameters for the pump and probe beams are listed in table 5.1. The pump pulse duration (FWHM) is for the bandwidth-limited pulse.

5.2.2 Pulse shapes

As mentioned above, three different pump-pulse shapes are used in the experiments. One is a bandwidth-limited pulse with a temporal Gaussian intensity distribution as given by Eq. (2.39) with a FWHM pulse duration of $\tau = 35$ fs. The other two are shaped pulses, where a third-order spectral phase function has been applied: $\phi(\omega) = \frac{\phi_3}{3!}(\omega - \omega_c)^3$ [48], where ω is the different frequency components of the pump pulse and ω_c its central frequency. The pulses are temporally antisymmetric with third-order dispersions of $\phi_3 = \pm 600\,000$ fs³; they will be referred to as the +TOD and -TOD pulses from hereon. The intensity envelopes of the TOD pulses are given by

$$I_{\pm\text{TOD}} = I_0 \left(f \frac{\tau}{\phi_0} \exp \left(0.5 \ln 2 \frac{\frac{2}{3}t_1 - t}{t_2} \right) \text{Ai} \left(\frac{t_1 - t}{\Delta t} \right) \right)^2, \quad (5.1)$$

where $f = \sqrt{\pi}/(2^{1/6}\sqrt{\ln 2})$, $t_1 = \tau^4/(32(\ln 2)^2\phi_3)$, $t_2 = 2(\ln 2)^2\phi_3/\tau^2$, $\phi_0 = |\phi_3|^{1/3}$, $\Delta t = \phi_0 \text{sign}(\phi_3)/2^{1/3}$, $\text{Ai}(x)$ is the airy-function of x , and $\text{sign}(\phi_3) = \phi_3/|\phi_3|$. I_0 is the peak intensity of the bandwidth-limited pulse before shaping.

The three different pulse shapes are shown in figure 5.1 for the same pulse energy. The bandwidth-limited pulse is scaled down by a factor of 5. The maximum intensity for the shaped pulses is about 6 times lower than for the bandwidth-limited pulse, and the largest peak of the TOD pulses is about 3 times wider than the bandwidth-limited pulse. The TOD pulses has many peaks that decrease (+TOD) or increase (-TOD) in intensity with time, and the entire duration of the pulses extends over several picoseconds. The antisymmetry of the TOD pulses enables investigation of the influence of collisional (avalanche) excitation. The excitation resulting from the SFI processes from the two pulses will be identical. If the largest intensity peak comes before all the smaller ones (as for the +TOD pulse), the first peak will create the initial free seed electrons that can then be heated by the subsequent smaller peaks and cause collisional excitation. Hence, if collisional excitation contributes significantly to the electronic excitation, notably larger signals are expected to be observed for the +TOD pulses than for the -TOD.

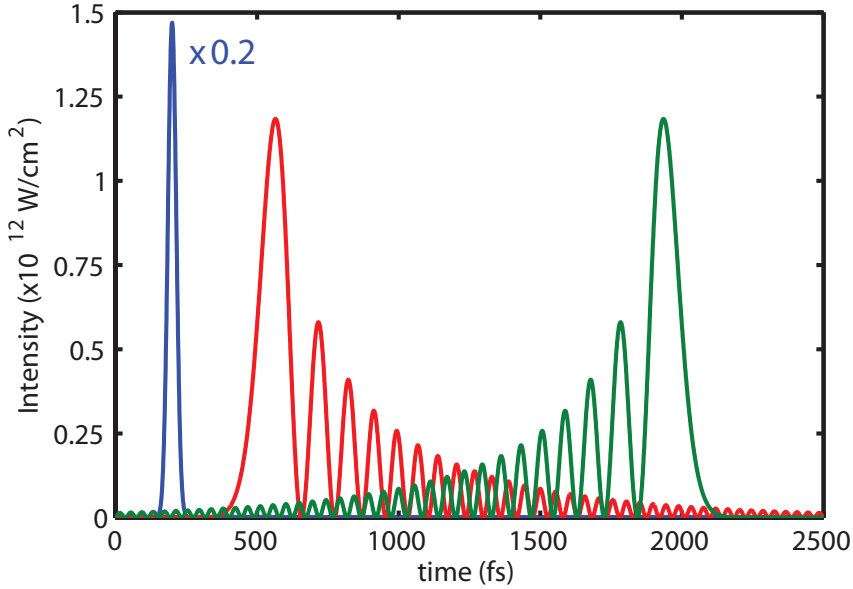


Figure 5.1: The intensity envelopes of the three different pulse shapes used in the experiments: bandwidth-limited (blue), +TOD (red), and -TOD (green). Note that the bandwidth-limited pulse is scaled down by a factor of 5. The pulse energy for all the pulses is $4 \mu\text{J}$ corresponding to a peak intensity of the bandwidth-limited pulse of $I_0 = 7.3 \times 10^{12} \text{ W/cm}^2$ with a pulse duration of $\tau = 35 \text{ fs}$. The third-order dispersions of the TOD pulses are $\phi_3 = \pm 600\,000 \text{ fs}^3$.

5.2.3 Experimental results

The fringe signal recorded with the CCD yields an intensity (S) as a function of (probe-laser) frequency (ω). This signal is fitted to the function [48]

$$S(\omega) = S_0(\omega) \left[1 + T + s\sqrt{T} \cos(\omega\tau_{\text{p-r}} - \Delta\Phi) \right], \quad (5.2)$$

where T is the transmittance and $\tau_{\text{p-r}}$ is the probe-reference time delay (0.2 ps). $S_0(\omega)$ is the signal envelope which is determined from measure-

ments without a pump pulse. From fits to the data, the phase shift ($\Delta\Phi$) and an effective optical density (OD) is extracted. The OD -signal is calculated from the transmittance as $OD = -\ln(T)$ and is used throughout this chapter instead of the absorption used in chapter 4.

The pump-probe setup with a variable delay can be used to determine the time evolution of the measured quantities. Examples of such time-evolution scans can be seen in Ref. [48]. The data from the temporal pump-probe overlap region cannot be interpreted unambiguously and will not be investigated further in this study. As mentioned above, a pump-probe time delay of 6.5 ps can be achieved with the experimental setup and the standard measuring technique. An alternative analysis method dubbed “relative mode” can be used at time delays larger than the 6.5 ps. In this case, both the reference and the probe pulses arrive after the pump pulse. However, any change in the material excitation during the 6.5 ps time delay between the pump and probe will still cause a phase shift and absorption. Recombination dynamics, for example, can be studied this way. As recombination leads to a decrease in the excitation, this will be observed as a positive phase shift in the relative mode, which is in fact observed in Ref. [48]. However, these signals are small, and during the initial 6.5 ps, the signals ($\Delta\Phi$ and OD) are almost constant. The focus of this study will only be on these stable level values and their dependence on pump-pulse energy and shape.

Figure 5.2 shows the experimentally measured phase shift and optical density as functions of the pump-pulse energy for the bandwidth-limited, +TOD, and -TOD pulses. The pump peak intensity for the bandwidth-limited pulse is stated on the top axis. These numbers differ by a factor of ~ 0.75 compared to those published in Ref. [48]. This is due to a calculation error in the published values, which has been corrected here. All the data sets show the same general trends: A relatively linear increase on the log-log scale for both $\Delta\Phi$ and OD at lower pulse energies. At higher energies, first the OD begins to decrease and then the $\Delta\Phi$, and at even higher energies the OD increases again. The linear regimes appear at different energies for the different pulse shapes. Due to the much (~ 6 times) higher peak intensity, the signals for the bandwidth-limited pulse appear at much lower energies. The +TOD-pulse signals are higher (i.e. at lower energies) than for the -TOD pulse, which is as expected with a significant contribution from collisional excitation.

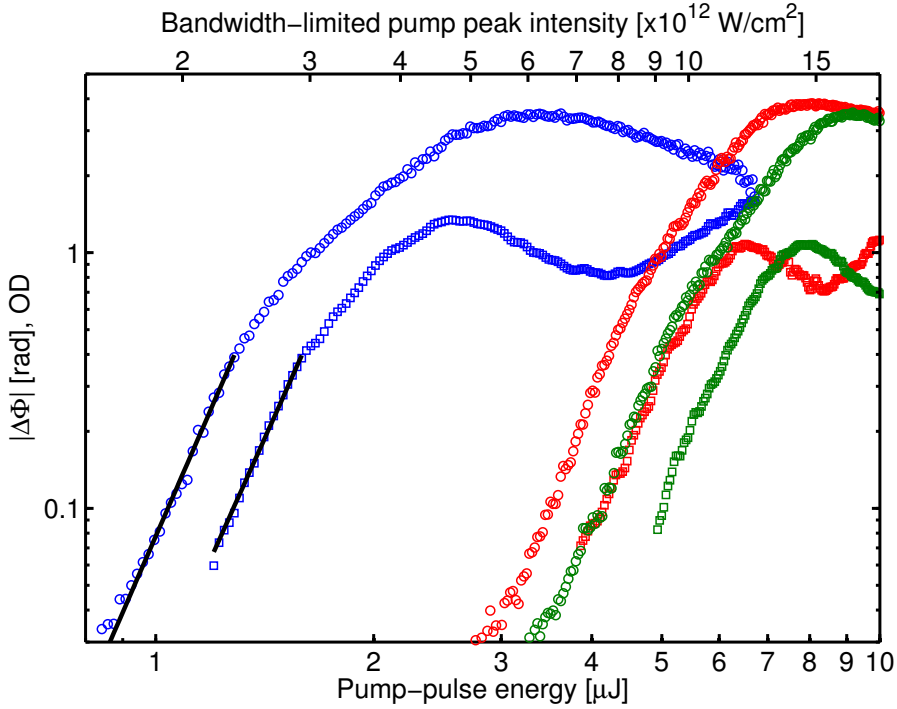


Figure 5.2: Absolute phase shift and effective optical density as functions of pump-pulse energy. The colors of the data sets represent the different pump-pulse shapes: bandwidth-limited (blue), +TOD (red), and -TOD (green). The circles are the $|\Delta\Phi|$ and the squares the OD data. The corresponding pump-peak intensity for the bandwidth-limited pulses are shown on the top axis. The solid black lines represent our power fits to the bandwidth-limited data in the regime where they are plotted; see text for details. The data are the same as those published in Ref. [48] and are reproduced with the accept of the authors.

5.3 Data analysis

In the low intensity regime, all the data sets in figure 5.2 seem to follow a power law, as they are relatively linear in the presented log-log plots. As described in section 4.5, such a power dependence is often interpreted as resulting from a multi-order process, where the order can be determined

from the slope. However, as also discussed in section 4.5, care should be taken when using this technique, as it may underestimate the order when looking at a narrow intensity range. Nevertheless, fits in Ref. [48] to the low-intensity part of the bandwidth-limited data yield exponents of 5.1 ± 0.2 for $|\Delta\Phi|$ and 5.2 ± 0.2 for OD , which is consistent with Sacchi [93] assuming an ionization energy of water of 6.5 eV corresponding to a 5-photon absorption process for 785-nm light.

We have also made fits to the low-intensity bandwidth-limited data, which are shown with the solid black lines in figure 5.2. They produce exponents of 6.5 ± 0.3 ($\Delta\Phi$) and 6.3 ± 0.2 (OD), thus, more likely suggesting a 6-photon process. Thomsen *et al.* [94] indicate that water has an absorption peak at about 150 nm (corresponding to 8.3 eV) and Elles *et al.* [95] state 8.2 eV, both of which are consistent with a 6-photon absorption process. The large differences in the exponents between the two fits goes to show that the specific choice of data region has a large influence on the obtained fitting values. When estimating a band gap for water, it is important to remember that it is in fact a liquid and, thus, not a classical dielectric arranged in a well-defined crystallographic lattice with an actual band structure. Absorption-spectroscopy experiments as performed by Elles *et al.* [96] also reveal that absorption at different photon energies are related to different physical mechanisms, e.g., dissociation at 8.3 eV and ionization at 12.4 eV.

The phase shift and optical densities are determined by the material excitation and can be calculated from equations similar to Eqs. (4.3) and (4.4). The co-linearly propagating pump and probe pulses simplifies the geometry, which results in phase shifts and optical densities given by

$$\Delta\Phi = \frac{2\pi}{\lambda_{\text{probe}}} \int_0^L \Delta k_{\text{probe}}(z) dz \quad (5.3)$$

$$OD = \frac{4\pi}{\lambda_{\text{probe}}} \int_0^L \Delta \kappa_{\text{probe}}(z) dz, \quad (5.4)$$

where L is now simply the sample thickness. Again, Δk_{probe} and $\Delta \kappa_{\text{probe}}$ are the changes in the real and imaginary parts of the refractive index. Note that this is for the probe pulse. In chapter 4, the pump and probe wavelengths were the same and, thus, also their refractive indices. Here,

the probe is the second harmonic of the pump, which means they have different refractive indices. The refractive index for the probe pulse is still given by Eq. (2.22) with the laser frequency set to the probe frequency $\omega_l = \omega_{\text{probe}}$.

5.3.1 Low-excitation regime

At low pump-pulse energies, the density of excited electrons remains relatively low and different approximations can be made. Since only a small fraction of the valence band electrons have been excited, the Clausius-Mossotti correction can be neglected, and the approximation $\varepsilon_b = k_0^2$ is appropriate (see Eq. (2.24)). With a low excitation density, the plasma frequency is also low as $\omega_{\text{pl}} \propto \sqrt{n_{\text{con}}}$. Note that the plasma frequency is purely a material parameter and *not* dependent on the laser frequency. For $\omega_{\text{pl}} \ll \omega_l$, \tilde{k} (Eq. (2.22)) can be approximated with a Taylor expansion to the first order:

$$\tilde{k}_{\text{probe}} \simeq k_{0,\text{probe}} - \frac{1}{2k_{0,\text{probe}}} \frac{\omega_{\text{pl}}^2}{\omega_{\text{probe}}^2 + i\omega_{\text{probe}}\Gamma}. \quad (5.5)$$

This expression can be split into its real and imaginary parts. By subtracting $k_{0,\text{probe}}$ and inserting the plasma frequency (Eq. (2.23)), the changes in the real and imaginary parts of the refractive index are given by

$$\begin{aligned} \Delta k_{\text{probe}} &\simeq - \frac{\omega_{\text{pl}}^2}{2k_0(\omega_{\text{probe}}^2 + \Gamma^2)} \\ &= - \frac{e^2 n_{\text{con}}}{2k_{0,\text{probe}} \varepsilon_0 m_{\text{con}} (\omega_{\text{probe}}^2 + \Gamma^2)} \end{aligned} \quad (5.6)$$

$$\begin{aligned} \Delta \kappa_{\text{probe}} &\simeq \frac{\omega_{\text{pl}}^2 \Gamma}{2k_{0,\text{probe}} (\omega_{\text{probe}}^2 + \Gamma^2) \omega_{\text{probe}}} \\ &= \frac{e^2 n_{\text{con}} \Gamma}{2k_{0,\text{probe}} \varepsilon_0 m_{\text{con}} (\omega_{\text{probe}}^2 + \Gamma^2) \omega_{\text{probe}}}. \end{aligned} \quad (5.7)$$

Figure 5.3 compares the full and approximate expressions for $|\Delta k_{\text{probe}}|$ and $\Delta \kappa_{\text{probe}}$ as functions of conduction-band density. The effective

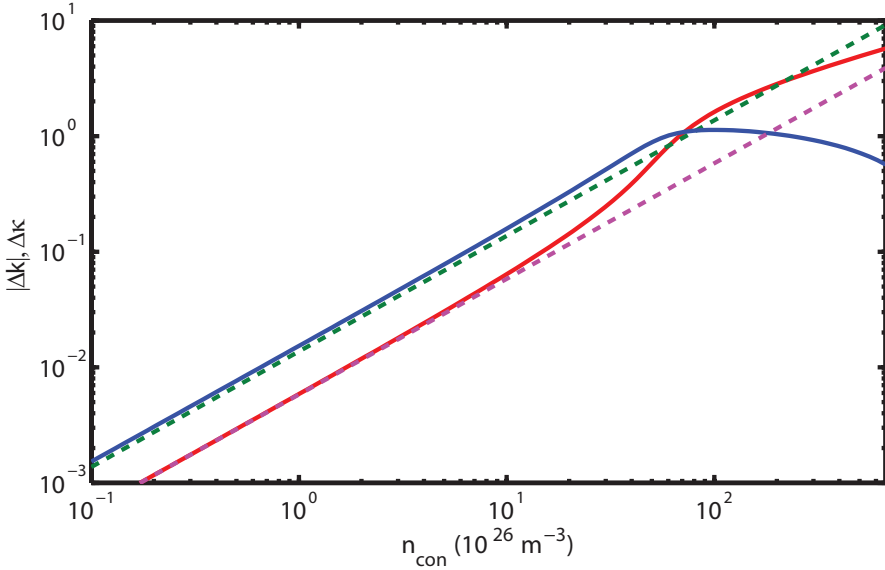


Figure 5.3: The calculated changes in the absolute value of the real part ($|\Delta k|$) and the imaginary part ($\Delta \kappa$) of the refractive index as functions of electron density in the conduction band. The solid lines are for the full expressions (blue: real part, red: imaginary part), and the dashed lines are for the approximate expressions given by Eqs. (5.6) and (5.7) (green: real part, magenta: imaginary). The calculations are based on the probe wavelength (392.5 nm), an effective electron mass equal to the free electron mass, an electron-scattering rate of $\Gamma = 10^{15} \text{ s}^{-1}$, and a total electron density of $n_{\text{tot}} = 6.68 \times 10^{28} \text{ m}^{-3}$.

electron mass is set equal to the free electron mass, and the electron-scattering rate is fixed at $\Gamma = 10^{15} \text{ s}^{-1}$. The approximate expressions depend linearly on density. The same goes for the full calculations in the low-excitation regime. However, at high excitation densities, they deviate from the linear behavior, and $|\Delta k|$ is seen to drop at the highest densities. The figure shows that with this set of parameters, the approximate expressions are applicable up to conduction-band densities of about 10^{27} m^{-3} . The small offsets at low excitation densities are due to the Clausius-Mossotti correction to the dielectric function, see

section 2.6.

With the approximations in Eqs. (5.6) and (5.7), the absolute value of the phase shift and the optical density can be expressed as

$$|\Delta\Phi| = \frac{\pi e^2}{\lambda_{\text{probe}} k_{0,\text{probe}} \varepsilon_0 m_{\text{con}} (\omega_{\text{probe}}^2 + \Gamma^2)} \int_0^L n_{\text{con}}(z) dz \quad (5.8)$$

$$OD = \frac{2\pi e^2}{\lambda_{\text{probe}} k_{0,\text{probe}} \varepsilon_0 m_{\text{con}} (\omega_{\text{probe}}^2 + \Gamma^2)} \frac{\Gamma}{\omega_{\text{probe}}} \int_0^L n_{\text{con}}(z) dz. \quad (5.9)$$

Here, a uniform scattering rate is assumed. If this approximation is not valid, it needs to be included in the integrals.

At very low excitation densities, where absorption of the *pump* pulse can be neglected, uniform excitation of the sample can be assumed. With no z -dependence the integral in the above expression can be approximated by $\int_0^L n_{\text{con}}(z) dz = Ln_{\text{con}}$. Hence, the uniform excitation density can be determined from $\Delta\Phi$ or OD via

$$\begin{aligned} n_{\text{con}} &= \frac{\lambda_{\text{probe}} k_{0,\text{probe}}}{L} \cdot \frac{\varepsilon_0 m_{\text{con}}}{\pi e^2} (\omega_{\text{probe}}^2 + \Gamma^2) \cdot |\Delta\Phi| \\ &= \frac{\lambda_{\text{probe}} k_{0,\text{probe}}}{L} \cdot \frac{\varepsilon_0 m_{\text{con}} \omega_{\text{probe}}}{\pi e^2 \Gamma} (\omega_{\text{probe}}^2 + \Gamma^2) \cdot OD. \end{aligned} \quad (5.10)$$

In order to determine the conduction-band electron density from this, the effective electron mass (m_{con}) is needed as well as the electron-scattering rate (Γ). The electron-scattering rate can be determined by dividing Eqs. (5.8) and (5.9)

$$\Gamma = \frac{\omega_{\text{probe}} OD}{2|\Delta\Phi|}. \quad (5.11)$$

Note that this does not require the harsh assumption of uniform excitation density – only $\omega_{\text{pl}} \ll \omega_l$ and of course uniform Γ . The scattering rate can thus be found by measuring $\Delta\Phi$ and OD for any given (not too high) excitation.

If the electron-scattering rate is significantly below the probe laser frequency, the estimate $(\omega_{\text{probe}}^2 + \Gamma^2) \simeq \omega_{\text{probe}}^2$ is reasonable. Hence, from

Eqs. (5.8) and (5.9), the phase shift is seen to be relatively unaffected by changes in Γ , whereas the optical density is (to the first order) linearly dependent on Γ . Therefore, if the order of the multi-photon process is determined from experimental data, it is better to use the phase shift than the optical-density data. The slope of the *OD*-data might be “distorted” by a systematic change in the scattering rate. Once again, it should be emphasized that precautions should be taken when utilizing this technique, as discussed in section 4.5. In the low-intensity regime of the experimental data, the $|\Delta\Phi|$ and *OD* signals move closer to each other in the logarithmic y-scale as the pump intensity increases. This is probably related to an increase in the electron-scattering rate. Note that this is only true at low excitation, where the change in the refractive index (both the real and imaginary part) is proportional to the excitation density. As can be seen from figure 5.3, the real and imaginary parts diverge from the linear dependence in very different ways as the excitation is increased. Hence, there is no longer a fixed relation between the two signals and the scattering rate.

5.3.2 Energy consideration

In Ref. [48], a standard single-rate-equation model is applied to describe the low-pump-energy data. This model assumes a low uniform excitation density, i.e., pump-pulse absorption is not included, which means that Eq. (5.10) can be applied. A constant electron-scattering rate is found by Eq. (5.11) to be $\Gamma = (1.6 \pm 0.3 \text{ fs})^{-1}$. A 6.5-eV (5-photon) band gap is applied, and the effective electron mass is set equal to the free electron mass. Good agreement with the experiments is achieved, which is why the initial idea of this study was to apply our model to describe mainly the experimental data in the high-pump-energy regime. However, simulations with our model and the parameters obtained in Ref. [48] did not reproduce even the low-energy data. The simulated phase shifts and optical densities are much below the experiments.

In fact, a straight-forward energy consideration shows that the densities given in Ref. [48] are unphysical. By comparing the energy contained in the pump pulse with the energy deposited in the sample, as calculated with Eq. (5.10) with $m_{\text{con}} = m_e$, it becomes apparent that the numbers do not add up. The integrated energy density (energy per area) in the center of the pump pulse is simply the peak fluence, which

Table 5.2: Comparison of density of pump-pulse energy and minimum absorbed energy, as calculated by Eqs. (1.4) and (5.12) with $\epsilon_g = 6.5$ eV, $m_{\text{con}} = m_e$, and $\Gamma = (1.6 \text{ fs})^{-1}$. Calculations for two different experimental data points are shown.

ϵ_{pulse}	$ \Delta\Phi $	F_{peak}	$\delta\epsilon_{\text{min}}$
1.4 μJ	0.5	0.096 J/cm ²	0.063 J/cm ²
3.3 μJ	3.4	0.23 J/cm ²	0.43 J/cm ²

is given by Eq. (1.4): $F_{\text{peak}} = 2\epsilon_{\text{pulse}}/(\pi\omega_0^2)$, where (again) ω_0 is the pump spot size at the sample – not to be confused with the various optical frequencies. The minimum energy per area that must have been absorbed by the sample is that needed for the excited electrons to overcome the band gap. Excluding any electron heating, the minimum energy per area $\delta\epsilon_{\text{min}}$ for a given $\Delta\Phi$ is therefore given by

$$\begin{aligned} \delta\epsilon_{\text{min}} &= \epsilon_g \int_0^L n_{\text{con}}(z) dz \\ &= \epsilon_g |\Delta\Phi| \frac{\lambda_{\text{probe}} k_{0,\text{probe}} \epsilon_0 m_{\text{con}} (\omega_{\text{probe}}^2 + \Gamma^2)}{\pi e^2} \end{aligned} \quad (5.12)$$

Table 5.2 compares these two values at two different experimental data points (from figure 5.2). In the calculation of the minimum absorbed energy density, a band gap of 6.5 eV has been applied. Also, this is the smallest band gap for water that we have found in the literature and, thus, gives the most conservative estimate of the energy density. The first data point is in the power-dependence regime, where absorption should be relatively small and, yet, the minimum energy density is almost as high as the peak fluence. This means that the majority of the pump-pulse energy must have been absorbed – even when not taking electron heating into account. For the second point, the energy density actually exceeds the peak fluence. Even though, in this regime, the phase shift is probably not linearly dependent on the conduction-band density (see figure 5.3), this is not physical. Especially, when taking into account that plasma absorption has been omitted, which is very prominent at such high excitation densities. These energy calculations reveal that the

optical response ($|\Delta\Phi|$ and OD) for a given excitation density must be larger than what is predicted here. Therefore, various approaches to modify the model accordingly are investigated.

5.4 Simulations

Simulations based on the model described in chapter 2 have been made to attempt to reproduce the experimental data. As can be seen from, e.g., the approximate expressions in Eqs. (5.8) and (5.9), the phase shift and optical density increase with decreasing effective conduction-band-electron mass (m_{con}). Hence, in order to increase the phase shift and absorption for a given conduction-band density, m_{con} is reduced compared to the first test, where $m_{\text{con}} = m_e$ is applied.

The simulations presented below employ the parameters given in table 5.1 as well as a band gap of 8.3 eV [94], third-order susceptibility of $\chi^{(3)} = 3.3 \times 10^{-22} \text{ m}^2/\text{V}^2$, initial valence band density of $1.32 \times 10^{23} \text{ cm}^{-3}$, and constant electron-scattering rate of $\Gamma = (1.6 \text{ fs})^{-1}$. The effective electron mass (m_{con}), hole mass (m_{val}), collisional-excitation rate (α), and scaling of the SFI rate (ζ) vary in the different simulations and will be stated explicitly.

Simulations are also made for a 6.5 eV band gap (not shown). However, irregardless of effective masses and scalings of the SFI rate, these are unsuccessful in reproducing the low-excitation slope. This is consistent with the exponent of ~ 6 obtained from our power fits to the low intensity part of the data (see figure 5.2).

5.4.1 Phase shift

It should be emphasized that the following simulations are preliminary. In many cases, better agreement with a specific data set can most likely be achieved by fine-tuning of the different parameters. Also, a limited number of fluences has been applied in each simulation. However, the purpose of the plots is to show a trend and illustrate the effect of varying the different parameters, which the presented simulations are adequate for. The plots in this section only include the data and simulations for the phase shift to prevent them from being too crowded. As discussed above, the optical density is generally fixed relative to the phase shift at low excitation (and for a constant scattering rate). Hence, it suffices

to look at the phase shift for now, and the optical-density simulations is discussed in section 5.4.2.

Figure 5.4 shows different simulations of the phase shift for the bandwidth-limited and TOD pulses. The experimental data are the same as shown in figure 5.2. In panel (a), collisional excitation is not included ($m_{\text{con}} = m_{\text{val}} = 0.125 \times m_e$, $\alpha = 0$, and $\zeta = 1000$). Without collisional excitation, the two TOD pulses produce almost the same excitation density, thus, yielding very similar simulations. It was believed that collisional excitation would not contribute significantly to the excitation for the bandwidth-limited and $-$ TOD pulses. This way the $+$ TOD data could simply be used to determine the collisional excitation rate. The bandwidth-limited simulations are not too far off at the lowest measured phase shifts, however, both of the TOD simulations greatly underestimate the phase shifts. Hence, collisional excitation must also contribute to the excitation for the $-$ TOD pulse. As shown in section 5.2.2, the main peak of the TOD pulses is about 3 times wider than for the bandwidth-limited pulse, which easily justifies why collisional excitation should play a larger role for the $-$ TOD pulse than for the bandwidth-limited one.

In panel (b), collisional excitation is included in simulations similar to those in panel (a), but with $\alpha = 10^{14} \text{ s}^{-1}$ ($m_{\text{con}} = m_{\text{val}} = 0.125 \times m_e$ and $\zeta = 1000$). Note that including collisional excitation actually affects the bandwidth-limited simulation. In fact, the simulation in panel (b) is optimized to best fit the bandwidth-limited data, and good agreement is observed – it even reproduces the high-pulse-energy dip. Once again, it should be emphasized that better agreement could be achieved with fine adjustment of the parameters. The $-$ TOD simulation also shows good agreement with the measurements though it continues to increase further than the experimental data. However, the $+$ TOD pulse simulation overestimates the phase shift substantially. In panel (c), the collisional excitation is reduced by a factor of 20 to $\alpha = 5 \times 10^{12} \text{ s}^{-1}$ ($m_{\text{con}} = m_{\text{val}} = 0.125 \times m_e$ and $\zeta = 1000$). This makes the $+$ TOD simulation fit the data, but now the $-$ TOD simulation is too low. For both these values of α , the simulations predict differences between signals for the $+$ TOD and $-$ TOD that are too large compared to the experimental data. In order to reduce this difference, the effective electron mass is increased. Panel (d) shows an example of such a simulation ($m_{\text{con}} = m_{\text{val}} = 0.25 \times m_e$, $\alpha = 10^{15} \text{ s}^{-1}$, and $\zeta = 3000$). This has the

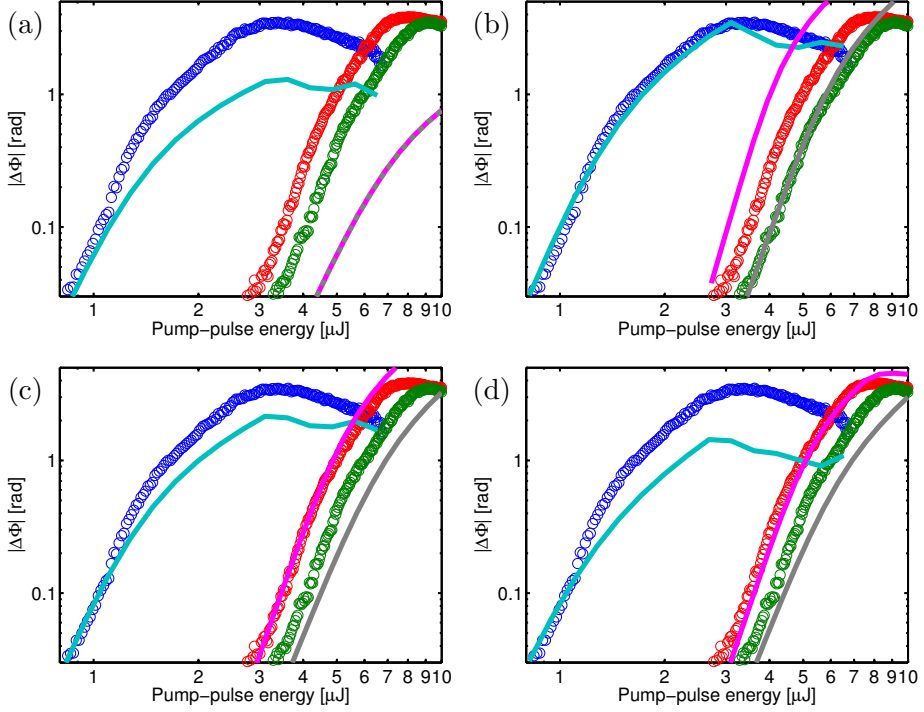


Figure 5.4: The phase shift as a function of the pump-pulse energy; the experimental data are the same as shown in figure 5.2: bandwidth-limited (blue), +TOD (red), and -TOD (green). The solid lines are simulations for the bandwidth-limited (cyan), +TOD (magenta), and -TOD pulses (gray). In panel (a), the gray line is dashed to be able to see the magenta line underneath. All the simulations employ a band gap of 8.3 eV, third-order susceptibility of $\chi^{(3)} = 3.3 \times 10^{-22} \text{ m}^2/\text{V}^2$, initial valence band density of $1.32 \times 10^{23} \text{ cm}^{-3}$, and constant electron-scattering rate of $\Gamma = (1.6 \text{ fs})^{-1}$.

- (a) $m_{\text{con}} = m_{\text{val}} = 0.125 \times m_e$, $\alpha = 0$, and $\zeta = 1000$.
- (b) $m_{\text{con}} = m_{\text{val}} = 0.125 \times m_e$, $\alpha = 10^{14} \text{ s}^{-1}$, and $\zeta = 1000$.
- (c) $m_{\text{con}} = m_{\text{val}} = 0.125 \times m_e$, $\alpha = 5 \times 10^{12} \text{ s}^{-1}$, and $\zeta = 1000$.
- (d) $m_{\text{con}} = m_{\text{val}} = 0.25 \times m_e$, $\alpha = 10^{15} \text{ s}^{-1}$, and $\zeta = 3000$.

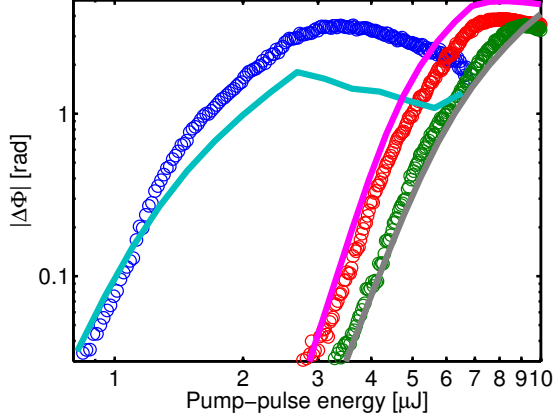


Figure 5.5: The phase shift as a function of the pump-pulse energy; the experimental data are the same as shown in figure 5.2: bandwidth-limited (blue), +TOD (red), and -TOD (green). The solid lines are simulations for the bandwidth-limited (cyan), +TOD (magenta), and -TOD pulses (gray). The simulations employ: $\epsilon_g = 8.3$ eV, $\chi^{(3)} = 3.3 \times 10^{-22}$ m²/V², $n_{\text{tot}} = 1.32 \times 10^{23}$ cm⁻³, $\Gamma = (1.6 \text{ fs})^{-1}$, $m_{\text{con}} = 0.25 \times m_e$, $m_{\text{val}} = 2 \times m_e$, $\alpha = 10^{15}$ s⁻¹, and $\zeta = 3000$.

desired effect, however, with the increased effective electron mass, the TOD signals cannot become high enough to reproduce the experimental data, when the other parameters are fixed to achieve agreement for the bandwidth-limited pulse.

In all the simulations above, the electron and hole masses are kept the same, which implies that $\mu = m_{\text{con}}/m_{\text{val}} = 1$ in Eq. (2.21) and $\epsilon_{\text{imp}} = 3/2\epsilon_{\text{corr}}$. Adjusting m_{con} and m_{val} individually, alters the role of collisional excitation (in a different way than by changing α), since it changes ϵ_{imp} and, thus, the number of photons an electron needs to absorb to cause collisional excitation. Figure 5.5 shows a simulation for $m_{\text{con}} = 0.25 \times m_e$, $m_{\text{val}} = 2 \times m_e$, $\alpha = 10^{15}$ s⁻¹, and $\zeta = 3000$, which is the best simultaneous agreement for all three pulse shapes that has been achieved so far and an improvement to the fixed electron-hole mass simulations shown above.

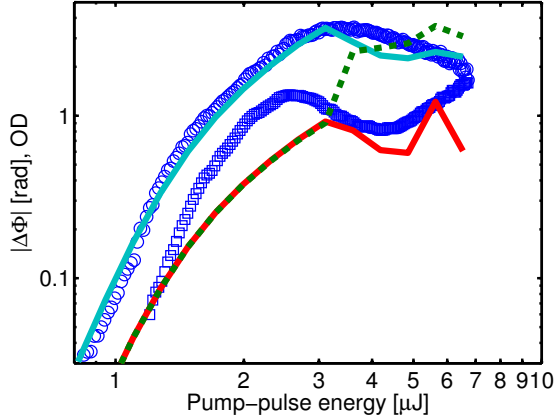


Figure 5.6: Phase shift (circles) and optical density (squares) as functions of the pump-pulse energy. The lines show simulations for the phase shift (solid cyan) as well as the uncorrected (solid red) and corrected (dashed green) optical density. The simulations employ the same parameters as in figure 5.4 (b).

5.4.2 Optical density

Figure 5.6 shows the experimental data and simulations for both the phase shift and the optical density for the bandwidth-limited pulse. The simulation parameters are the same as those applied in figure 5.4 (b). The OD simulations for the TOD-shaped pulses exhibit the same behavior as for the bandwidth-limited pulse and will not be examined specifically. The solid blue and red lines are the $\Delta\Phi$ and OD simulations as determined by Eqs. (5.3) and (5.4), respectively. However, as the material excitation increases, the surface reflectance and transmittance change (as seen in chapters 3 and 4). In a spectral-interferometry experiment, a reduced transmittance will appear as an increase in the OD -signal. The dashed green line is a corrected OD -simulation where the simulated surface transmittance is taken into account. As can be seen, at high excitation this leads to an increased optical density compared to the uncorrected simulation.

At low excitation, the optical density simulations are fixed relative to the phase shift owing to the fixed electron-scattering rate. The experimental data indicate a decreasing $\Delta\Phi/OD$ ratio for increasing excitation

density, where, if anything, the simulations predict the opposite. This suggests that Γ is in fact increasing with increasing excitation, which is not included in these simulations. Simulations with temperature-dependent scattering rates have been made (not shown), which gave an increased OD , but not as much as observed for the experimental data and only at higher excitation levels. At higher pump-pulse energies, a dip is observed in the optical density data, which starts at lower pulse energies than the dip in phase shift. The uncorrected OD simulation does show a dip, but simultaneously with the dip in the phase shift. Also, the corrected simulation shows no dip, which could indicate that the excitation at the surface behaves differently than in the bulk. Section 5.5 discusses the evolution of the high-energy data further.

5.5 Discussion and outlook

The simulations presented in this chapter demonstrate the necessity of relatively detailed models to describe the excitation of water in the examined pulse-energy range. Models that, e.g., omit light-field absorption are simply inadequate. However, the investigation to find an appropriate model to describe the excitation over the entire energy range is still under way. Long collisional-excitation times (i.e. a high α) as used in figure 5.4 (c) are not plausible, as this should be observed in the high-energy time-evolution scans for the bandwidth-limited pulses: The conduction band electrons would be left highly excited and then collisionally excite more electrons after the pulse was over. This would increase the excitation density and decrease the scattering rate (on a $1/\alpha$ time scale) – both of which increase the phase shift, which is not observed in the experiments.

The effective electron and hole masses are varied in the simulation, which in fact changes the reduced mass m^* and, thus, the SFI rate (see Eq. (2.13)). However, in the presented simulations, the SFI rate is calculated with $m_{\text{con}} = m_{\text{val}} = m_e$ and then scaled by the given ζ -values. Using the stated effective masses for the SFI-rate calculation instead will mainly cause a scaling of the rate, which means a different ζ would be applied. Especially at low intensities, where the SFI rate can be approximated by the multi-photon expression in Eq. (2.16). In fact, at low excitation, $\dot{n}_{MPI} \propto (m^*)^{3/2-\mathcal{N}}$, which means reducing m^* by a factor of 4 or 8 actually increases \dot{n}_{MPI} by a factor of 512 or 11585, respectively

(for $\mathcal{N} = 6$). These numbers are on the same order of magnitude as the applied ζ -values and, thus, may eliminate the need for scaling the SFI rate.

Lorentz model for refractive index

In order to increase the $\Delta\Phi$ and OD signals, the effective electron mass is changed in the presented simulations. In a different attempt to achieve this, a so-called Lorentz model has been employed to describe the dielectric function instead of the Drude model (Eq. (2.22)). This is motivated by experiments on solvated electrons, which indicate a strong and broad resonant absorption peak [94, 97, 98]. In the Lorentz model, the refractive index is given by [9]

$$\tilde{k}_{\text{Lor}} = \sqrt{\varepsilon_b - \frac{\omega_{\text{pl}}^2 f_{\text{Lor}}}{(\omega_l^2 - \omega_{\text{Lor}}^2) + i\omega_l \Gamma_{\text{Lor}}}}, \quad (5.13)$$

where ω_{Lor} is the central frequency of the Lorentz absorption peak and Γ_{Lor} is the electron-scattering rate for the electrons, which is equal to the width (FWHM) of the Lorentz absorption peak. f_{Lor} is the so-called oscillator strength, which is usually around 1 (why it has been omitted from Eq. (2.22)). Jou and Freeman [97] give the center and width of the absorption peak as functions of the water temperature. At room temperature, they are found to be $\omega_{\text{Lor}} = 2.62 \times 10^{15} \text{ s}^{-1}$ and $\Gamma_{\text{Lor}} = 1.28 \times 10^{15} \text{ s}^{-1}$, which corresponds to wavelengths of 720 and 352 nm, respectively.

Introducing the Lorentz refractive index increases the phase shift and optical density for a given conduction-band density. The oscillator strength is deduced from Thomsen *et al.* [94] and Jou and Freeman [97], which makes the probe-propagation simulations independent of the effective electron mass as this is included in the deduced oscillator strength.

However, the Lorentz-based simulations produced larger absolute values of the optical density than the phase shift, which is not compatible with the experimental findings. Perhaps some of the electrons in the conduction band (depending on their kinetic energy) follow the Lorentz description while others follow the Drude expressions. Simulations that adopt such a scheme with resonant transitions between some of the different discretized levels in the MRE model is being tested, but so far

they have not produced better results than the pure Drude simulations. However, this possibility will be investigated further in the future.

High pump-pulse-energy results

As mentioned above, the simulations deviate from the experimental data for high pump-pulse energies. Also, the behavior of the experimental data in this regime is not intuitively understood: The optical density starts to decrease prior to the decrease in the phase shift – for all three pulse shapes (see figure 5.2). Figure 5.3 shows that the $\Delta\kappa$ is continuously increasing for increasing excitation density. Hence, a decrease in the optical density is only obtained with a decrease in the total excitation (e.g. due to increased plasma absorption near the surface), but this also leads to a decrease in the phase shift – as predicted by the simulations, which is in disagreement with the data. For electron-scattering rates larger than the optical (probe) frequency, an increase in the scattering rate also causes a decrease in the optical density. However, this again also leads to decrease in the phase shift.

The introduction of the Lorentz model is in fact also partly motivated by this surprising behavior. The idea was that, at low excitation, the electrons follow the Lorentz description, but at higher pump-pulse energies the electrons are heated and follow a Drude description instead, which decreases the absorption (thus the OD) while the phase shift continues to increase. However, the simulations were unsuccessful in reproducing the desired behavior. Nevertheless, it is evident that for the high energies and excitation levels, a more elaborate model is required, which may include a temperature-dependent electron-scattering rate and perhaps a Lorentz-model for the refractive index. Effective masses and collisional excitation rates that depend on the electron kinetic energy may also be incorporated in a suitable manner.

Experimental outlook

Besides the above-mentioned future perspectives for the simulations, additional experiments may also serve to improve the understanding of laser-excited water. Measurements of the pump-pulse absorption tell how much energy is deposited throughout the sample, which gives a different measure of the excitation level, thus, easing the determination of

the optical response for a given excitation. Switching the pump and probe wavelengths could also provide new information: It increases the signals at low excitation, since $|\Delta\Phi| \propto \lambda_{\text{probe}}$ and $OD \propto \lambda_{\text{probe}}^2$ (in the Drude model). In the Lorentz model, a switch would actually lead to a probe frequency below the Lorentz peak causing *positive* phase shifts.

Unrelated to this water study, experiments on solid samples (e.g. sapphire and quartz) in the setup in Kassel would be of great interest. What will such experiments with shaped pulses indicate about the role of collisional excitation in sapphire compared to Ref. [84], and will the optical response in quartz be delayed as observed in Ref. [90]? Ablation studies by Englert *et al.* [99] on sapphire and fused quartz with the shaped pulses have already been carried out in the group of Baumert. They revealed surprisingly narrow holes with diameters well below the diffraction limit. It would be interesting to utilize the spectral-interferometry setup to study the material excitation further, which may give insight into the surprising ablation profiles.

Part II

Laser-written computer-generated holograms

Laser-written holography

Computer-generated holograms (CGHs) written with a femtosecond laser is an example of a direct application of laser-induced surface modifications, which exploits the ability of the femtosecond laser to generate small structures. For this project, the CGHs are written on the surface of silicon and copper samples, but the technique is very general and can be applied to any reflecting or transmitting material.

Two different studies have been done in connection with the laser-written CGHs. The first is a proof-of-principle study, which demonstrates that high resolution CGHs can be made – with the possibility of including 3-D effects. In the second study, different hologram parameters are systematically tested to optimize the hologram efficiency. Introductions to classical and computer-generated holography are given before the experimental procedures and results of the two studies are presented. Finally, the results from both studies are discussed.

The work presented in this chapter has led to the two articles *High-resolution computer-generated reflection holograms with three-dimensional effects written directly on a silicon surface by a femtosecond laser*, Optics Express **19**, 3434 (2011) [100] and *Optimizing the efficiency of femtosecond-laser-written holograms*, Applied Physics B, online first (DOI: 10.1007/s00340-013-5496-0) (2013) [101].

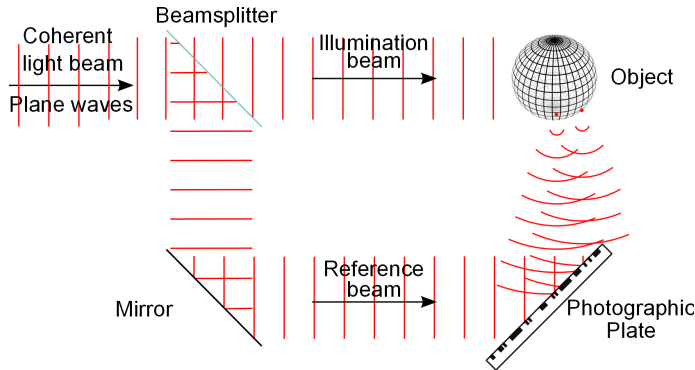


Figure 6.1: Recording of a classical hologram. The interference pattern of the object and reference beams is recorded on a photographic plate. The figure is taken from Ref. [104], courtesy of Thomas Rank Andersen.

6.1 Classical holography

This section gives a brief introduction to classical holography, and through that introduces some of the concepts used in the rest of this chapter. For a detailed description of classical holography, see, e.g., Refs. [102, 103]. In classical holography, the holograms are recorded using a special optical setup. A simplified schematic illustration of such a setup is shown in figure 6.1. A laser beam is split into two, and one beam is directed onto the object that wants reconstructed afterwards. The light is scattered off the object and some of the scattered light hits the holographic plate. This scattered light wave is known as the object wave. The second part of the laser beam (the reference wave) is sent directly to the holographic plate, where the interference pattern of the two incoming waves is recorded on a photographic film.

The photographic film is developed, which produces the actual hologram. The object wave is then reconstructed by illuminating the hologram with a so-called reconstruction beam, which is identical to the reference beam used in the recording. This is shown in figure 6.2. The reference beam is diffracted by the interference pattern of the hologram and thereby generates several waves traveling in different directions, one of which is identical to the original object wave. This is what is usually observed when looking at a hologram.

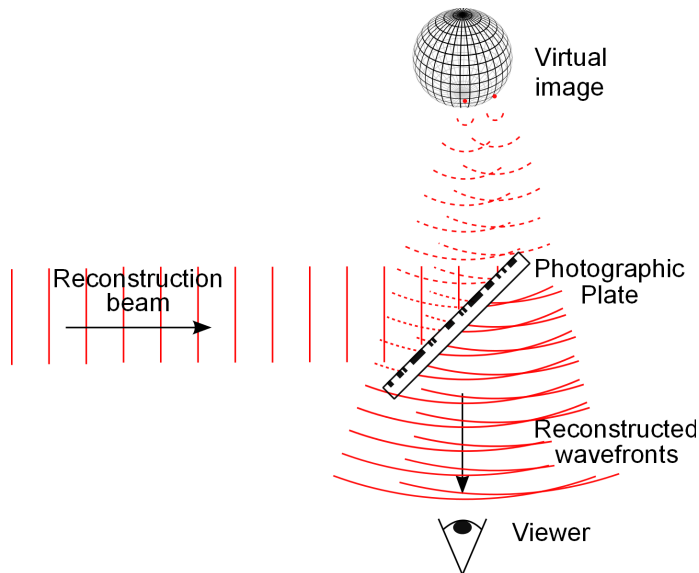


Figure 6.2: Reconstruction of a classical hologram. Illuminating the hologram with a reconstruction beam reproduces a wave that is identical to the original object wave and thereby generates a virtual image of the recorded object behind the hologram. The figure is taken from Ref. [104], courtesy of Thomas Rank Andersen.

When recording the hologram, highly coherent light is needed to obtain a nice interference pattern, which is why lasers are always used for this. In addition, the laser offers high intensity and a directional beam, which eases the recording process. Still, the setup has to be very static during the recording process. If one element is moved even a fraction of a wavelength (~ 100 nm) relative to another, this can change the interference and thereby the recorded intensity pattern significantly.

A good analogy to understand how a hologram appears, is to consider it as a window. An object behind a window is seen by looking through the window, and in the same way one has to look at the hologram to see the virtual object on the other side. To be able to see the three-dimensionality of the object, it must be observed from different angles. However, the object can only be seen from angles that are within the dimensions of the window or hologram. This, for one, implies that you

need a cylindrical hologram to have a 360-degree view of an object (in one rotational direction). On the other hand, if you have a very small hologram, the object can only be viewed from one angle and the three-dimensionality is unapparent. Holograms have the peculiar property that every part of the hologram reconstructs the entire object. So, if a hologram is split in two, each half can reconstruct the full object, and even very small holograms can reconstruct much larger objects. The holography experiments in this project exploits the latter.

6.2 Computer-generated holography

In computer-generated holography, the holographic interference pattern is calculated on a computer instead of being optically recorded with the complicated setup described above. This was first demonstrated in 1967 by Lohmann and Paris [105].

Calculation

There are different ways of calculating the CGHs; some are binary (e.g. “binary detour-phase holograms” [103, 106, 107]) and others are in gray scale (e.g. “kinoforms” [103, 108]). The CGHs for this project are calculated as binary Fresnel holograms [109]. Figure 6.3 shows the virtual setup that is used when calculating the holographic interference pattern. The object is thought of as consisting of a number of luminous voxels¹. Each object voxel, n , has a coordinate in space given by $(x_o(n), y_o(n), z_o(n))$, a real amplitude, A_n , and a relative phase, ϕ_n . The object is positioned at some distance from the hologram plane, which is at $z = 0$. The complex electric field of the object wave \mathbf{O} at a point (x, y) on the hologram is given by [110]

$$\mathbf{O}(x, y) = \sum_{n=1}^N \frac{A_n}{r_n(x, y)} \exp \left[i \left(\frac{2\pi}{\lambda} r_n(x, y) + \phi_n \right) \right], \quad (6.1)$$

where N is total number of voxels in the object, λ is the wavelength of the “recording” laser, and r_n is the distance between the object and

¹A voxel is the three-dimensional analogue of a pixel.

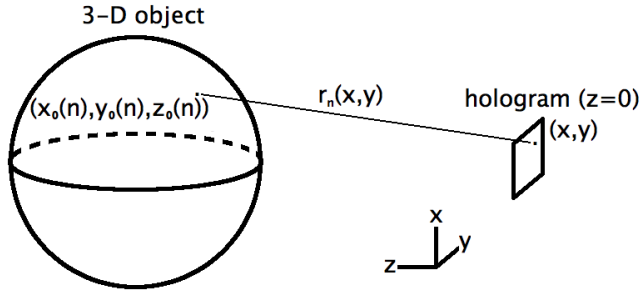


Figure 6.3: Calculation of a CGH from a three-dimensional object. The hologram is divided into pixels with coordinates (x, y) , and $r_n(x, y)$ is the distance from the n 'th object point to the pixel.

hologram points, which is given by

$$r_n(x, y) = \sqrt{(x - x_o(n))^2 + (y - y_o(n))^2 + z_o(n)^2}. \quad (6.2)$$

In these calculations, the reference beam is chosen to be normally incident and uniform on the hologram, so the reference electric field \mathbf{R} is constant: $\mathbf{R}(x, y) = A_{\text{ref}}$. Note that the time evolution of the electric fields, $\exp(i\omega t)$, is omitted because we are only interested in the intensity. This can be done because the time evolution of the two waves is the same, since they originate from the same (virtual) laser. The intensity of the total electric field on the hologram, which is the sum of the object and reference fields, is then given by:

$$\begin{aligned} I(x, y) &= \frac{1}{2} \epsilon_0 c^2 |\mathbf{O} + \mathbf{R}|^2 \\ &= \frac{1}{2} \epsilon_0 c^2 \left(|\mathbf{O}|^2 + |\mathbf{R}|^2 + 2\text{Re}(\mathbf{O}\mathbf{R}^*) \right), \end{aligned} \quad (6.3)$$

where \mathbf{R}^* is the complex conjugate of \mathbf{R} . The first and second terms are just the intensities of the object and reference waves, respectively. The third term, however, is due to interference and contains all the holographic information [111]. Looking only at this term and inserting

the values for \mathbf{O} and \mathbf{R} in Eq. (6.3) gives the so-called bipolar intensity

$$\begin{aligned}
 I_{\text{bp}}(x, y) &= \frac{1}{2} \epsilon_0 c^2 \cdot 2\text{Re}(\mathbf{O}\mathbf{R}^*) \\
 &= \epsilon_0 c^2 \text{Re} \left(A_{\text{ref}} \sum_{n=1}^N \frac{A_n}{r_n(x, y)} \exp \left[i \left(\frac{2\pi}{\lambda} r_n(x, y) + \phi_n \right) \right] \right) \\
 &= \epsilon_0 c^2 A_{\text{ref}} \sum_{n=1}^N \frac{A_n}{r_n(x, y)} \cos \left(\frac{2\pi}{\lambda} r_n(x, y) + \phi_n \right). \quad (6.4)
 \end{aligned}$$

The term ‘‘bipolar intensity’’ was introduced by Lucente [111] to account for the fact that this quantity can assume both positive and negative values. For the CGHs presented in this thesis, all the relative phases are chosen to be 0. Individual random phases can be assigned to each object point, which actually has some effect on the final outcome. A_n is chosen to be constant, which means that all the voxels in the object are equally bright. Since the hologram is very small compared to the distance to the object, the r_n outside the cosine can also be considered constant. The final CGH must be binary, so the common constant prefactor can be set to unity, which simplifies the expression for the final bipolar hologram intensity to

$$I_{\text{holo}}(x, y) = \sum_{n=1}^N \cos \left(\frac{2\pi}{\lambda} r_n(x, y) \right). \quad (6.5)$$

In the calculations, the hologram is divided into a two-dimensional (2-D) finite grid of equidistant pixels corresponding to the chosen pixel size and hologram dimensions, and the hologram intensity related to each pixel is calculated. A binary bit pattern is then constructed by setting all pixels in the grid with values below the median level to 0 and the rest to 1. When calculating the CGHs in this way, they automatically include focusing, which means that a real image of the object is generated at the same position relative to the hologram. This enables the realization of the holographic image without the use of other optics such as lenses. The object is given a small offset to prevent the holographic image from overlapping with the directly reflected beam.

Higher order holographic images are often observed in holographic reconstructions from CGHs, e.g., in all the holograms made for this the-

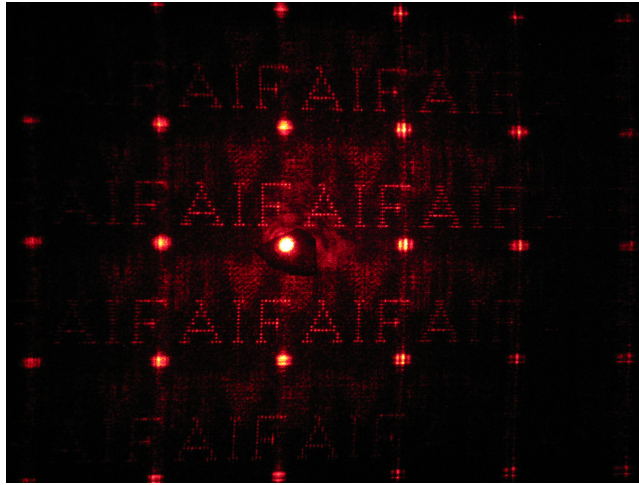


Figure 6.4: Image of a holographic reconstruction (IFA), where higher order images and diffraction spots are clearly visible.

sis. The pixels in the grid will – besides reconstructing the holographic image – function as a 2-D diffraction grating. At normal incidence, the angles, Θ_n , for constructive interference are given by [59]

$$\sin(\Theta_n) = \frac{n\lambda}{\Gamma}, \quad (6.6)$$

where λ is the laser wavelength and Γ the grating pitch, which in this case is the pixel size. If the pitch is smaller than the wavelength, only the 0th order (i.e., the directly reflected) spot exists. However, if the pixels are larger, higher order diffraction spots – as well as higher order holographic images – will appear. Figure 6.4 shows an example of a holographic reconstruction, where the higher order images and diffraction spots are clearly seen.

Fabrication

Once a CGH is calculated, there are different ways of fabricating the actual hologram from the calculations. A commonly used method is based on photolithography, which is well-known in the semiconductor

industry for manufacturing microchips. It is based on creating a mask, which is subsequently used to print the hologram (or microchip). It is a time-consuming process to make the initial mask and thereby the first hologram, but rapid mass production of identical holograms is easy once the mask is made. An example of this is the so-called embossed holograms that are for example found on *VISA* and other credit cards.

Recently, femtosecond lasers have been used for direct writing of CGHs, e.g., inside glasses [112–114], by evaporation of metal films on glass substrates [115], and in this project on silicon and copper surfaces [100,101]. The lithographic production method is suitable for mass production of identical holograms, while the direct-writing method provides a quick way to make “one of a kind” holograms. This opens up for new applications such as anti-counterfeiting, beam shaping [113,114], and optical keys [116].

For more insight on computer-generated holography, including other calculation techniques and more fabrication methods, see, e.g., Refs. [102, 103, 117].

6.3 Laser-written CGHs

The high resolution offered by ultrashort-pulse laser ablation is employed to write highly detailed holograms with a resolution up to 111 kpixels/mm² (~ 8500 dpi). These high-resolution holograms enable reconstruction of detailed images. In addition, it is demonstrated how three-dimensional effects can be realized in CGHs. Three-dimensional effects are visualized as a relative motion between different parts of the holographic reconstruction, when the hologram is moved relative to the reconstructing laser beam. This initial part is a “proof-of-principle” study, which merely demonstrates the capability of fabricating CGHs on a reflecting surface with a femtosecond laser. Optimization of various hologram parameters for the most efficient reconstruction is studied in section 6.4.

6.3.1 Experimental setup

The calculated CGHs are written directly onto a silicon surface using the femtosecond-laser system described in section 3.1.2. The beam is focused onto the sample surface using an aspheric lens with a focal length of 10

mm (NA 0.45). The sample is mounted on a 3-D translation stage, which is controlled by a computer that also controls whether the laser is on or off based on the position of the stage. This is done via an inhibit signal sent to the Pockels cell that switches the pulses in and out of the regenerative amplifier. The computer program LabVIEW is used for this simultaneous control. The different parameters that are specific to each hologram, such as the pitch, are set in LabVIEW, which then reads the calculated holographic bit pattern and writes it directly on the sample surface. A gentle flow of helium is applied through a nozzle enclosing the focusing beam to prevent break down in the air and remove laser-generated debris.

The CGHs generated with this technique are reflection holograms as opposed to the transmission holograms described in section 6.1 on classical holography, but the principles are the same, and reflection holograms work just as well as transmission holograms. For this study, silicon was selected because it is easy to obtain flat, uniform samples, and it is relatively inexpensive. The reflectance of silicon for wavelengths in the visible regime is about 35 % [118], which is not a lot compared to many metals but sufficient for the holography application.

The pulse energy is controlled with a half-wave plate inside the compressor (as described in section 3.1.2) together with a neutral density (ND) 2.0 filter, which has a transmittance of only 1 %. This is necessary to get the pulse energies down to the applied 50–100 nJ. The beam diameter before the lens is ~ 10 mm, so with a focal length of the lens of 10 mm, the theoretical Gaussian focal spot size (ω_0) is ~ 0.5 μm , hence the theoretical fluence is 6.5–13 J/cm².

The holograms are written by transferring the binary CGH bit pattern onto the sample by selective ablation of single pixels. The ablated areas have a significantly reduced reflectance, so when a laser beam is reflected off the hologram, the reflection will mainly come from the un-ablated areas. No pre- or post-treatment of the sample is necessary, so the CGHs are ready for use immediately after being written. The typical production time for a single hologram (700 \times 700 pixels) with this setup is about 10 hours. Therefore, it is only appropriate for this proof-of-principle study. Nevertheless, a subsequent upgrade of the experimental apparatus has decreased this time very significantly (see section 6.4.1).

The holographic objects are reconstructed by shining a laser onto the hologram and projecting the reflected light onto a screen. Both a He-Ne

laser at 633 nm and a frequency-doubled Nd:YAG at 532 nm have been used for the holographic reconstructions. The latter was used because of the high output power, which enabled clear and bright reconstructed images. The wavelength of the reconstruction laser does not have to be the same as the one used in the calculation of the CGH. If a different wavelength is used, the reconstructed image merely has a different size and focal distance.

6.3.2 Results

To demonstrate the capabilities of the direct-writing technique, two different virtual objects are used for the calculation of the CGHs. The seal of Aarhus University, which is a relatively detailed object, is used to investigate the effect of increasing the resolution of the CGHs on the clarity of the reconstruction. To study 3-D effects in the directly written CGHs, a 3-D object consisting of the letters “IFA” is used.

Resolution

With the employed setup, it has been possible to generate holograms with a pitch (i.e. the distance between pixels) down to 3 μm , which corresponds to a resolution of 111 kpixels/ mm^2 (~ 8500 dpi). Figure 6.5 shows scanning-electron-microscope (SEM) images of the silicon sample with the directly written CGH. Panel (a) shows a relatively large area of the hologram with the produced bit pattern. The size of the entire hologram is $2.1 \times 2.1 \text{ mm}^2$ (700×700 pixels). Panel (b) shows a magnified image of a few ablated spots. The spots have a diameter of 2.5–3 μm . This can be compared to the theoretical ablation diameter obtained from Eq. (1.16). Assuming a peak fluence of 6.5 J/cm^2 and a threshold fluence of 0.52 J/cm^2 [119], d should be only 1.1 μm . The reason for the larger spots is most likely aberrations in the lens in combination with deviation from a perfectly Gaussian beam profile, which also explains the slight ellipticity of the spots. However, as can be seen in figure 6.5 (b), the spots have a central ablated region with a diameter of about 1.4 μm , i.e., close to the theoretical ablation diameter. Most importantly, the reflectance is reduced significantly at all the ablated spots, which is the key feature for forming the binary hologram.

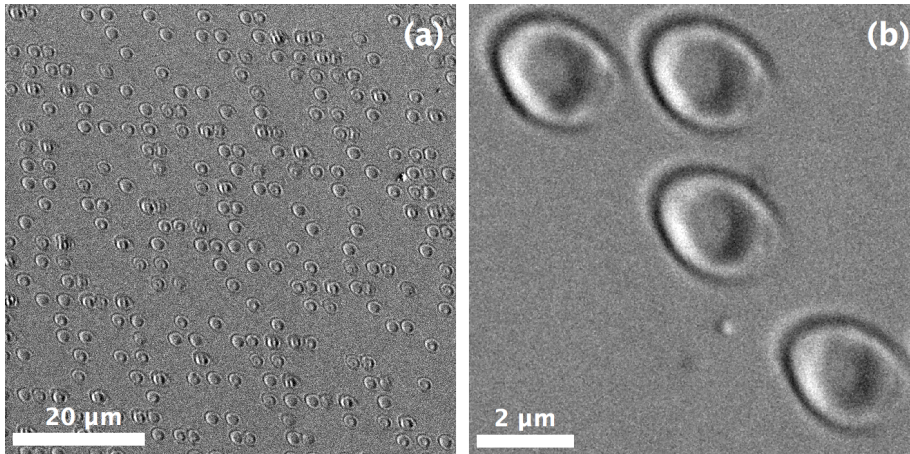


Figure 6.5: SEM images of the CGH pattern with a pitch of $3\ \mu\text{m}$ written on silicon. (a) Large part of the hologram showing the bit pattern. (b) Zoom in on a few ablated spots.

Figure 6.6 shows the seal of Aarhus University (a) and image of the reconstruction (b). The reconstruction is made with a frequency doubled Nd:YAG laser at $532\ \text{nm}$. As can be seen, this relatively detailed object can be reconstructed quite well. The distance between the hologram and the reconstruction screen is about $2\ \text{m}$, and the reconstructed logo has a diameter of about $20\ \text{cm}$, which means it is readily visible. The reconstruction distance and object size are set in the calculation of the CGH, but the depth of focus is very large, so the clarity of the reconstruction is not very dependent on the specific distance to the screen. This is explained in more detail below. A beam dump is placed between the hologram and the reconstruction screen to minimize scattered light from the reflection spot. Some of the scattered light can still be seen in the bottom right corner as well as the shadow of the beam dump (the dark spot in the very corner). The reason for the increasing blur in the reconstruction towards the left side of the object is discussed in section 6.5.

The achieved resolution is more than an order of magnitude higher than in previous similar work [115]. Increasing the resolution has several advantages, as it provides sharper images as well as enables reconstruc-

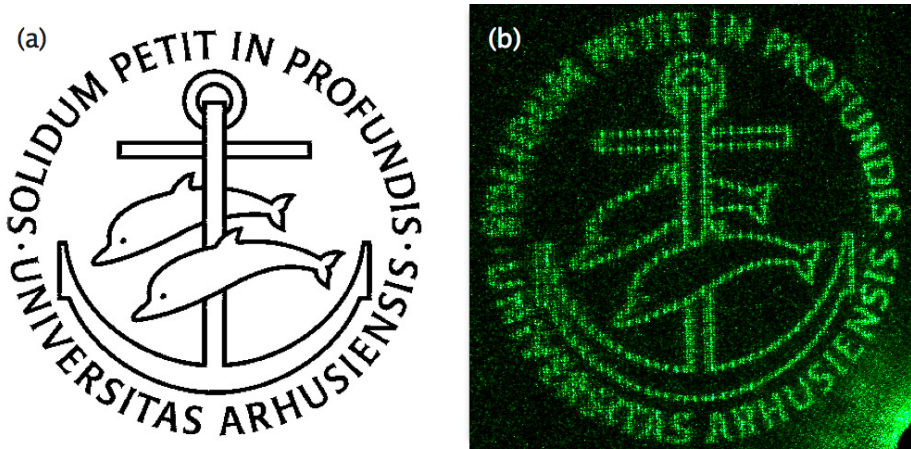


Figure 6.6: (a) The seal of Aarhus University. (b) Image of the holographic reconstruction made from a hologram with a pitch of $3\ \mu\text{m}$. The image is about 20 cm in diameter, and the bright area in the bottom right corner is scattered light from the reflection spot, most of which was blocked by a beam dump.

tion of larger objects. The images are sharper due to the increase in information in the hologram, which means that more detailed objects can be successfully reconstructed. Attempts to reconstruct the seal of Aarhus University, seen in figure 6.6 (a), with holograms of lower resolution were unsuccessful.

As described above, the hologram also acts as a two-dimensional grating, which explains why the reconstruction of larger objects is enabled by increasing the resolution. From the diffraction grating equation (Eq. (6.6)), the distance between diffraction spots is for small angles inversely proportional to the grating period, or in this case the hologram pitch. So, an increase in resolution (i.e. a decrease in pitch) increases the separation between diffraction orders. Since the holographic reconstructions are also generated at higher orders, this implies that larger holographic images can be created without overlapping when the resolution is increased.

Three-dimensional effects

Holography is well-known for the ability to reconstruct three-dimensional objects. To illustrate how the 3-D nature is visualized, remember the window analogy from section 6.1: When looking at the virtual object from different angles through the hologram (or window), one actually has to look at different parts of the hologram (window). This means that the size of the hologram has to be larger or comparable to the size of the object. Therefore, 3-D holograms are classically relatively large holograms (several cm) all of which is illuminated by a large reconstruction beam. This is very impractical compared to the laser pointer sized beams with a diameter of ~ 2 mm used in these experiments. Furthermore, these CGHs are not viewed by looking directly at the hologram but at the projection of the reconstructed light on a screen. Since the screen is flat, the projected holographic reconstruction will of course always be two-dimensional. However, when remembering that the 3-D effects appear when looking at different parts of the hologram, the projection reconstruction method can actually be used for visualizing the 3-D nature of an object in a completely different way. This is done by writing a CGH, which is larger than the reconstruction beam and then reconstructing from different positions on the CGH.

In practice, the 3-D effects are incorporated in the calculation of the holographic interference pattern by assigning different depths to different parts of the object from which the CGH is calculated. Figure 6.7 shows the virtual object used for calculating the CGH seen from two different horizontal angles. It consists of the letters “IFA”, where each letter is placed at a different depth. In figure 6.7 (a) the object is viewed from the front and in (b) from the right-hand side. In both cases they are viewed a bit from above to visualize the three-dimensionality of the object. As can be seen, viewing the object from different angles changes the apparent separation of the letters. A holographic reconstruction of the object behaves in the same way, so when the CGH is reconstructed on a screen and a 2-D projection of the object is seen, a change in viewing angle causes a change in the relative position of the letters. The viewing angle is changed by translating the hologram relative to the reconstruction beam. It should be noted, that the angle of incidence of the reconstruction beam on the CGH is irrelevant as the holographic reconstruction – from a fixed point on the CGH – always appears at the same position relative to the

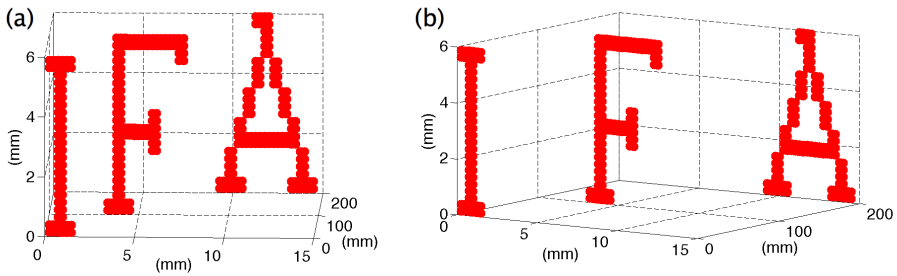


Figure 6.7: Perspective image of the 3-D object that is the basis of the CGH calculation. The object is shown from the front (a) and from the right-hand side (b), and in both cases a bit from above.

directly reflected beam.

To demonstrate this, a rectangular hologram with a size comparable to that of the virtual object ($1.8 \times 10.8 \text{ mm}^2$) has been calculated from the object in figure 6.7. The size of the object can be seen from the axes on figure 6.7. The resulting CGH bit pattern is shown in figure 6.8 together with images of the holographic reconstruction from the two ends of the CGH. In the calculation, the object is placed in front of the right-hand side of the CGH, which means that the reconstruction from the right side is on-axis and the letters are separated with the original spacing. The reconstruction from the left side of the hologram, on the other hand, is off-axis and there is larger separation of the letters. A smooth translation between the two outer positions causes the reconstruction to change smoothly between the two outer positions. A movie of the evolution of the holographic reconstruction as the CGH is translated from right to left and back can be seen in the online version of Ref. [100].

The object is given a small offset in the vertical direction to position the reconstructed image just above the reflection spot, which is why the letters are misaligned in the vertical direction. This could easily be avoided by also assigning different vertical positions to the letters in the calculation of the CGH. Since the 3-D objects are virtual objects, the CGH calculations can be chosen not to include shadowing of elements in the background by elements in the foreground. This way all parts of the hologram will help to reconstruct all the different elements of the 3-D object.

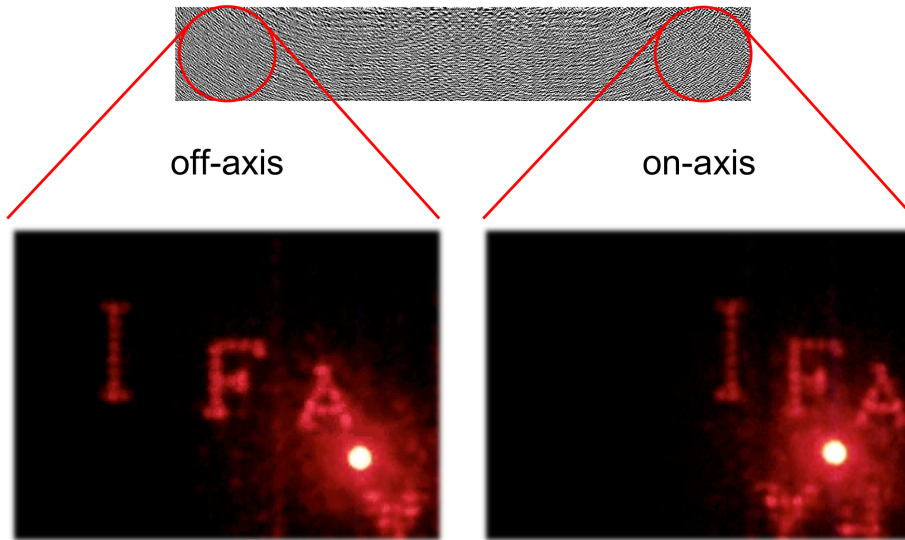


Figure 6.8: Visualization of 3-D effects in directly written CGHs. Top: Rectangular CGH bit pattern of the 3-D object shown in figure 6.7. Bottom: Images of the holographic reconstruction (made with a He-Ne laser) from the on-axis (right) and off-axis (left) ends of the CGH. The hologram used for the reconstruction was made with a pitch of $6\ \mu\text{m}$.

The distance from the CGH where the holographic reconstruction is in focus is determined by the distance between the object and hologram planes in the calculation of the CGH. However, when introducing 3-D effects by varying the depth of the object, the focus distance also varies. Still, the depth of focus (i.e. the range in which the reconstruction is sharp) is larger than the total depth span of the object, so blurring is not visible. This is due to the small size of the holograms, or in the case of the elongated *IFA* hologram the small size of the reconstruction beam. The small aperture compared to the size of the object gives a large depth of focus – analogous to using a pinhole. If the entire hologram is instead illuminated with one broad reconstruction beam, the letters that are not at their correct focal distances on the screen will be visibly out of focus. So, in order to be able to achieve the large depth of focus, which enables the 3-D effects, a small spot size of the reconstruction laser is needed.

6.4 Optimization of the holographic reconstruction

As described above, it has been proven that the femtosecond-laser-written CGHs can in fact be made with high resolution and including 3-D effects. The natural next step is to optimize the hologram parameters to achieve the best holographic reconstruction. However as mentioned in section 6.3.1, with the original setup, the hologram production time was ~ 10 hours. Fortunately, new equipment substantially decreased the production time, thereby enabling this optimization study. The efficiency of the holographic reconstruction is systematically tested against different hologram parameters and compared to theoretical calculations of diffraction efficiencies.

6.4.1 Experimental setup

The general setup used for the production of the CGHs in this study is very similar to the setup described in section 6.3.1. However, two key changes has been made. First, one of the translational stages used for the sample motion was upgraded. The original setup utilized 3 linear, screw-driven stages from Newport (850G actuator) with a maximum speed of 0.5 mm/s. In the new setup, one of these stages was replaced by a magnetically driven, air-bearing stage from Aerotech (ABL1500) with a maximum speed of 2000 mm/s and acceleration of 2 g (~ 20 m/s²). Second, the pulse picking scheme was changed. Instead of using an inhibit signal to modulate the laser output, the trigger signal to the Pockel's cells (see section 3.1.2) was directly controlled. The old technique shut the laser on and off independently of the timing of the laser output, whereas the new one is synchronized with the laser, which enables single shot pulse picking at a 1 kHz rate (maximum laser repetition rate).

The latter change was partly motivated by the first, since the Newport stages (even at full speed) could not fully exploit an individual pulse picking scheme. On the other hand with the new setup, the laser repetition rate was now the limiting factor for the production speed. The speed of the Aerotech stage during hologram writing was determined by the chosen pitch, so that the stage moved exactly one pitch length during the time between two consecutive laser pulses. Hence, this allows a

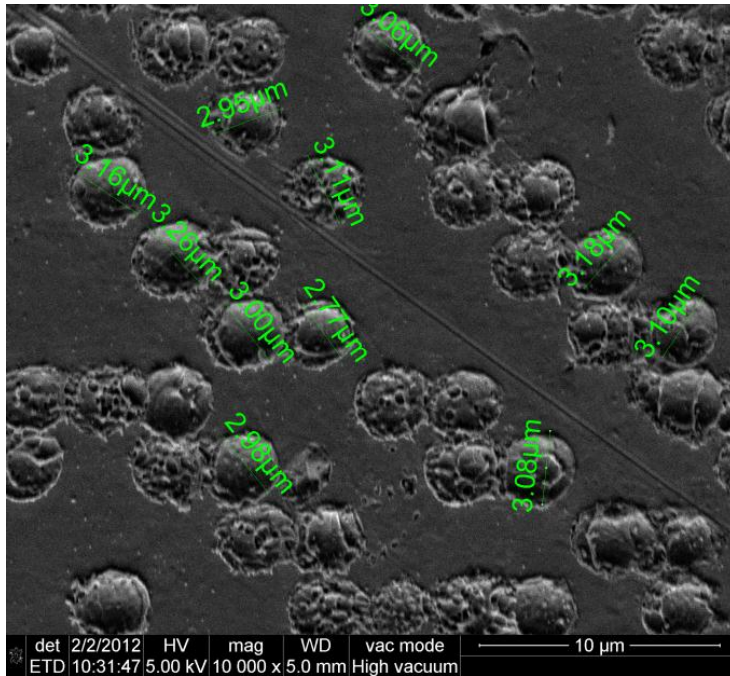


Figure 6.9: SEM image of part of a hologram written on a copper sample with the “new” setup. The pixels are made from single shot ablation. The diameter of a number of the holes is indicated. Image from [120].

maximum pitch of 2 mm, which greatly exceeds the pitches of 2–8 μm used in this study.

The initiation of the Aerotech stage motion is triggered by a signal from the laser to ensure that the motion is always synchronized relative to the laser output. In practice, this means that the individual lines that make up the hologram are aligned to a very high precision. With the upgraded setup, a typical hologram of 700×700 pixels is written in ~ 23 minutes. For more technical details on the two setups and the LabVIEW program that controls the stage motion and pulse picking, see the Master’s thesis of Henrik Hansen [120].

Figure 6.9 shows a SEM image of a section of a hologram written with the new setup. The diameter of the ablated holes is one of the parameters, whose influence on the holographic reconstruction is inves-

tigated. The diameter of a number of the holes in the image have been measured and indicated in the figure. Based on multiple measurements, a mean value and a statistical uncertainty of the diameter is determined for each hologram.

The technique for calculating the CGHs, the lens and the nozzle are identical to those used in the first study. However, in this study, the holograms are written on polished copper surfaces in stead of silicon. Due to the change of material and switch from multi to single shot ablation, the pulse energy is increased to be in the range 0.2–7 μJ . The holographic images are reconstructed on a white screen using a 2 mW He-Ne laser at 633 nm. A digital camera is used to record images of the screen for quantitative measurements of the hologram efficiency. To avoid saturation of the camera when measuring the 0th order diffraction spot, a neutral density filter is inserted, which reduces the intensity by a factor of 440 [120].

6.4.2 Results

An example of an image reconstructed from a laser-written hologram is shown in figure 6.10. The image shows both the normal and the inverted reconstructed image of the first diffraction order on each side of the 0th order spot. If the hologram efficiency is characterized by the power in one holographic reconstruction (i.e. the top right pattern in figure 6.10) relative to the power of the incident beam, this efficiency can be measured as a function of the hologram parameters.

The experimental efficiencies are compared to calculations of diffraction grating efficiencies. The efficiency of a one-dimensional binary amplitude grating can be determined theoretically. The normalized amplitude of the m th diffraction order is given by [121]

$$G_m = \exp(-ima\pi) \int_0^{ma2\pi} \frac{1}{m2\pi} \exp(i\Theta) d\Theta, \quad (6.7)$$

where a is the fill factor (i.e. the ratio of the reflecting to the total area of the grating). The efficiency of the diffraction order is then given by

$$\eta_m = |G_m|^2 = \frac{\sin^2(ma\pi)}{m^2\pi^2}. \quad (6.8)$$

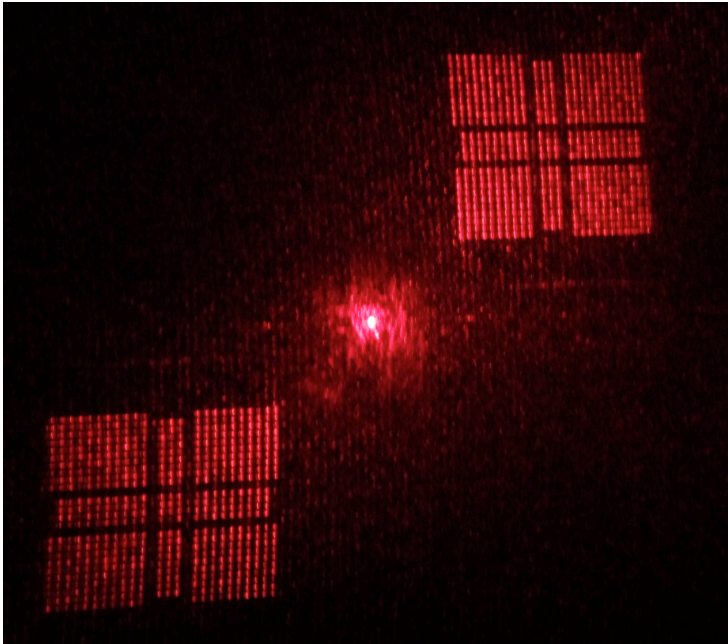


Figure 6.10: Example of a reconstructed holographic image used to characterize the efficiency. Here, the efficiency is defined as the ratio of the power in one reconstructed image (i.e. the top right pattern) to that of the incident beam.

For the first diffraction order, the maximum diffraction efficiency is found for a fill factor of $a = \frac{1}{2}$ to be $\frac{1}{\pi^2}$ (i.e. 10.1 %). Note that this efficiency is actually higher than for a sinusoidal amplitude grating, where the maximum efficiency of the first diffraction order is only 6.25 % [102, 103]. However, the sinusoidal diffraction grating has the advantage of suppressing higher-order diffraction peaks.

Figure 6.11 shows the efficiency as defined above versus the diameter of individual laser holes for a fixed pitch of 6 μm . The coverage (i.e. relative area covered by ablated pixels), $A(d)$, for a given diameter, d , is determined by geometrical calculations based on the actual pixel positions and the circularity of the holes for each individual CGH. For diameters less than 6 μm , the covered area is simply given by the area

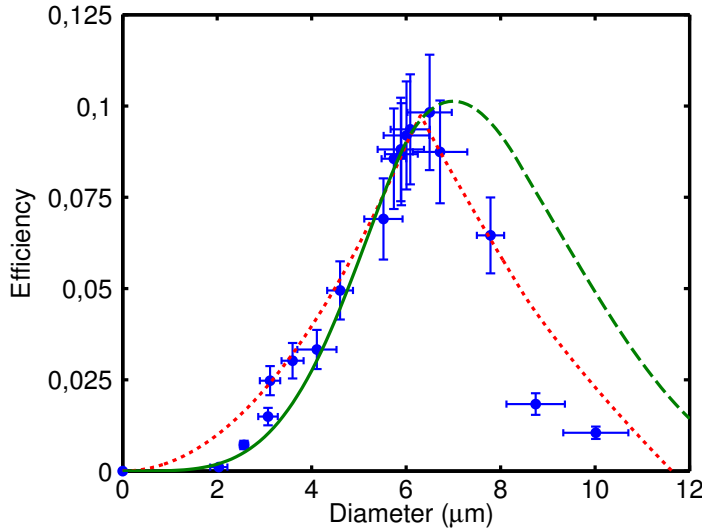


Figure 6.11: Measured efficiency (data points) of the holographic reconstruction as a function of the hole size, together with a theoretical calculation of the diffraction grating efficiency (full and dashed green line), and a fit (dotted red line) to a model described in detail in the text. The full line reflects the region, where the calculation is applicable. The horizontal error bars represent the statistical spread of the measured diameters. The vertical error bars represent an estimate of the efficiency uncertainty determined from the holographic images.

of all the holes, and is therefore proportional to the diameter squared. However, above $6 \mu\text{m}$ the ablated regions start to overlap and, thus, the covered area is less than the sum of the individual areas. The partly full ($d \leq 6 \mu\text{m}$), partly dashed ($d > 6 \mu\text{m}$) green line is the theoretical efficiency given by Eq. (6.8), with a fill factor of $a(d) = 1 - A(d)$. For diameters up to and a bit above the pitch, the theory reproduces the experimental measurements well. Note that this is *without* any scaling or fitting of the experimental data. However, at larger diameters (i.e. smaller fill factor) the theory overestimates the efficiency. This is probably due to the fact that the theory is based on a regular periodic grating. The irregularity of the hologram causes the above-mentioned overlapping

of pixels to be more random, which decreases the holographic reconstruction efficiency compared to that of a perfect periodic grating. The specific formulas for calculating the coverage, when the hole diameter exceeds the pitch, are purely based on geometry. Nevertheless, they are fairly comprehensive and will not be discussed in detail here; see Ref. [120] for details.

To determine the diameter and coverage, where the efficiency is the highest, the experimental data are fitted to a simple model: It is assumed that the efficiency increases linearly with the coverage until a maximum is reached and then decreases linearly with the same slope. That is, the efficiency is fitted with the piecewise function given by

$$\eta(d) = \begin{cases} cA(d) & \text{for } d \leq d_{\text{opt}} \\ c[2A(d_{\text{opt}}) - A(d)] & \text{for } d > d_{\text{opt}} \end{cases}, \quad (6.9)$$

where the slope c and the optimal diameter d_{opt} are free parameters in the fit. The dotted red line in figure 6.11 shows the fit to this model. The fit does not reproduce the initial evolution of the efficiency as well as the analytical theory, but it reproduces the sharp bend and the following rapid decrease more accurately. The optimal diameter is found from the fit to be $6.3 \pm 0.2 \mu\text{m}$. Combined with exactly half the pixels being ablated, this corresponds to an optimal coverage of $A(d_{\text{opt}}) = 43 \pm 2 \%$. The CGHs are calculated as being made up of square pixels, but in reality, the ablated regions are circular. If the hole diameter is equal to the pitch, the ablated region only covers part of the intended pixel area so that $A(d = \text{pitch}) = 39 \%$. On the other hand, if the ablated area for a single hole is set to be equal to the area of the square pixel, the diameter has to be $2/\sqrt{\pi} (\simeq 1.13)$ times larger than the pitch, which gives $A(d) = 48 \%$. However, as mentioned above, when the hole diameter exceeds the pitch, adjacent holes start to overlap and parts of pixels that were supposed to be reflecting become absorbing. Therefore, the optimal diameter and coverage is a compromise between the two. The theoretical optimal coverage is 50 %, which is reached at a pitch of about 7 μm . But at this coverage, the overlap is too dominant and the efficiency has dropped significantly. Nevertheless, the maximum efficiency achieved in the experiment is $\sim 10 \%$, which is close to the theoretical maximum of 10.1 %. The maximum efficiency achieved for these reflection holograms

compare to that achieved for volume gratings also produced by femtosecond lasers, where a maximum efficiency of $\sim 15\%$ is reached [122]. The theoretical maximum for binary volume holograms is 4 times higher (i.e. 40.5 %) than for thin holograms [123].

The efficiency, which is directly proportional to the absolute power in the reconstruction, may not be the most appropriate measure for the quality of the reconstruction. Therefore, we define the transferred power ratio (TPR) as the power in one reconstruction relative to the sum of the powers in the 0th-order spot and the two first-order reconstructions. This gives a relative measure of how much power is transferred from the directly reflected beam into the holographic reconstruction, and thereby how clearly the reconstructed image appears relative to the central (0th order) spot.

Figure 6.12 shows the TPR as a function of diameter for the same data shown in figure 6.11. The theoretical TPR (full and dashed green line) has again been calculated by Eq. (6.8) (note: the 0th order diffraction efficiency is simply given by $E_0 = a^2$). Again, the theory reproduces the experimental data well up to and a bit above the pitch, and not very well at larger diameters. The theory actually predicts a continuously increasing TPR that approaches $\frac{1}{3}$ (or 33 %) for the coverage approaching 100 %. Nevertheless, for the same reasons as mentioned above, the measured TPR in fact reaches a maximum value for an optimal diameter and coverage.

Once again, a simpler model has been used to fit the data to determine the optimal values. There is a decrease in the total power reflected from the hologram with increasing diameter due to the corresponding decrease of the area of the reflecting part of the hologram. Measurements show that the total power drops linearly with the reflecting area (data not shown), as expected by summation of Eq. (6.8) over all diffraction orders. Hence, the data in figure 6.12 are fitted to Eq. (6.9) divided by a function that is linearly decreasing with $A(d)$:

$$\text{TPR}(d) = \begin{cases} \frac{cA(d)}{1 - A(d)} & \text{for } d \leq d_{\text{opt}} \\ \frac{c[2A(d_{\text{opt}}) - A(d)]}{1 - A(d)} & \text{for } d > d_{\text{opt}} \end{cases}, \quad (6.10)$$

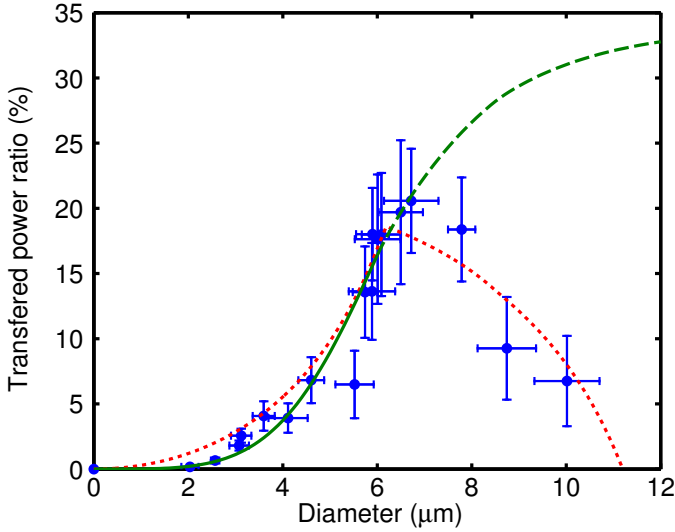


Figure 6.12: Measured TPR (data points) of the holographic reconstruction as a function of the hole size, together with a theoretical calculation (full and dashed green line), and a fit (dotted red line) to a model described in detail in the text. The full line reflects the region, where the calculation is applicable.

In this fit (dotted red line in figure 6.12), the optimal diameter is found to be $6.2 \pm 0.2 \mu\text{m}$ corresponding to an optimal coverage of $42 \pm 2 \%$, which agrees within uncertainties with the fit in figure 6.11. About 20 % of the power (see figure 6.12) is transferred into the reconstructed image at hole diameters close to the optimal one, which fits well with the theoretical value of 22 % at a coverage of 50 %.

The reconstruction efficiency has also been tested as a function of the hologram pitch. For these measurements, CGHs have been calculated to reconstruct the same image (shown in figure 6.10) but with different pitches resulting in different CGH patterns. As mentioned in section 6.3.2, when increasing the resolution (i.e. decreasing the pitch) larger holographic images can be reconstructed without overlap between different diffraction orders. In each calculation, the size of the reconstructed image is scaled to take up the same relative area between the

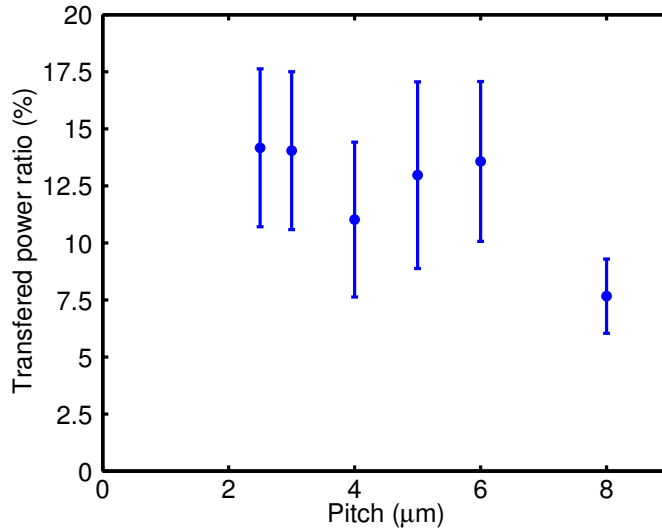


Figure 6.13: Measured TPR as a function of hologram pitch for a fixed coverage of $\sim 39\%$. The pitch uncertainty is less than the data point size.

0th and higher order diffraction spots – this means that the actual size of the reconstructed image increases with decreasing pitch. In this experiment, when writing the CGHs on the copper sample, the diameter of the holes is kept almost the same as the pitch, which ensures that the coverage is constant ($\sim 39\%$). Figure 6.13 shows the TPR as a function of the pitch. For pitches up to $6\ \mu\text{m}$, the TPR is seen to be fairly constant. As expected, the power in a reconstructed image does not increase with increased resolution, since the maximum efficiency is already reached at the $6\ \mu\text{m}$ pitch. However, although it does not increase the diffraction efficiency, the increased resolution has the advantages discussed in section 6.3.2: It enables reconstruction of larger images without overlap between different diffraction orders. Also, owing to the increase in information in the hologram, the increased resolution gives sharper images, which means that more detailed objects can be successfully reconstructed [100].

6.5 Discussion

The use of femtosecond-laser ablation for direct writing of CGHs on a surface has been investigated. CGHs are successfully produced on both semiconductors (Si) and metals (Cu). The proof-of-principle study shows that high resolution can be obtained and demonstrates how 3-D effects can be incorporated in the holograms. The optimization study determines how an ideal reconstruction efficiency can be obtained.

Silicon is a semiconductor with a band gap of 1.11 eV [124], and the photon energy of the 800 nm femtosecond pulses is 1.55 eV. Hence, ablation of silicon – as well as copper – is a linear (single-photon) process. If the CGHs are written on the surface of or inside a high band gap material (dielectric) [112–114], the absorption is a non-linear (multi-photon) process; as described in chapter 2. Since the minimal focal spot size is diffraction limited, it is possible to generate smaller structures and thereby achieve a higher resolution of the CGHs when working with dielectrics instead of, e.g., silicon or copper. However, the purpose of this study was also to show that relatively detailed CGHs can be made with the resolution achievable on the surface of metals or silicon – despite the linear absorption regime.

In the image of the reconstructed seal of Aarhus University seen in figure 6.6 (b), the sharpness of the reconstruction decreases visibly towards the left side of the image. This is probably due to poor alignment of the pixels in the vertical direction, which can be seen in the overview SEM image of the hologram (figure 6.5 (a)). This hologram is fabricated with the “old” setup. The pixels are written row by row while the translational stage is moving the sample. However, when a row is written, the initiation of the motion is not synchronized with the laser output, so the single-shot pixels may be offset relative to each other. The vertical translation is done in between writing the rows, which explains the good horizontal alignment. This misalignment is likely to cause the observed blurring in the interference pattern that makes up the holographic reconstruction. In the “new” setup, the horizontal motion of the stage is synchronized to the laser output, as explained in section 6.4.1. This ensures that the individual lines are much better aligned. Indeed, the reconstructions in figure 6.10 are *not* more blurry in one direction compared to the other (i.e. right-left versus up-down). Note that the decrease in visibility towards the edges of the figure is simply due to the

fact that the light intensity always decreases away from the 0th order spot. Since blurring is not observed in the reconstructions from the new setup, this supports the explanation of bad alignment.

The holograms made in this project are written on the surfaces of silicon and copper samples. However, as mentioned above, they could be produced on any reflecting or transmitting surface, e.g., also plastic surfaces. As an example, a CGH has been written on a piece of transparency film. With the transparent sample, both reflection and transmission holographic images are reconstructed. The small thickness of the sample makes it flexible. Bending the sample (even very slightly) destroys the reflection reconstruction, due to the reflected light no longer being spatially coherent. Since the holographic reconstruction is based on interference between light from different parts of the hologram, just bending the hologram a fraction of the laser wavelength (~ 100 nm) will cause the reflection reconstruction to disappear. On the other hand, the transmission reconstruction is hardly affected by the bending as the transmitted light remains spatially coherent.

As described in section 6.2, the femtosecond-laser direct-writing method is well suited for the production of unique CGHs, which makes it particularly suitable for security applications: The holograms that may include a unique code are easy to reconstruct but hard to replicate, since a femtosecond laser or a similar tool is needed to produce the tiny spots forming the hologram. The small (millimeter) size of the hologram also makes it possible to hide the hologram or produce it on small items, while the much larger reconstructed image is readily visible. The installation of the Aerotech stages (described section 6.4.1) reduced the production time significantly, e.g., ~ 10 hours to ~ 23 minutes for a 700×700 pixels hologram. This may be compatible with some industrial production lines, but it is possible to decrease it further. Currently, the laser repetition rate (of 1 kHz) is the limiting factor determining the writing speed. However, e.g., femtosecond-laser systems with repetition rates up to 5.1 MHz, short pulses (< 50 fs) and sufficient pulse energy (> 100 – 500 nJ depending on the system) are available from Femtolasers [125]. At this repetition rate, the 700×700 pixels could be written in less than 0.1 second. However, with such a system, the writing speed is actually limited by the acceleration time of the stages. Still, the 700 lines can be written in about 1 min with a laser repetition rate of 667 kHz. This project focuses on proof-of-principle and optimization of the laser-written CGHs

and not industrial implementation. However, the equipment necessary to fabricate the CGHs at speeds compatible with production lines does exist.

Summary

This thesis studies the interaction between ultrashort-laser pulses and materials, and how this interaction modifies the material. Emphasis is on the changes in the material optical properties related to the laser-excitation. The first part combines experiments and numerical modeling to investigate fundamental aspects of the laser-matter interaction. In the second part, laser-induced reflectance modifications are applied to produce computer-generated holograms (CGHs) on different surfaces.

A numerical model describing the ultrashort-pulse excitation of dielectric materials is developed. The model is based on the multiple-rate equations (MRE) model by Rethfeld [15], which was expanded by Christensen and Balling [36] to include optical propagation. It takes into account strong-field excitation in a Keldysh picture [8], electron heating by plasma absorption, and collisional excitation. In the present thesis, much attention is given to accurately describing the inherent optical properties, which is essential for comparison to experimental studies.

Experiments carried out at Aarhus University study how the self-reflectance and ablation depth depend on the fluence of femtosecond-laser pulses for a sapphire sample. At first, the self-reflectance increases with increasing pulse fluence, as is expected due to the so-called plasma-mirror effect. However, at the highest applied fluences, the self-reflectance de-

creases. The ablation depth results are characterized by a distinct threshold, a steep increase after the threshold, and a quick stabilization at an almost constant level. Numerical simulations based on the above-mentioned model reproduce the experimental data well, including the high-fluence decrease in the self-reflectance as well as the threshold and steep increase in ablation depth, however, at the highest fluence, the simulations overestimate the ablation depth.

Reflectance and ablation depth measurements are combined with spectral-interferometry measurements in experiments carried out in collaboration with the group of Guizard at the “Centre Energie Atomique” in Sacclay, France. This combined experiment enables studying a large range of fluences, as the spectral interferometry measurements are made at significantly lower fluences than the reflectance and hole-depth measurements. In addition, the experiment employs a pump-probe scheme, which allows measuring the probe reflectance instead of the self-reflectance. These results are also compared to numerical simulations and good agreement is achieved – even over the large fluence range and for various pulse durations. Different refinements of the model are made, motivated by the addition of the low-fluence measurements.

Furthermore, the model is applied to describe the excitation of water by laser pulses with different temporal shapes. Spectral-interferometry experiments have been carried out in the group of Baumert at the University of Kassel [48] using three different pulse shapes, which enables investigating the role of collisional excitation. Therefore, the aim is to reproduce the experimental data using the model, which is still a work in progress. Simultaneous agreement is achieved for two of three pulse shapes, but it seems that further modifications to the model is needed for an adequate description that succeeds in reproducing all the data.

The second part of this thesis investigates laser-written CGHs. Laser ablation changes the surface morphology and, thus, the optical properties of the surface. Initially reflecting surfaces can become strongly scattering and absorbing. Selectively ablating a calculated CGH pattern onto a surface locally reduces the reflectance (on a microscopic scale) and alters the macroscopic optical properties of that surface. Illuminating the hologram with a standard laser pointer produces a holographic image to be seen on a screen. In this thesis, high-resolution CGHs are demonstrated – with the possibility of including 3-D effects. In addition, the hologram efficiency is systematically studied and optimal parameters are derived.

Dansk resumé

Denne Ph.D.-afhandling omhandler vekselvirkningen mellem ultrakorte laserpulser og materialer, og hvilken effekt denne vekselvirkning har på materialet. Afhandlingen har særlig fokus på de optiske egenskaber af materialet, som ændrer sig, når det bliver eksiteret af laserpulsen. Første del kombinerer eksperimenter med numerisk modellering i en undersøgelse af fundamentale aspekter af vekselvirkningen mellem dielektriske materialer og laserpulserne. I anden del anvendes laserinducerede refleksionsændringer til at fremstille computer-genererede hologrammer (CGH'er) på forskellige overflader.

En model, som beskriver eksitationen af dielektriske materialer med ultrakorte laserpulser, er blevet udviklet. Modellen er baseret på den såkaldte “multiple-rate equations model”, som oprindeligt er udviklet af Rethfeld [15] og udvidet af Christensen og Balling [36] til at inkludere optisk udbredning. I modellen inkluderes stærkfeltseksitation, som beskrevet af Keldysh [8], elektronopvarmning forårsaget af plasmaabsorption samt kollisionseksitation. I denne afhandling bliver der lagt særlig vægt på beskrivelsen af materialets optiske egenskaber, som er væsentlige i sammenligningen med de udførte eksperimenter.

I eksperimenter udført på Aarhus Universitet studeres, hvordan selvreflektansen og ablationsdybden afhænger af laserfluensen (pulsenergi

per areal) for safir. For stigende fluens observeres først en stigende selv-reflektans, hvilket er en forventelig følge af den såkaldte plasmaspjelleffekt. Ved de højeste fluenser ses til gengæld et fald i selv-reflektansen, hvilket umiddelbart er overraskende. Målingerne af ablationsdybden er karakteriseret ved en tydelig tærskel efterfulgt af en brat stigning og en hurtig stabilisering på et næsten konstant niveau. De numeriske simuleringer baseret på den ovennævnte model gengiver de eksperimentelle resultater godt – inklusiv faldet i selv-reflektans ved høje fluenser og både tærsklen og den bratte stigning i ablationsdybden, men ved de højeste fluenser overvurderer simuleringerne ablationsdybden.

Målinger af reflektans og ablationsdybde kombineres med målinger baseret på spektral interferometri i eksperimenter udført i samarbejde med Professor Stéphane Guizard's gruppe ved "Centre Energie Atomique" (CEA) i Sacclay, Frankrig. Da interferometrimålingerne laves ved markant lavere fluenser end reflektans- og ablationsdybdemålingerne, kan et større fluensinterval undersøges med dette eksperiment. Den eksperimentelle opstilling er baseret på et pumpe-probe-system, som muliggør måling af probe-reflektans i stedet for selv-reflektans. Resultaterne fra disse forsøg er også sammenlignet med numeriske simuleringer og god overensstemmelse er opnået – selv over det store fluensinterval og for forskellige pulsvarigheder. På basis af tilføjelsen af lavfluensmålingerne er modellen blevet modificeret en anelse.

Modellen er desuden blevet anvendt til at beskrive eksitationen af vand med laserpulser med forskellige tidslige udformninger. Professor Thomas Baumerts gruppe ved University of Kassel har lavet spektral-interferometri-eksperimenter med tre forskellige pulsudformninger, som gør det muligt at undersøge kollisionseksitationens rolle. Målet er derfor at reproducere de eksperimentelle data ved brug af modellen, hvilket er et igangværende arbejde. Der er opnået samtidig overensstemmelse mellem data og simuleringer for to ud af de tre pulsudformninger, men det lader til, at yderligere modifikationer af modellen er nødvendige for at få en fyldestgørende og tilstrækkelige beskrivelse af materialeeksitationen.

Anden del undersøger laserskrevne CGH'er. Laserablation ændrer materialets overflademorfologi og derved de optiske egenskaber, og f.eks. kan overflader, som oprindeligt er reflekterende, blive meget spredende og absorberende. Ved selektivt at ablere et CGH-mønster på en overflade reduceres reflektansen lokalt (på mikroskopisk skala), hvorved de makroskopiske optiske egenskaber ændres. Belyses hologrammet med

f.eks. en almindelig laserpointer, skabes et holografisk billede, som kan ses på en skærm. I denne afhandling er CGH'er med høj opløsning og med mulighed for at integrere 3-D effekter demonstreret. Derudover er effektiviteten af de producerede hologrammer undersøgt systematisk, og de optimale parametre er bestemt.

Bibliography

- [1] D. Bäuerle, *Laser Processing and Chemistry* (Springer-Verlag Berlin Heidelberg, Germany, 2011), 4th edition.
- [2] P. Balling and J. Schou, *Femtosecond-laser ablation dynamics of dielectrics: basics and applications for thin films*, Reports on Progress in Physics **76**, 036502 (2013).
- [3] E. G. Gamaly, *The physics of ultra-short laser interaction with solids at non-relativistic intensities*, Physics Reports – Review Section of Physics Letters **508**, 91 (2011).
- [4] R. R. Gattass and E. Mazur, *Femtosecond laser micromachining in transparent materials*, Nature Photonics **2**, 219 (2008).
- [5] N. Bloembergen, *A brief history of light breakdown*, Journal of Non-linear Optical Physics and Materials **6**, 377 (1997).
- [6] E. E. B. Campbell, D. Ashkenasi, and A. Rosenfeld, *Ultra-short-pulse laser irradiation and ablation of dielectrics*, Lasers in Materials Science **301**, 123 (1999).
- [7] W. Kautek and J. Kruger, *Femtosecond pulse laser ablation of metallic, semiconducting, ceramic, and biological materials*, Proceedings of SPIE **2207**, 600 (1994).
- [8] L. V. Keldysh, *Ionization in Field of a Strong Electromagnetic Wave*, Soviet Physics Jetp-Ussr **20**, 1307 (1965).
- [9] J. D. Jackson, *Classical Electrodynamics* (Wiley, New York, USA, 1999), 3rd edition.

-
- [10] R. Loudon, *The propagation of electromagnetic energy through an absorbing dielectric*, Journal of Physics Part A General **3**, 233 (1970).
- [11] J. M. Liu, *Simple technique for measurements of pulsed Gaussian-beam spot sizes*, Optics Letters **7**, 196 (1982).
- [12] P. P. Pronko, S. K. Dutta, J. Squier, J. V. Rudd, D. Du, and G. Mourou, *Machining of submicron holes using a femtosecond laser at 800-nm*, Optics Communications **114**, 106 (1995).
- [13] K. Vestentoft, J. Olesen, B. Christensen, and P. Balling, *Nanostructuring of surfaces by ultra-short laser pulses*, Applied Physics A **80**, 493 (2005).
- [14] L. Englert, M. Wollenhaupt, C. Sarpe, D. Otto, and T. Baumert, *Morphology of nanoscale structures on fused silica surfaces from interaction with temporally tailored femtosecond pulses*, Journal of Laser Applications **24**, 042002 (2012).
- [15] B. Rethfeld, *Unified Model for the Free-Electron Avalanche in Laser-Irradiated Dielectrics*, Physical Review Letters **92**, 187401 (2004).
- [16] K. Wædegaard, M. Frislev, L. A. Kjaer, and P. Balling, *Femtosecond laser excitation of dielectric materials: Optical properties and ablation*, AIP Conference Proceedings **1464**, 32 (2012).
- [17] K. Wædegaard, M. Frislev, and P. Balling, *Femtosecond Laser Excitation of Dielectric Materials: Experiments and Modeling of Optical Properties and Ablation Depths*, Applied Physics A **110**, 601 (2013).
- [18] K. J. Wædegaard, D. B. Sandkamm, A. Mouskeftaras, S. Guizard, and P. Balling, *Modeling of short-pulse laser excitation of dielectrics*, Physical Review Letters, submitted (2013).
- [19] K. J. Wædegaard, C. Sarpe, T. Winkler, J. Köhler, M. Wollenhaupt, T. Baumert, and P. Balling, *Excitation of water by temporally shaped femtosecond laser pulses: Measuring and modeling the transient optical properties including propagation*, in preparation (2013).
- [20] P. Audebert, P. Daguzan, A. Dos Santos, J. C. Gauthier, J. P. Geindre, S. Guizard, G. Hamoniaux, K. Krastev, P. Martin, G. Petite, and

- A. Antonetti, *Space-Time Observation of an Electron Gas in SiO₂*, Physical Review Letters **73**, 1990 (1994).
- [21] B. C. Stuart, M. D. Feit, S. Herman, A. M. Rubenchik, B. W. Shore, and M. D. Perry, *Nanosecond-to-femtosecond laser-induced breakdown in dielectrics*, Physical Review B **53**, 1749 (1996).
- [22] P. Martin, S. Guizard, P. Daguzan, G. Petite, P. D'Oliveira, P. Meynadier, and M. Perdrix, *Subpicosecond study of carrier trapping dynamics in wide-band-gap crystals*, Physical Review B **55**, 5799 (1997).
- [23] M. Li, S. Menon, J. P. Nibarger, and G. N. Gibson, *Ultrafast Electron Dynamics in Femtosecond Optical Breakdown of Dielectrics*, Physical Review Letters **82**, 2394 (1999).
- [24] A. Kaiser, B. Rethfeld, M. Vicanek, and G. Simon, *Microscopic processes in dielectrics under irradiation by subpicosecond laser pulses*, Physical Review B **61**, 11437 (2000).
- [25] T. Apostolova and Y. Hahn, *Modeling of laser-induced breakdown in dielectrics with subpicosecond pulses*, Journal of Applied Physics **88**, 1024 (2000).
- [26] S. Guizard, A. Semerok, J. Gaudin, A. Hashida, P. Martin, and F. Quere, *Femtosecond laser ablation of transparent dielectrics: measurement and modelisation of crater profiles*, Applied Surface Science **186**, 364 (2002).
- [27] M. D. Feit, A. M. Komashko, and A. M. Rubenchik, *Ultra-short pulse laser interaction with transparent dielectrics*, Applied Physics A **79**, 1657 (2004).
- [28] N. M. Bulgakova, R. Stoian, A. Rosenfeld, I. V. Hertel, and E. E. B. Campbell, *Electronic transport and consequences for material removal in ultrafast pulsed laser ablation of materials*, Physical Review B **69**, 054102 (2004).
- [29] L. Jiang and H. L. Tsai, *Energy transport and material removal in wide bandgap materials by a femtosecond laser pulse*, International Journal of Heat and Mass Transfer **48**, 487 (2005).

-
- [30] J. R. Peñano, P. Sprangle, B. Hafizi, W. Manheimer, and A. Zigler, *Transmission of intense femtosecond laser pulses into dielectrics*, Physical Review E **72**, 036412 (2005).
- [31] J. R. V. de Aldana, C. Méndez, L. Roso, and P. Moreno, *Propagation of ablation channels with multiple femtosecond laser pulses in dielectrics: numerical simulations and experiments*, Journal of Physics D: Applied Physics **38**, 2764 (2005).
- [32] B. Rethfeld, *Free-electron generation in laser-irradiated dielectrics*, Physical Review B **73**, 035101 (2006).
- [33] G. M. Petrov and J. Davis, *Interaction of intense ultra-short laser pulses with dielectrics*, Journal of Physics B: Atomic, Molecular and Optical Physics **41**, 025601 (2008).
- [34] L. Jiang and H.-L. Tsai, *A plasma model combined with an improved two-temperature equation for ultrafast laser ablation of dielectrics*, Journal of Applied Physics **104**, 093101 (2008).
- [35] V. Gruzdev and J. Chen, *Laser-induced ionization and intrinsic breakdown of wide band-gap solids*, Applied Physics A **90**, 255 (2008).
- [36] B. H. Christensen and P. Balling, *Modeling ultrashort-pulse laser ablation of dielectric materials*, Physical Review B **79**, 155424 (2009).
- [37] T. E. Itina, O. Utéza, N. Sanner, and M. Sentis, *Interaction of femtosecond laser pulses with dielectric materials: insights from numerical modelling*, Journal of Optoelectronics and Advanced Materials **12**, 470 (2010).
- [38] B. Rethfeld, O. Brenk, N. Medvedev, H. Krutsch, and D. H. H. Hoffmann, *Interaction of dielectrics with femtosecond laser pulses: application of kinetic approach and multiple rate equation*, Applied Physics A **101**, 19 (2010).
- [39] A. Bourgeade, C. Mézel, and O. Saut, *Modeling the Early Ionization of Dielectrics by Ultrashort Laser Pulses*, Journal of Scientific Computing **44**, 170 (2010).

- [40] N. M. Bulgakova, R. Stoian, and A. Rosenfeld, *Laser-induced modification of transparent crystals and glasses*, *Quantum Electronics* **40**, 966 (2010).
- [41] B. Chimier, O. Utéza, N. Sanner, M. Sentis, T. Itina, P. Lassonde, F. Légaré, F. Vidal, and J. C. Kieffer, *Damage and ablation thresholds of fused-silica in femtosecond regime*, *Physical Review B* **84**, 094104 (2011).
- [42] N. S. Shcheblanov, E. P. Silaeva, and T. E. Itina, *Electronic excitation and relaxation processes in wide band gap dielectric materials in the transition region of the Keldysh parameter*, *Applied Surface Science* **258**, 9417 (2012).
- [43] C. Mézel, A. Bourgeade, and L. Hallo, *Surface structuring by ultrashort laser pulses: A review of photoionization models*, *Physics of Plasmas* **17**, 113504 (2010).
- [44] B. C. Stuart, M. D. Feit, A. M. Rubenchik, B. W. Shore, and M. D. Perry, *Laser-Induced Damage in Dielectrics with Nanosecond to Subpicosecond Pulses*, *Physical Review Letters* **74**, 2248 (1995).
- [45] M. D. Perry, B. C. Stuart, P. S. Banks, M. D. Feit, V. Yanovsky, and A. M. Rubenchik, *Ultrashort-pulse laser machining of dielectric materials*, *Journal of Applied Physics* **85**, 6803 (1999).
- [46] P. K. Kennedy, *A first-order model for computation of laser-induced breakdown threshold in ocular and aqueous-media. 1. Theory*, *Journal of Quantum Electronics* **31**, 2241 (1995).
- [47] A. Vogel, J. Noack, G. Huttman, and G. Paltauf, *Mechanisms of femtosecond laser nanosurgery of cells and tissues*, *Applied Physics B* **81**, 1015 (2005).
- [48] C. Sarpe, J. Köhler, T. Winkler, M. Wollenhaupt, and T. Baumert, *Real-time observation of transient electron density in water irradiated with tailored femtosecond laser pulses*, *New Journal of Physics* **14**, 075021 (2012).
- [49] N. W. Ashcroft and D. N. Mermin, *Solid State Physics* (Holt, Rinehart and Winston, Philadelphia, USA, 1976).

-
- [50] V. E. Gruzdev, *Laser-induced ionization of solids: back to Keldysh*, Proceedings of SPIE **5647**, 480 (2005).
- [51] A. C. Tien, S. Backus, H. Kapteyn, M. Murnane, and G. Mourou, *Short-pulse laser damage in transparent materials as a function of pulse duration*, Physical Review Letters **82**, 3883 (1999).
- [52] M. N. Christensen, J. Byskov-Nielsen, B. H. Christensen, and P. Balling, *Single-shot ablation of sapphire by ultrashort laser pulses*, Applied Physics A **101**, 279 (2010).
- [53] B. K. Ridley, *Quantum Processes in Semiconductors* (Clarendon, Oxford, UK, 1982).
- [54] F. Quere, S. Guizard, and P. Martin, *Time-resolved study of laser-induced breakdown in dielectrics*, Europhysics Letters **56**, 138 (2001).
- [55] F. L. Pedrotti, L. S. Pedrotti, and L. M. Pedrotti, *Introduction to Optics* (Pearson Education, Upper Saddle River, USA, 2007), 3rd edition.
- [56] B. Rethfeld, H. Krutsch, and D. H. H. Hoffmann, *Tracing Laser-Induced Dielectric Breakdown in Solids*, Contributions to Plasma Physics **50**, 16 (2010).
- [57] Y. T. Lee and R. M. More, *An electron conductivity model for dense plasmas*, Physics of Fluids **27**, 1273 (1984).
- [58] K. Eidmann, J. M. ter Vehn, T. Schlegel, and S. Hüller, *Hydrodynamic simulation of subpicosecond laser interaction with solid-density matter*, Physical Review E **62**, 1202 (2000).
- [59] H. D. Young and R. A. Freedman, *Sears and Zemansky's University Physics* (Addison-Wesley, Boston, USA, 2012), 13th edition.
- [60] F. Mandl, *Statistical Physics* (Wiley, Chichester, UK, 1988), 2nd edition.
- [61] L. D. Landau and E. M. Lifshitz, *Electrodynamics of continuous media* (Pergamon Press Ltd., Oxford, UK, 1963), 2nd edition.

- [62] N. Medvedev and B. Rethfeld, *A comprehensive model for the ultra-short visible light irradiation of semiconductors*, Journal of Applied Physics **108**, 103112 (2010).
- [63] R. Ruppin, *Electromagnetic energy density in a dispersive and absorptive material*, Physics Letters A **299**, 309 (2002).
- [64] F. D. Nunes, T. C. Vasconcelos, M. Bezerra, and J. Weiner, *Electromagnetic energy density in dispersive and dissipative media*, Journal of the Optical Society of America B-Optical Physics **28**, 1544 (2011).
- [65] O. Brenk and B. Rethfeld, *Electron dynamics in transparent materials under high-intensity laser irradiation*, Proceedings of SPIE **8190**, 15 (2011).
- [66] R. Car and M. Parrinello, *Unified approach for molecular dynamics and density-functional theory*, Physical Review Letters **55**, 2471 (1985).
- [67] N. Medvedev, H. O. Jeschke, and B. Ziaja, *Nonthermal phase transitions in semiconductors induced by a femtosecond extreme ultraviolet laser pulse*, New Journal of Physics **15**, 015016 (2013).
- [68] S. K. Sundaram and E. Mazur, *Inducing and probing non-thermal transitions in semiconductors using femtosecond laser pulses*, Nature Materials **1**, 217 (2002).
- [69] S. Klimentov, P. Pivovarov, N. Fedorov, S. Guizard, F. Dausinger, and V. Konov, *Conical emission in focused beams: analysis of contributing factors and elimination of scattering*, Applied Physics B **105**, 495 (2011).
- [70] C. Rullière (editor), *Femtosecond Laser Pulses: Principles and Experiments* (Springer, New York, USA, 2005), 2nd edition.
- [71] J.-M. Savolainen, *The nature of femtosecond laser ablation: Experiments on single-crystalline aluminium under ultra-high vacuum conditions*, Master's thesis, Aarhus University, Denmark (2010).
- [72] http://www.mt-berlin.com/frames_cryst/descriptions/sapphire.htm.

- [73] J. E. Medvedeva, E. N. Teasley, and M. D. Hoffman, *Electronic band structure and carrier effective mass in calcium aluminates*, Physical Review B **76**, 155107 (2007).
- [74] D. E. Gray (editor), *American Institute of Physics Handbook* (McGraw-Hill, New York, 1972), 3rd edition.
- [75] R. H. French, *Electronic Band Structure of Al₂O₃, with Comparison to Alon and AlN*, Journal of the American Ceramic Society **73**, 477 (1990).
- [76] F. Träger (editor), *Springer Handbook of Lasers and Optics* (Springer, New York, 2007).
- [77] A. P. Joglekar, H.-h. Liu, E. Meyhöfer, G. Mourou, and A. J. Hunt, *Optics at critical intensity: Applications to nanomorphing*, Proceedings of the National Academy of Sciences of the United States of America **101**, 5856 (2004).
- [78] D. Puerto, J. Siegel, W. Gawelda, M. Galvan-Sosa, L. Ehrentraut, J. Bonse, and J. Solis, *Dynamics of plasma formation, relaxation, and topography modification induced by femtosecond laser pulses in crystalline and amorphous dielectrics*, Journal of the Optical Society of America B-Optical Physics **27**, 1065 (2010).
- [79] L. Qi, K. Nishii, M. Yasui, H. Aoki, and Y. Namba, *Femtosecond laser ablation of sapphire on different crystallographic facet planes by single and multiple laser pulses irradiation*, Optics and Lasers In Engineering **48**, 1000 (2010).
- [80] V. V. Temnov, K. Sokolowski-Tinten, P. Zhou, and D. von der Linde, *Femtosecond time-resolved interferometric microscopy*, Applied Physics A **78**, 483 (2004).
- [81] V. V. Temnov, K. Sokolowski-Tinten, P. Zhou, A. El-Khamhawy, and D. von der Linde, *Multiphoton ionization in dielectrics: Comparison of circular and linear polarization*, Physical Review Letters **97**, 237403 (2006).
- [82] E. Tokunaga, A. Terasaki, and T. Kobayashi, *Frequency-domain interferometer for femtosecond time-resolved phase spectroscopy*, Optics Letters **17**, 1131 (1992).

- [83] J. P. Geindre, P. Audebert, A. Rousse, F. Fallières, J. C. Gauthier, A. Mysyrowicz, A. D. Santos, G. Hamoniaux, and A. Antonetti, *Frequency-domain interferometer for measuring the phase and amplitude of a femtosecond pulse probing a laser-produced plasma*, Optics Letters **19**, 1997 (1994).
- [84] A. Mouskeftaras, S. Guizard, N. Fedorov, and S. Klimentov, *Mechanisms of femtosecond laser ablation of dielectrics revealed by double pump-probe experiment*, Applied Physics A **110**, 709 (2013).
- [85] V. V. Kononenko, E. V. Zavedeev, M. I. Latushko, and V. I. Konov, *Observation of fs laser-induced heat dissipation in diamond bulk*, Laser Physics Letters **10**, 036003 (2013).
- [86] A. Major, F. Yoshino, I. Nikolakakos, J. Aitchison, and P. Smith, *Dispersion of the nonlinear refractive index in sapphire*, Optics Letters **29**, 602 (2004).
- [87] A. Facchetti and T. Marks (editors), *Transparent Electronics: From Synthesis to Applications* (Wiley, Chichester, UK, 2010).
- [88] W. L. Masterton, E. J. Slowinski, and C. L. Stanitski, *Chemical Principles* (Saunders, Philadelphia, USA, 1983), alternate edition.
- [89] A. B. Thompson, *Gibbs energy of aluminous minerals*, Contributions to Mineralogy and Petrology **48**, 123 (1974).
- [90] J. Hernandez-Rueda, D. Puerto, J. Siegel, M. Galvan-Sosa, and J. Solis, *Plasma dynamics and structural modifications induced by femtosecond laser pulses in quartz*, Applied Surface Science **258**, 9389 (2012).
- [91] D. Puerto, W. Gawelda, J. Siegel, J. Bonse, G. Bachelier, and J. Solis, *Transient reflectivity and transmission changes during plasma formation and ablation in fused silica induced by femtosecond laser pulses*, Applied Physics A **92**, 803 (2008).
- [92] M. Wollenhaupt, M. Krug, J. Köhler, T. Bayer, C. Sarpe-Tudoran, and T. Baumert, *Photoelectron angular distributions from strong-field coherent electronic excitation*, Applied Physics B **95**, 245 (2009).

- [93] C. A. Sacchi, *Laser-induced electric breakdown in water*, Journal of the Optical Society of America B-Optical Physics **8**, 337 (1991).
- [94] C. L. Thomsen, D. Madsen, S. R. Keiding, J. Thogersen, and O. Christiansen, *Two-photon dissociation and ionization of liquid water studied by femtosecond transient absorption spectroscopy*, The Journal of Chemical Physics **110**, 3453 (1999).
- [95] C. G. Elles, A. E. Jailaubekov, R. A. Crowell, and S. E. Bradforth, *Excitation-energy dependence of the mechanism for two-photon ionization of liquid H_2O and D_2O from 8.3 to 12.4 eV*, The Journal of Chemical Physics **125**, 044515 (2006).
- [96] C. G. Elles, I. A. Shkrob, R. A. Crowell, and S. E. Bradforth, *Excited state dynamics of liquid water: Insight from the dissociation reaction following two-photon excitation*, The Journal of Chemical Physics **126**, 164503 (2007).
- [97] F.-Y. Jou and G. R. Freeman, *Temperature and isotope effects on the shape of the optical absorption spectrum of solvated electrons in water*, The Journal of Physical Chemistry **83**, 2383 (1979).
- [98] D. Madsen, C. L. Thomsen, J. Thogersen, and S. R. Keiding, *Temperature dependent relaxation and recombination dynamics of the hydrated electron*, The Journal of Chemical Physics **113**, 1126 (2000).
- [99] L. Englert, B. Rethfeld, L. Haag, M. Wollenhaupt, C. Sarpe-Tudoran, and T. Baumert, *Control of ionization processes in high band gap materials via tailored femtosecond pulses*, Optics Express **15**, 17855 (2007).
- [100] K. J. Wædegaard and P. Balling, *High-resolution computer-generated reflection holograms with three-dimensional effects written directly on a silicon surface by a femtosecond laser*, Optics Express **19**, 3434 (2011).
- [101] K. J. Wædegaard, H. D. Hansen, and P. Balling, *Optimizing the efficiency of femtosecond-laser-written holograms*, Applied Physics B, online first (DOI: 10.1007/s00340-013-5496-0) (2013).

-
- [102] G. K. Ackermann and J. Eichler, *Holography, A Practical Approach* (Wiley-VCH Verlag GmbH, Weinheim, Germany, 2007).
- [103] P. Hariharan, *Optical Holography: Principles, Techniques, and Applications* (Cambridge University Press, New York, USA, 1996), 2nd edition.
- [104] T. R. Andersen, Master's thesis, Aarhus University, Denmark (2013).
- [105] A. W. Lohmann and D. P. Paris, *Binary Fraunhofer Holograms, Generated by Computer*, Applied Optics **6**, 1739 (1967).
- [106] B. R. Brown and A. W. Lohmann, *Complex Spatial Filtering with Binary Masks*, Applied Optics **5**, 967 (1966).
- [107] B. R. Brown and A. W. Lohmann, *Computer-generated binary holograms*, IBM Journal of Research and Development **13**, 160 (1969).
- [108] L. B. Lesem, P. M. Hirsch, and J. A. Jordan, *The Kinoform: A New Wavefront Reconstruction Device*, IBM Journal of Research and Development **13**, 150 (1969).
- [109] J. P. Waters, *Holographic image synthesis utilizing theoretical methods*, Applied Physics Letters **9**, 405 (1966).
- [110] H. Yoshikawa, *Fast computation of fresnel holograms employing difference*, Optical Review **8**, 331 (2001).
- [111] M. Lucente, *Interactive computation of holograms using a look-up table*, Journal of Electronic Imaging **2**, 28 (1993).
- [112] Y. Li, Y. P. Dou, R. An, H. Yang, and Q. H. Gong, *Permanent computer-generated holograms embedded in silica glass by femtosecond laser pulses*, Optics Express **13**, 2433 (2005).
- [113] Z. Guo, S. Qu, and S. Liu, *Generating optical vortex with computer-generated hologram fabricated inside glass by femtosecond laser pulses*, Optics Communications **273**, 286 (2007).

- [114] L. Ran and S. Qu, *Self-assembled volume vortex grating induced by femtosecond laser pulses in glass*, Current Applied Physics **9**, 1210 (2009).
- [115] Q.-Z. Zhao, J.-R. Qiu, X.-W. Jiang, E.-W. Dai, C.-H. Zhou, and C.-S. Zhu, *Direct writing computer-generated holograms on metal film by an infrared femtosecond laser*, Optics Express **13**, 2089 (2005).
- [116] C. G. Trevino-Palacios, A. Olivares-Perez, and O. J. Zapata-Nava, *Security system with optical key access*, Proceedings of SPIE **6422**, 42218 (2007).
- [117] O. Bryngdahl and F. Wyrowski, *Digital Holography - Computer-Generated Holograms*, Progress in Optics **28**, 1 (1990).
- [118] D. F. Edwards, *Handbook of Optical Constants of Solids* (Academic, Orlando, USA, 1985), chapter Silicon (Si).
- [119] J. Bonse, K. W. Brzezinka, and A. J. Meixner, *Modifying single-crystalline silicon by femtosecond laser pulses: an analysis by micro Raman spectroscopy, scanning laser microscopy and atomic force microscopy*, Applied Surface Science **221**, 215 (2004).
- [120] H. D. Hansen, *Praktiske anvendelser af laserskrevne hologrammer og optimering af hologramrekonstruktionen (Practical applications of laserwritten holograms and optimization of the holographic reconstruction)*, Master's thesis, Aarhus University, Denmark (2012).
- [121] A. Martínez, M. del Mar Sánchez-López, and I. Moreno, *Phasor analysis of binary diffraction gratings with different fill factors*, European Journal of Physics **28**, 805 (2007).
- [122] K. Zhou, Z. Guo, W. Ding, and S. Liu, *Analysis on volume grating induced by femtosecond laser pulses*, Optics Express **18**, 13640 (2010).
- [123] T. M. de Jong, D. K. G. de Boer, and C. W. M. Bastiaansen, *Surface-relief and polarization gratings for solar concentrators*, Optics Express **19**, 15127 (2011).
- [124] B. G. Streetman and S. Banerjee, *Solid State Electronic Devices* (Prentice Hall, New Jersey, USA, 2000), 5th edition.

[125] <http://www.femtolasers.com/xl-tm.116.0.html> .